University of Kassel
Study programme: Nanoscience

Master's Thesis

Fabrication of Anisotropically Shaped Polymer Particles via Reversal Nanoimprint Lithography and Their Functionalization

submitted by
B. Sc. Tobias Grabsch

March 22, 2019, Kassel

Assessors:
Prof. Dr. Hartmut Hillmer and Prof. Dr. Arno Ehresmann
Supervisors:
Uh-Myong Ha, Andreea Tomita

Contents

1 Introduction

Nanostructures have attracted profound interest as a rapidly growing class of materials for many applications thanks to their tunable physical, chemical and biological properties, which result in enhanced performance compared to their bulk counterparts [1, 2]. They find application in areas such as materials and manufacturing, electronics, energy, medicine, information technology, national security and more. Nanotechnology is, at times, described as the next industrial revolution [3].

The application of micro- and nano-particulate systems has attracted significant interest in pharmaceutical fields, as they enable precisely-targeted, high-dosage delivery of active ingredients to a desired location. Biodegradable polymeric particulates have been used for sustained release of various drugs, while magnetic particles have been used for improved targeting [4–6]. In this magnetic targeting, an active substance is bound to a magnetic compound, injected into a patient's blood stream, and then stopped with a strong magnetic field in the target area. Despite the effectiveness of this targeting, these particles face a challenging *in vivo* environment made up of various biological barriers or proteins that lead to rapid degradation [7]. The interaction of particles with their environment and each other depends on a number of properties. An abundance of research focuses on surface chemistry and particle dimensions, which have a large impact on particle interaction *in vivo* [8–10]. It could be shown, for example, that hydrophilic polymeric chains like polyethylene glycol [11], hydroxyethyl starch [12], or polysialic acid [13], which can be adsorbed or linked covalently to the particles' surface, prevent serum protein adsorption and prolong circulation time [14]. Protecting outer shells often not only stabilize the particles, but can also be used for further functionalization, e. g. by adding binding sites for various ligands [10]. Other research showed particles of identical material to be degraded faster by macrophages if their size exceeds 500 nm compared to that of 50 nm to 200 nm size [5], while particles smaller than 5 nm are rapidly eliminated from the blood stream by extravasation or renal clearance [8].

Another property of micro- and nanoparticles influencing their interaction with biological system is their shape. Particle uptake, half-life and targeting can be improved by utilizing non-spherical shapes [4, 15–18]. Particle degradation by macrophages has been observed to reduce ten-fold for ellipsoidal shapes compared to spherical shapes [19]. Other research investigates the influence of particle size and shape on their deposition in the respiratory tract upon inhalation in order to assess toxicity and efficiency of drug delivery [20].

High interest, therefore, lies in the establishment of synthesis methods allowing a high level of control over the particles' size, shape and surface, while allowing easy variation of these properties as desired for their application. A number of bottom-up synthesis methods for magnetic micro- and nanoparticles have been developed, such as chemical coprecipitation, microemulsion and chemical vapor deposition. Precise control of the above properties, however, remains a challenge when using these methods [10].

A top-down approach to fabricating micro- and nanostructures with uniform size and shape is nanoimprint lithography (NIL). First employed by *Chou et al.* in 1995, it was employed to produce vias and trenches of 25 nm feature size using a hot embossing pro-

cess, where a thin film of thermoplastic material was softened by heating it, and the embossed film was hardened again when cooled down [21]. Extensive research in the following years has made NIL a well-established lithography technique. Its high spatial resolution down to 2 nm, as well as the corresponding variety of possible materials and shapes, represent advantages over bottom-up technologies [22, 23]. When regarding nanopatterning, NIL is one of the most promising techniques due to its low-cost, high-resolution and large-area patterning capabilities compared with other lithography techniques [24]. For example, optical lithography is limited in its resolution due to Abbe's diffraction limit, while electron beam lithography (EBL) has a low throughput [25]. NIL, on the other hand, has been used in various approaches to obtain patterns with sub-10 nm resolution [26, 27] and is compatible with the roll-to-roll process, allowing a high throughput [24]. Furthermore, NIL can be applied to pattern a high diversity of materials. In order to produce particles, the normal NIL technique requires removal of residual material connecting the structures with the substrate after the imprint through reactive ion etching (RIE). This processing step reduces overall efficiency and can interfere with the imprinted structures or embedded materials in an undesirable fashion [24, 28]. A variation of the method termed reversal nanoimprint lithography (RNIL) includes all of the advantages of normal NIL but produces nearly no residual layer (RL), thus eliminating the necessity to perform RIE. Instead of pressing a patterned mold onto the imprint material, the material is applied on top of the mold via spin coating. After the material hardens through temperature or UV exposure, it can be separated from the mold in various ways. This technique, which was patented by *Huang et al.* in 2002, reduces the overall complexity of the fabrication process, allowing for even higher throughput. It also eliminates the need for high temperatures and pressures, allowing for an even broader range of compatible materials. Due to these advantages, the RNIL technique represents an ideal tool for the fabrication of uniformly sized and shaped particles.

In his thesis, *Kaban* used the RNIL technique to fabricate polymer particles, which were magnetically functionalized via magnetic guest particles. The according research was performed in the same institute as this thesis, both of which serve the purpose of investigating the potential of RNIL for the production of multifunctional anisotropically shaped hybrid (MASH) particles. In contrast to *Kabans* work, the research of this thesis aims for particle functionalization through surface modification, utilizing a magnetic thin film. Similarly, the particles are to be produced using RNIL. Future research will then enable the combination of these two functionalization methods, as well as others.

In this thesis, the magnetic surface functionalization will be achieved by sputter deposition of a magnetic film on top of the imprinted polymer. This research will specifically manipulate the magnetic state of the film and, consequently, the particle, towards a predetermined direction, granting more ways to access the particles' translational as well as rotational movement behavior in a magnetic field. This will be done by introducing a unidirectional magnetic anisotropy to the thin film: the exchange bias (EB). This unidirectional anisotropy arises at the interface of an antiferromagnet and a ferromagnet and can dominate the system, opposing the magnetocrystalline and shape anisotropy, which otherwise determine the magnetic behavior of solely ferromagnetic thin films [29, 30].

In detail, this thesis investigates if and how the RNIL technique can be utilized to reliably produce anisotropically shaped polymer particles. To make this applicable to a variety of materials, sizes and shapes, it is vital to understand how variations to process parameters, like utilized imprint resist and preceding mold treatment, influence the outcome of the imprint. Optimization of the overall process, especially with regard to subsequent functionalization, is a key component of this thesis. Moreover, the imprinted polymers will be equipped with an EB layer system by means of sputter deposition. Since the EB effect strongly depends on the substrate it is deposited on, the interplay of the corresponding thin film with the polymer used as substrate is investigated in detail. This will determine how broadly the functionalization method can be applied to materials produced via RNIL.

The above can be summarized in four research goals:

1. The RNIL technique will be used for polymer patterning. This step does not require the fabrication of particles, which is achieved by patterning the polymer in a way that leaves no residual material, but instead focuses solely on fabricating a structured surface. This goal includes optimizing any process parameters or steps tangentially related to the resulting RL.

2. Sputter deposition will be used to magnetically functionalize the patterned polymer. For reference purposes, this includes deposition on unpatterned polymer. This step serves to obtain data on the interplay of the magnetic thin film with the polymer. Further experiments will only be reasonable if this step is successful. It represents a qualitative analysis of the practicability of combining sputter deposition of an EB layer system with RNIL.

3. The RNIL technique will be used to produce polymeric particles that are released from the substrate in water. For this step, good wetting of the imprint mold as well as a nearly complete elimination of residual material after the imprint are crucial features. A variety of imprint resists, mold treatments and process parameters are to be tested for their influence on the experimental outcome.

4. Finally, a patterned polymer film, prepared according to the findings above, will be magnetically functionalized via sputter deposition of an exchange bias layer system onto the polymer surface. Since the deposition must happen before the release of the structures as particles in water, deposition onto the polymer film is, at least in theory, equivalent to deposition onto the particles. The outcome will be analyzed quantitatively to assess the compatibility of magnetic surface functionalization with RNIL produced polymers.

The thesis is structured as follows. Section 2 introduces the theoretical background necessary to understand the phenomenon of exchange bias. The types of magnetic interactions are presented and their role in causing magnetic anisotropy is explained.

Section 3 explains the methods utilized to fabricate patterned polymers and describes the machines used for imaging and magnetic, as well as topographic characterization.

First, the design and fabrication of the silicon master template, which contains the pattern that is to be imprinted, are described. After this, an description of how this pattern is copied onto a PDMS mold is given, followed by a detailed explanation of the RNIL technique. Second, this section provides a description of the sputter deposition process used to deposit the EB layer system onto the polymer film.

In section 4, the machines used for characterization are explained, which are the vibrating sample magnetometer (VSM), Kerr magnetometer and atomic force microscope (AFM).

Section 5 presents and discusses the results. It is organized according to the four research questions above, although the order is adjusted slightly to provide better context. The first two subsections present the research involving polymer patterning using the RNIL technique, while the last two subsections present the research involving thin film sputter deposition on top of unpatterned and patterned polymers.

The thesis concludes with a summary of the obtained results and an outlook for future research based on the results of this thesis.

2 Theoretical Background

When measuring magnetization curves of materials of different crystal structures, it is observed that the magnetization M prefers one or more directions over others. If the external magnetic field is aligned with such a preferred direction, the magnitude necessary for saturation is reduced compared to other directions. The energy required to change the magnetization from such a preferable direction, a so-called easy axis, to the least preferable direction, a so-called hard axis, is called anisotropy energy E_{ani} [31, 32]. This phenomenon is crucial for many applications. For example, storage of binary data through opposing magnetization directions or devices as simple as a compass needle would be impossible without it [31]. The cause of magnetic anisotropy lies in the magnetic interactions of atoms within a material. Accordingly, section 2.1 aims to provide an overview of the magnetic interactions that cause magnetic behavior and, consequently, magnetic anisotropy in a material. It addresses the interaction between atomic dipoles, the quantum mechanical exchange interaction which occurs between atoms that are brought in close contact to one another, and spin-orbit coupling. Section 2.2 then presents the magnetic anisotropies caused by these interactions, providing the knowledge required for interpretations of results and their discussion later in this thesis. The concepts of magnetocrystalline anisotropy, shape anisotropy and unidirectional anisotropy explained in this subsection play an important role in understanding the magnetic experiments performed in this thesis.

2.1 Magnetic Interactions

2.1.1 Dipole-Dipole Interaction

Each dipole in a solid body generates a magnetic field that can interact with other dipoles. The dipole-dipole interaction energy between two dipoles μ_i and μ_j with a distance $\vec{r}$ is given by

$$E_{\mathrm{DD}} = \frac{\mu_0}{4\pi r^3}\left(\vec{\mu_i}\cdot\vec{\mu_j} - \frac{3\,(\vec{\mu_i}\cdot\vec{r})\,(\vec{\mu_j}\cdot\vec{r})}{r^2}\right) \tag{1}$$

with the vacuum permeability μ_0 [33].

The interaction energy between two neighboring atoms can be estimated by assuming a distance of $r = 2\,\text{Å}$, as well as $\vec{\mu_i/j} \uparrow\uparrow \vec{r}$ and $\mu_i/j = \mu_{\mathrm{B}}$, where μ_{B} is the Bohr magneton, changing Equation 1 to

$$E_{\mathrm{DD}} = \frac{\mu_0 \mu_B^2}{2\pi r^3} \approx 2 \cdot 10^{-24}\mathrm{J}. \tag{2}$$

This equation can be used to correlate the energy to a temperature T using $E = k_{\mathrm{B}}T$ with the Boltzmann constant k_{B}, which lies in the sub-Kelvin range [30, 33, 34]. Because remanent magnetization occurs at higher temperatures than this, it is evident that dipole-dipole interaction cannot be the cause of a collective magnetic order in solid

bodies. However, the long range influence of this interaction plays an important role in the context of shape anisotropy and the formation of magnetic domains [30, 34].

2.1.2 Exchange Interaction

The exchange interaction is a quantum mechanical effect based on the fact that electrons, being fermions, are indistinguishable. It causes the degeneration of energy states of electrons in parallel and antiparallel spin configuration [34, 35]. This phenomenon is caused by the Pauli principle, which demands that two or more identical fermions cannot occupy the same quantum state within a quantum system simultaneously. Upon exchange of two identical particles, the total wave function must be antisymmetric. Two electrons that have a symmetric spatial function must have an antisymmetric spin function or vice versa [33].

In consequence, two electrons in a solid state material can occupy the same energy state if they have antiparallel spin (singlet state). If their spin is parallel, they have to occupy different energy states (triplet state). In this case the higher spatial separation leads to a reduced Coulomb repulsion, lowering the potential energy of the system. At the same time, occupation of a higher energy state increases the kinetic energy of the system. Only if the potential energy reduction outweighs the increase in kinetic energy will a parallel spin orientation be favored and a magnetic order introduced to the material. The result of this energy difference strongly depends on the material and can be described by utilizing the isotropic Heisenberg model with the Hamiltonian

$$\mathcal{H} = -\sum_{ij} J_{ij} \vec{S}_i \cdot \vec{S}_j \quad \text{with} \quad J_{ij} = 0 \quad \text{for not neighboring spins,} \tag{3}$$

with the exchange constant J for neighboring electrons with their respective spins S. This model reduces the exchange interaction to the interaction between two neighboring spins based on the short range of the exchange interaction [30, 33, 35].

The exchange constant J_{ij} of two spins depends on the electronic structure of the system and the overlap between the respective spatial wave functions, which itself depends on the distance r of the two spins. J_{ij} can be positive or negative, which translates to ferromagnetic material with parallel spin configuration or antiferromagnetic material with antiparallel spin configuration, respectively [30]. The so-called *Bethe-Slater* curve illustrates this distance dependency for transition metals and is depicted in figure 1.

Although short-ranged, the strength of the exchange interaction ($\approx 10^{-20}$ J per atomic magnetic moment) surpasses that of the dipole-dipole interaction (subsubsection 2.1.1) in several magnitudes and is hence regarded essential for the introduction of magnetic order to solid state materials.

2.1.3 Spin-Orbit Coupling

The second effect that mediates magnetic order in a solid state material is that of spin-orbit interaction, which couples the magnetization of a material to its crystal structure.

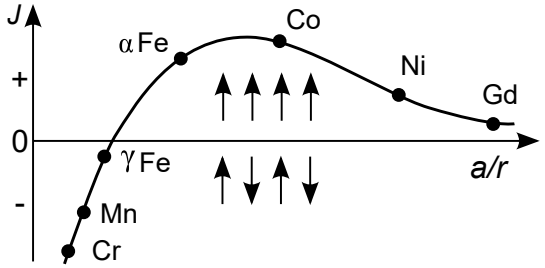

Figure 1: The Bethe-Slater curve illustrates the dependence of the exchange energy on the distance of the atoms for a number of transition metals. Positive values correspond to parallel orientation of the spins, negative values to antiparallel orientation. Adapted from [30, 36]

It determines how the orbital angular momenta $\vec{l}$ and spins $\vec{s}$ of an atom couple to its total angular momentum $\vec{J}$.

In a semi-classical approach, it can be interpreted as the interaction of an electrons spin with the magnetic field caused by its orbital movement, similar to a current in a conductor loop [37]. From the electrons frame of reference, it is orbited by the nucleus with its Coulomb potential V at a distance r. The strength of the spin-orbit interaction energy is proportional to the Coulomb potential gradient and given by

$$E_{\mathrm{SOI}} \propto \frac{\vec{l} \cdot \vec{s}}{r} \frac{\mathrm{d}V}{\mathrm{d}r} \tag{4}$$

The above equation expresses how this interaction becomes stronger for heavy atoms, causing the orbital angular momentum of an electron $\vec{l}$ to couple with its spin $\vec{s}$ to the electrons total angular momentum $\vec{j}$. The total angular momenta of the atom's electrons then couple to the atoms total angular momentum $\vec{J}$ (jj coupling) [30]:

$$\vec{j}_i = \vec{l}_i + \vec{s}_i \quad \vec{J} = \sum_i \vec{j}_i. \tag{5}$$

In contrast, electrons of light atoms have a weak spin-orbit interaction, causing their spins to instead couple with each other to a total spin $\vec{S}$, while their orbital angular momenta couple to $\vec{L}$, which then interact to couple to the atom's total angular momentum $\vec{J}$ (LS coupling) [30]:

$$\vec{S} = \sum_i \vec{s}_i \quad \vec{L} = \sum_i \vec{l}_i \quad \vec{J} = \vec{S} + \vec{L}. \tag{6}$$

2.2 Magnetic Anisotropy

2.2.1 Magnetocrystalline Anisotropy

Magnetocrystalline anisotropy causes the preferred magnetization to follow certain crystallographic directions. It represents an intrinsic, material dependent property of solid bodies. It finds its origin in the crystal fields, which create a preferable orientation of

orbital angular momenta of the solids atoms. Through spin-orbit coupling (see subsubsection 2.1.3), this in turn creates a preferable spin orientation.

The d- or f-electrons in transition metals, which are responsible for the material's magnetic behavior, have an anisotropic density distribution (see figure 2). Changing the orientation of the spins and, through spin-orbit coupling, the orientation of the orbital angular momenta influences the overlap of wave functions of neighboring atoms and, consequently, their exchange interaction and electrostatic interaction [31]. Accordingly, the orbital angular momenta and spins have preferred orientations relative to the crystallographic axes. This behavior is described using anisotropy constants K_{ani}. Calculations show that cubic crystals (e.g. Ni, Fe) have three easy axes equivalent to certain crystal lattice directions, while hexagonal lattices often show only a single easy axis [32].

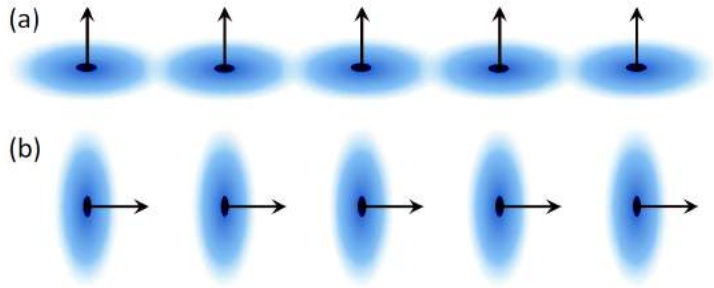

Figure 2: Illustration of the origin of magnetocrystalline anisotropy. The electron density distribution is aspherical, resulting in different exchange interaction and electrostatic interaction for different orientations of the coupled spins and orbital momenta within the crystal lattice. Taken from [31].

2.2.2 Shape Anisotropy

Shape anisotropy gets its name from the dependence on the material shape and the corresponding demagnetization fields (stray fields). As they change with the direction of magnetization, shape anisotropy represents the system's aim to minimize its stray field energy.

Due to the long ranged dipole-dipole interaction (2.1.1), uncompensated magnetic charges on the surface of a magnetized material cause magnetic stray fields [33]. This is especially interesting in the context of a magnetic thin film, which is utilized in this thesis. With a high aspect ratio of its lateral dimension to its thickness, the stray field energy ϵ_{S} is given by

$$\epsilon_{\mathrm{S}}(\vartheta) = \frac{\mu_0}{2} M^2 \cos^2 \vartheta \tag{7}$$

with the vacuum permeability μ_0, and the angle ϑ between the surface normal and the magnetization M [30, 32, 33]. The stray field energy becomes minimal for an in-plane magnetization ($\vartheta = \pi$) [30, 33].

2.2.3 Unidirectional Exchange Anisotropy - Exchange Bias

Another anisotropy is the exchange anisotropy, or EB, a unidirectional (not uniaxial) anisotropy which relates to an interface effect between two different classes of material. Within the context of this thesis, as well as its first discovery by *Meiklejohn and Bean* [29], the effect is observed for a ferromagnet-antiferromagnet interface, although it has also been observed for ferri-antiferromagnetic materials and ferri-ferromagnetic materials [38]. Its discovery led to the description of interlayer exchange coupling between ferromagnets interleaved by paramagnet layers [39] and the proximity effect between ferromagnetic and superconducting layers [40, 41]. The EB effect is being used in spin valves with one pinned and one free ferromagnetic layer as found in devices such as storage media, readout sensors, and magnetic random access memory(MRAM) [42]. If bombarded with keV helium ions, the EB field is locally modified [43, 44], allowing fabrication of magnetically structured EB thin film systems, which can be used for transport of magnetic colloid particles [45, 46], as well as optimization of microfluidic processes [47].

Phenomenology

The EB effect causes the bilayer material to have only one easy direction and manifests itself in a mostly negative shift of the hysteresis loop with respect to the applied field as well as an increase in coercivity [29, 48]. Here, the EB bilayer consists of an antiferromagnet (AF) layer of iridium manganese (IrMn) and a ferromagnet (F) layer of cobalt iron (CoFe). The phenomenon can be understood in an intuitive, qualitative way by regarding a possible fabrication process.

First, the two materials (F and AF) that share an interface are heated to a temperature T that exceeds the Néel temperature T_N of the AF but lies below the Curie temperature T_C of the F ($T_N < T < T_C$). The ferromagnet's spins align with the direction of the applied field H_{FC}, which is set high enough to saturate the F. Then, while the magnetic field remains, the temperature is decreased to a value below T_N. After this so-called field cooling process, the first monolayer of the AF aligns parallel (or antiparallel) with the F spins due to their exchange interaction (see 2.1.2). The next AF monolayer aligns antiparallel to the previous layer and so forth, until the AF order is complete. It is noteworthy that the spins at the AF interface are uncompensated, leading to a net magnetization of the according AF monolayer.

Another way to fabricate an exchange coupled bilayer is by applying an external magnetic field during the deposition of the material layers [42, 49, 50].

If the bilayer material is now exposed to an external magnetic field of opposite direction, the F spins try to follow its direction. Through their coupling to the AF spins, however, it takes a bigger force and thus a stronger external magnetic field to overcome this coupling and rotate the F spins. On the other hand, the F spins require less force to rotate back into their original direction. For all angles except the stable, original direction during field cooling, a torque acts on the F spins, which causes the shift of the hysteresis loop. It is assumed here that the AF spins are rigid during the whole process.

This displacement from the center of the hysteresis loop is called exchange bias field H_{EB} (EB field) and is negative in relation to the orientation of the F spins after field cooling (see figure 3) [42]. Regarding the intersections of the hysteresis curve H_L and H_R with the axis of the external magnetic field, the EB field and the coercive field are defined as

$$H_{EB} = \frac{H_{\mathrm{R}} + H_{\mathrm{L}}}{2} \quad H_C = \frac{H_{\mathrm{R}} - H_{\mathrm{L}}}{2}. \tag{8}$$

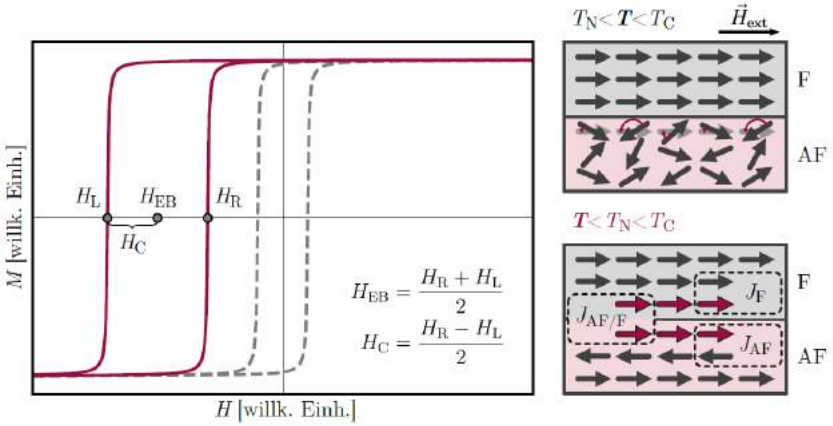

Figure 3: Left: Schematic of the exchange biased hysteresis curve of an AF/F bilayer system in an external magnetic field H prarallel to the easy axis of the uniaxial anisotropy (magenta) compared to that of a solely feromagnetic system (gray). Right: The EB effect is initiated by a field cooling process. Applying a certain temperature T to the system in presence of a saturating external magnetic field $\vec{H}_{ext}$ and succeeding cooling will cause the F spins to follow the external field and the AF spins to couple to the F after cooling. From [46, 51, 52]

Modeling of the EB effect

The description above allows a qualitative understanding of the phenomenon. But due to the variety of fabrication techniques and material systems used to influence structural characteristics like crystallinity and the interfacial properties of the EB bilayers, an overall theory encompassing a consensus of all experimental findings is still unavailable. In lieu of this, the following briefly describes various models based on their relevance for this thesis.

The first model to be mentioned is that of *Stoner and Wohlfahrth* [53]. It was developed in 1947 before the discovery of the EB effect and is used for describing the coherent rotation of the magnetization vector of a ferromagnet during magnetization reversal. Although it has no direct relation to the EB effect, it represents the groundwork on which many advanced models regarding the EB effect are based on [29, 42, 54]. The first of them is the model proposed by *Meiklejohn and Bean* after their discovery of the EB phenomenon. The ideal Meiklejohn-Bean model makes several assumptions [29, 49].

The F layer rotates completely coherent. Both the F and AF are in a single domain state. The AF/F interface is atomically smooth. The AF layer is magnetically rigid. The spins of the AF interface are fully uncompensated. The AF layer has an in-plane uniaxial anisotropy. Additionally, the F and AF are coupled by exchange interaction, which is described using the interfacial exchange coupling energy per unit are J_{EB}. The EB field H_{EB} can then be calculated as

$$H_{\mathrm{EB}} = -\frac{J_{\mathrm{EB}}}{\mu_0 M_{\mathrm{S}} t_{\mathrm{F}}} \tag{9}$$

with the ferromagnetic saturation magnetization M_S and the F layer thickness t_{F} [29]. The above equation describes the expected characteristics of the hysteresis loop for an ideal case and depicts the linear dependence of the EB field H_{EB} on the interfacial energy J_{EB} as well as its inverse dependence on the F thickness. The dependence on the AF thickness is more complex. Figure 4 shows experimental findings on the F and AF thickness dependence obtained by *Mauri et al.* for ferromagnetic nickel-iron (4a) [55], and by *Jungblut et al.* for antiferromagnetic iron-manganese (4b) [56]. It can be observed that a minimum AF thickness is required for the EB effect to occur. With increasing thickness, first the coercivity rises and then the EB field. While the coercivity reaches its maximum and then drops again, the EB field keeps increasing with the AF thickness until it reaches a plateau. For the F thickness, the inverse dependence predicted in Equation 9 can be recognized.

While this prediction regarding the F thickness holds true for several material systems [42, 55], very thin and non-continuous layers [57], as well as thick layers which exceed the domain wall length of the material, contradict this linear dependence [58]. Additionally, this model lacks predictions for the dependence on temperature and grain size, as well as for positive EB or the training effect [51]. The biggest issue, however, is the significant difference between theoretically predicted values for H_{EB} and H_{C} and experimentally observed values [42].

Later models have tried to explain this discrepancy by adjusting some of the above described assumptions. Based on the work of *Meiklejohn* and *Bean*, *Néel* similarly considered an ideal uncompensated spin structure at the AF/F interface, but in contrast postulated its possible deformation, resulting in irreversible change of the spin structure during the F magnetization reversal. This influences the values of both H_{EB} and H_{C} [42, 59, 60]. He also considered a finite roughness of the AF surface, which can contain both AF sublattice types (lattice planes with antiparallel spin orientation), leading to partial compensation of the AF net magnetic moment at the interface and in turn to a lower H_{EB} [60]. Further, the idea of partial domain walls in the AF replaced the concept of its complete rigidness. These domain walls describe the transition area between two neighboring magnetic domains [30] and contain some of the exchange interaction energy, thereby explaining the reduced energy of the interface and thus H_{EB} [42]. A disadvantage of this model is its demand for a material thickness above 100 nm, which limits its suitability to quantify thin film systems [61].

The *random-field* model by *Malozemoff* assumes a monocrystalline AF and a single domain F [62]. It postulates a AF/F interface with random atomic roughness. Con-

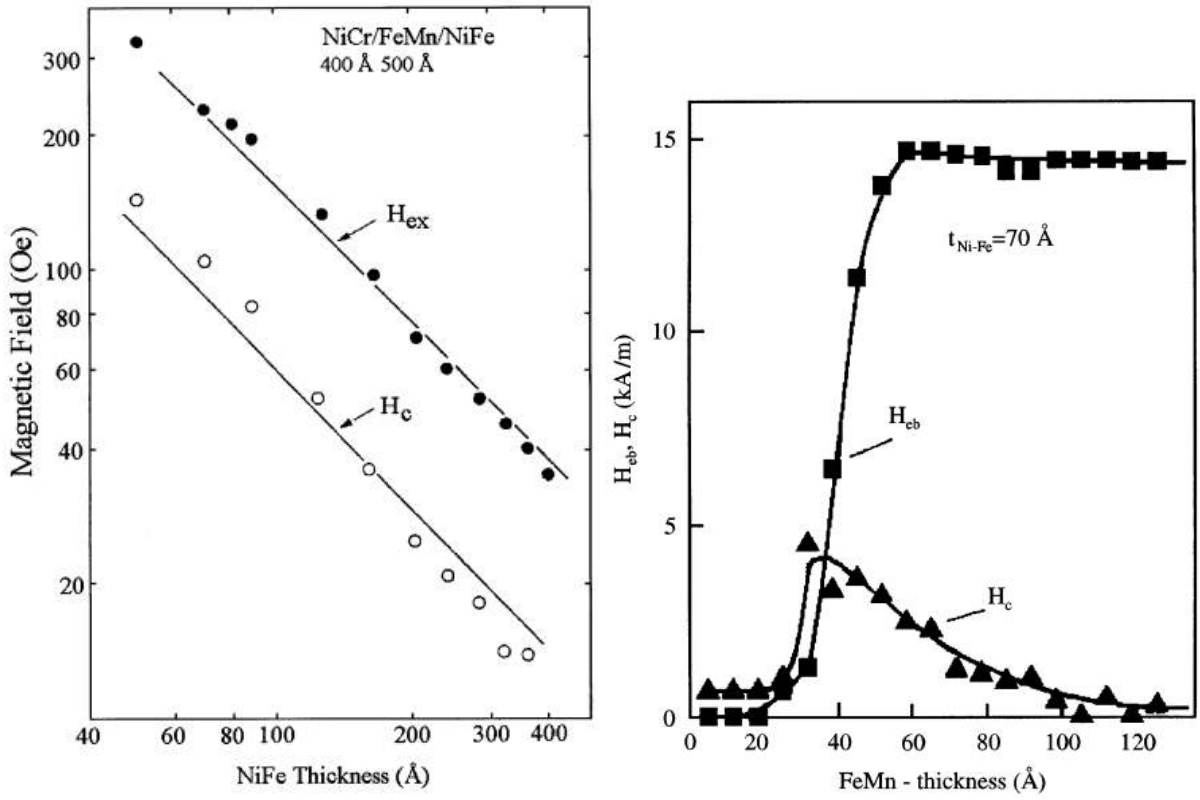

(a) ferromagnet (b) antiferromagnet

Figure 4: Dependence of H_{EB} and H_{C} on the thickness of the F (a) [55] and AF (b) [56] for a bilayer system of FeMn/NiFe.

sequently, the interface contains both compensated and uncompensated AF interface moments resulting in a net AF interface moment, especially when regarding small areas. A consequence of the *random-field* model is the formation of AF domains perpendicular to the AF/F interface due to the interplay of the magnetostatic and magnetocrystalline anisotropy energy, reducing the unidirectional anisotropy. This is illustrated in figure 5b, showing uncompensated spins (blue) and domain walls in the AF (white dashed line).

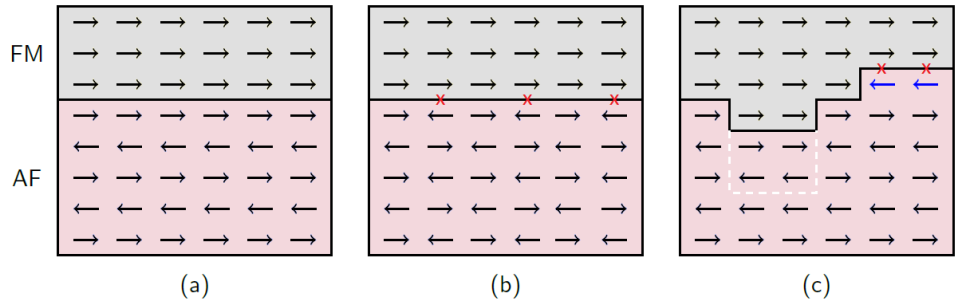

Figure 5: Spin coupling at an AF/F interface. For an ideal interface the AF spins are completely uncompensated, as shown in (a). (b) shows an ideal compensated interface and (c) portrays the case for a rough interface, containing uncompensated spins (blue) and domain walls in the AF (white dashed line) [25, 63]. Edited from [64].

One of the best and first models describing polycrystalline EB systems is that of *Fulcomer and Charap* [60, 65, 66]. Here, the AF is regarded as an ensemble of isolated AF grains with their respective grain size distribution, which influences both H_{EB} and H_{C} [65]. The AF grains have a uniaxial magnetocrystalline anisotropy $K_{\mathrm{AF}i}$, an effective magnetic volume V_i^* and the interface S_i^* to the F that mediates the exchange interaction. This is illustrated in figure 6.

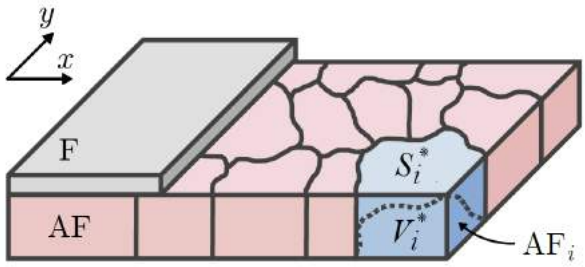

Figure 6: Illustration of the polycrystalline model of *Fulcomer* and *Charap*. Individual AF grains with a volume V_i^* interact with the single domain F through their shared interface S_i^* [65, 67]. Edited from [52].

To include the reducing influence of the interface roughness on the exchange interaction energy $E_{\mathrm{AF},i}$, the factor σ_i is added. Using these properties, the free energy of an AF domain E_i can be modeled as

$$E_i = K_{\mathrm{AF}i} V_i^* \sin^2(\theta_i - \Phi) - \sigma_i J_{\mathrm{AF/F},i} S_i^* \cos(\theta_i - \phi) \tag{10}$$

with the angle θ_i between the AF interface moment and the uniaxial anisotropy axis of the F (easy axis), the angle ϕ between the F magnetization direction and its respective uniaxial anisotropy axis and the angle Φ between the easy axes of AF and F [46, 65]. The first term of Equation 10 can be summarized as free uniaxial anisotropy energy $E_{\mathrm{AF},i}$ and the second term as free EB energy $E_{\mathrm{EB},i}$ of the respective AF domain. Equation 10 then becomes

$$E_i = E_{\mathrm{AF},i} \sin^2(\theta_i - \Phi) - E_{\mathrm{EB},i} \cos(\theta_i - \phi). \tag{11}$$

For a magnetization parallel or antiparallel to the F easy axis, the above equation shows a global or local minimum, respectively, as is shown in figure 7.

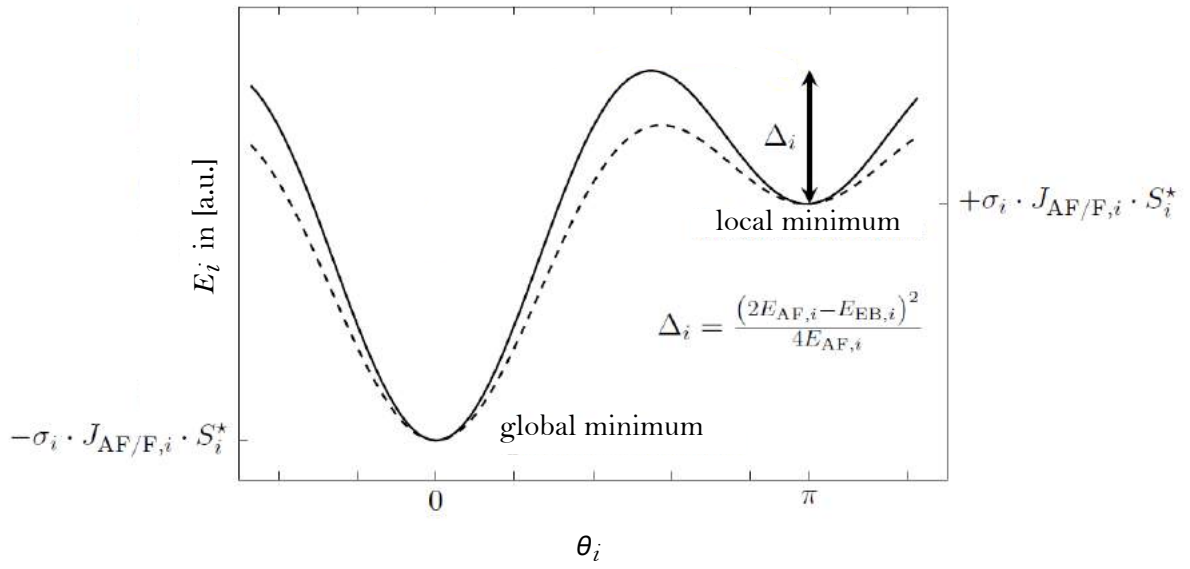

Figure 7: Free energy E_i of an AF grain as a function of angle θ_i between the orientation of the AF interfacial moment and the magnetization of the F, shown for two AF grains with different magnetocrystalline anisotropy energy $E_{\mathrm{AF},i}$ (Solid line: $E_{\mathrm{AF},1}$; Dashed line: $E_{\mathrm{AF},2} = (3/4) \cdot E_{\mathrm{AF},1}$). The energetic minima at $\theta_i = 0$ and $\theta_i = \pi$ are separated by an energy barrier Δ_i, which can be overcome through thermal activation. Edited from [46, 65, 67, 68].

The energy barrier Δ_i for the transition of the local to the global minimum is given as [65, 68]

$$\Delta_i = \frac{(2 \cdot E_{\mathrm{AF},i} - E_{\mathrm{EB},i})^2}{4 \cdot E_{\mathrm{AF},i}}. \tag{12}$$

An energy barrier therefore only exists for AF grains with $E_{\mathrm{AF},i} > \frac{E_{\mathrm{EB},i}}{2}$. Further, the dashed line in figure 7 indicates the decrease of the energy barrier Δi for smaller $E_{\mathrm{AF},i}$ and constant $E_{\mathrm{EB},i}$.

Based on this, AF grains can now be classified according to their free uniaxial anisotropy energy $E_{\mathrm{AF},i}$, which is illustrated in figure 8. At room temperature, grains with $E_{\mathrm{AF},i} <$

$k_\mathrm{B}T_\mathrm{R}$ are thermally unstable (superparamagnetic) and have no contribution to H_EB or H_C (figure 8a). Grains with $k_\mathrm{B}T_\mathrm{R} < E_{\mathrm{AF},i} < \frac{E_{\mathrm{EB},i}}{2}$ follow the orientation of the F, as the coupling between F and AF is stronger than the AF grain anisotropy. They contribute to H_C, but, because of the lack of an energy barrier, not to H_EB (figure 8b). Domains with $\frac{E_{\mathrm{EB},i}}{2} < E_{\mathrm{AF},i}$ do not follow the orientation of the F and stay in the local minimum. For the high temperatures during field cooling, the energy barrier can be overcome and AF-F coupling realized. These grains contribute to H_EB and H_C (figure 8c). Grains with very high $E_{\mathrm{AF},i}$ have an energy barrier too high to be overcome during field cooling. Their orientations are randomly distributed and they do not contribute to H_EB (figure 8d) [60, 67, 68].

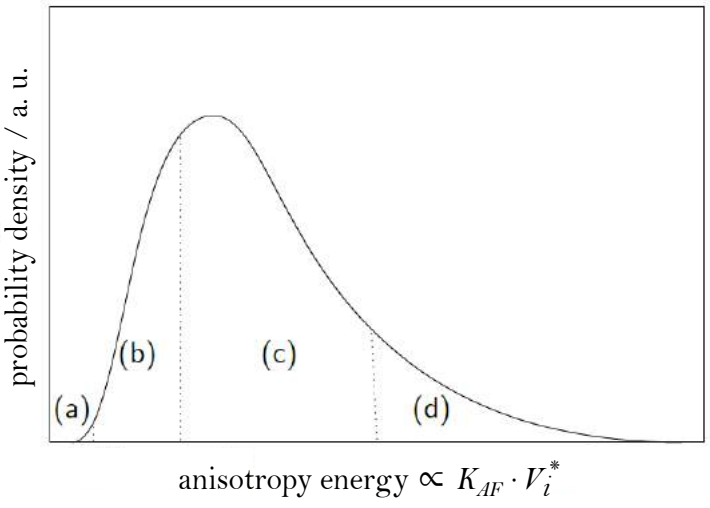

Figure 8: Schematic of grain size distribution in the AF in the polycrystalline model. The probability density follows a logarithmic normal distribution. Regarding their energy barrier, grains are grouped in four classes. These are thermally unstable AF grains (a), thermally stable grains that contribute to H_C (b), grains that can be reoriented during field cooling and contribute to both H_EB and H_C (c) and statistically oriented grains that are stable even during field cooling and do not contribute to the EB effect (d) [60, 67, 68]. Edited from [64].

3 Methods for Polymer Patterning and Magnetic Functionalization

In this section, the methods used to fabricate and functionalize patterned polymers are given. First, the process used to construct the two master templates used in this thesis is described. Then, the procedures used to fabricate the PDMS molds created with the master templates are presented, followed by a detailed description of the RNIL technique utilized to produce the particles. Ths description represents the main concepts as employed in the beginning of this thesis. Problems and solutions related to these concepts are included in the research section presented in section 5. Finally, the sputter deposition process used to apply a magnetic thin film on top of the patterned polymers is described. Here, crucial information about the exchange bias layer system is given, which pertains to the results found in sections 5.3 and 5.4.

3.1 Master Template Fabrication

The most vital part of any NIL or RNIL is the master template (MT) that contains the structures that are to be imprinted on suitable material. It is fabricated in multiple steps, which are illustrated in figure 9.

First, an electron beam (e-beam) sensitive resist is spin coated to a silicon wafer. Then, EBL is used to write the desired structures into the resist (figure 9a). The device employed to perform this is the *eLINE Plus* manufactured by *Raith Nanofabrication GbmH*. The resist is termed positive e-beam resist if its exposure to the beam causes its chains to fall apart, increasing its solubility. In contrast, it is termed a negative e-beam resist if exposure induces cross-linking of the chains, thereby decreasing solubility [69]. Here, the poly(methyl methacrylate) (PMMA) resist *AR-P 617.06* purchased from *allresist GmbH*, is used as a negative resist. After writing of the desired structures has been completed, the development of the MT follows, beginning with the removal of all but the exposed resist using a solution of methyl isobutyl ketone and isopropyl alcohol (MIBK:IPA) (figure 9b). After this, chromium is deposited on top (figure 9c). When the resist is removed in a lift-off process using *N*-Methyl-2-pyrrolidone (figure 9d), only the chromium that is in direct contact with the wafer remains, acting as a protective layer during the next step of anisotropic etching with C_4F_8 and O_2. (figure 9e). This process creates a negative of the structures on the silicon wafer. In a final step, the chromium layer is removed by chromium etching, leaving nothing but the structured MT behind (figure 9f).

A detailed schematic of the two MT designs used during this thesis is shown in figure 10. The first MT contains structures of four different dimensions (figure 10a). A rectangle with zig-zag edges of 2 µm and 5 µm edge length and three differently sized isosceles triangles of 2.5 µm, 5 µm and 7 µm base and height. All structures are 1 µm in depth, except the 2.5 µm triangles, which have a depth of 0.8 µm. They are arranged on the MT in four squared arrays of 1 mm edge length. The distance between two structures equals their base and edge length, respectively. The resulting four squares are arranged

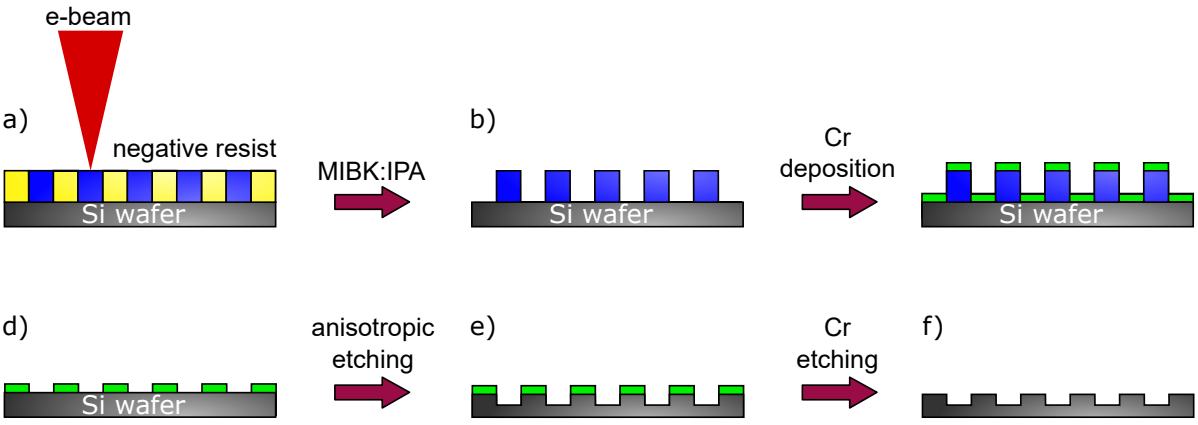

Figure 9: Writing of the MT using EBL and its development.

in another square, four of which are again arranged to form a square that contains a total of 16 arrays. Due to this design, this MT is hereafter referred to as 16-array MT. It was designed in this way to investigate the influence that different structure dimensions might have on the filling of the structures as well as later applications of the imprinted polymer structures. This arrangement also serves to investigate a possible direction dependent distribution of imprint material, especially relevant in the context of guest particles.

The second MT contains triangular structures of four different sizes, measuring 12.5 µm, 10 µm, 7.5 µm and 5 µm (figure 10b). Again, the base is equal to the height, while all structures are separated by 2 µm. They each form four squared arrays of 5 mm edge length. A key feature of this design is the spatial separation of the four arrays by 5 mm, intended to enable separation of the arrays after the imprint process. This MT is henceforth referred to as 4-field array.

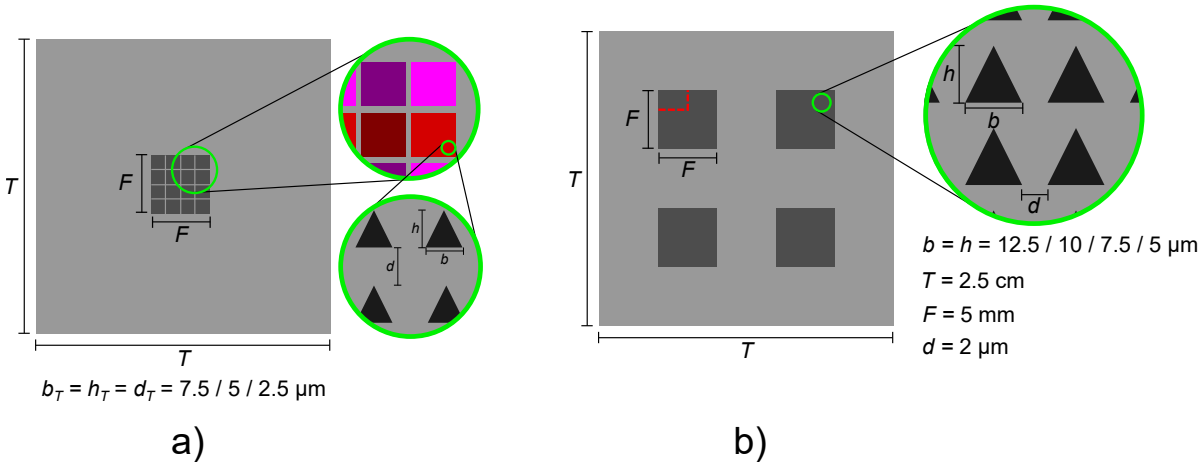

Figure 10: Schematics of the two MT designs used during this thesis. The red dashed line marks the area that was was not written due to unintended abortion of the writing process.

Due to technical difficulties in its development process, the structures of the MT suffer from defects and gaps. The extent of these defects varies with the structure size: the larger the structures, the more defects are observed. An example of these defects can be seen in figure 11, displaying a scanning electron microscope (SEM) image of the 10 µm sized structures. Additionally, the writing process via e-beam was aborted for the largest field, leaving it with a shape like a vertically mirrored L, as indicated by the red dashed line in the top left field in figure 10.

Figure 11: SEM image of the array containing the 10 µm sized structures. Many gaps and structural defects due to complications in fabrication can be observed.

3.2 Copying the Master Template Structures to a PDMS Mold

The fabrication of a MT is costly and time consuming. To minimize its wear, a stamp made out of Polydimethylsiloxane (PDMS) is molded and used for sample production in its place. This process is comparatively simple and is explained in the following.

The adhesion between MT and PDMS can cause removal of the structures upon their separation [70], which is prevented by a non-stick coating. For this, perfluorodecyltrichlorosilane (FDTS), purchased from *ABCR GmbH*, is utilized. It consists of a polar head and an unpolar tail. The polar head forms a covalent bond to the hydroxyl groups at the MT's surface, thereby forming a silanole. The heavily fluorinated tail reduces the surface energy, decreasing PDMS adhesion. It is deposited using molecular vapor deposition. For this, it is filled into a small aluminum bowl next to the MT, both positioned on a hot plate at 250 °C. This setup is covered by a Petri dish for 1 hour. Successful coating results in a self-assembled monolayer and can be tested by estimating the contact angle of a drop of water, which changes visibly compared to uncoated silicon.

After application of the non-stick coating, first hard PDMS (h-PDMS) and then soft PDMS (s-PDMS) are cast onto the MT to form a hybrid mold. The h-PDMS, being more physically resilient than the soft counterpart, embeds the structures, while s-PDMS

forms the body of the mold. The use of hybrid molds is advantageous as they combine the benefits of soft molds, such as increased yield and mold preservation, with that of hard molds, such as high resolution lithography [71].

These molds are referred to as hybrid molds, and serve as the primary type of mold used in this thesis, unless otherwise specified. The h-PDMS is obtained by combining two components: component A (product no.: AB112958, AB153234 and AB1719912) and component B (article no.: AB109380), purchased from *ABCR GmbH*, in a mass ratio of 3:1, as recommended by the manufacturer. The s-PDMS is purchased from *Dow Chemical Company* and is also obtained by mixing two components, SYLGARD 184 Silicone Elastomer base and curing agent, in a mass ratio of 10:1.

The h-PDMS is spin coated onto the MT at 1000 rpm and hardened for 20 minutes at 65 °C, after which s-PDMS is manually poured on top. A glass substrate is then positioned on top of the liquid, viscous s-PDMS to serve as mold holder and enable its future handling. To hold it in place and allow a proper body thickness of the mold, the glass substrate rests on two more glass substrates placed on both sides of the MT. A schematic of this is shown in figure 12. This is setup on an aluminum plate and hardened at 65 °C either on a hot plate or in an oven. After 24 hours, the hardened mold is separated from the MT and hardened for another three days. The separation is achieved through careful use of a scalpel[1]. This process can be repeated multiple times without renewal of the FDTS layer, as long as its presence is occasionally confirmed, as mentioned above. This represents the general process that was utilized in the beginning

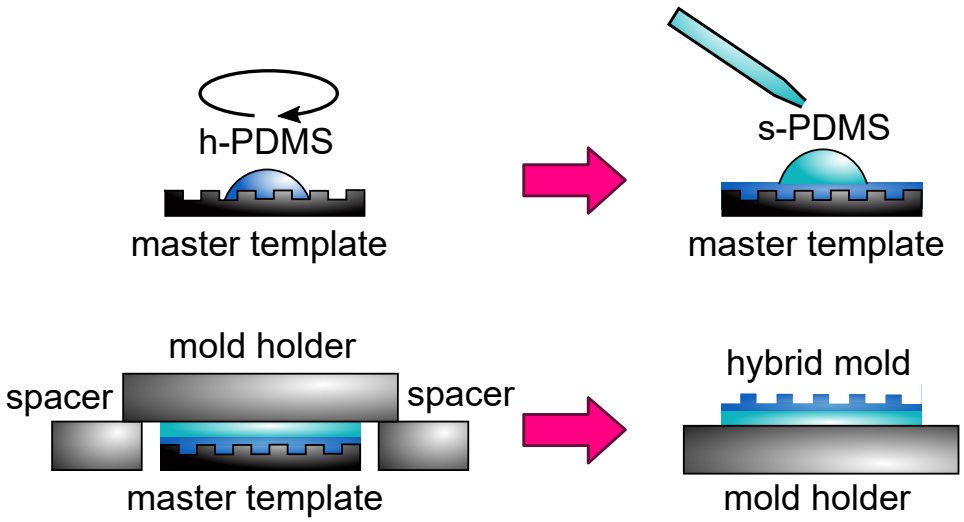

Figure 12: Schematic of the molding process. The MT is covered by first h-PDMS and then s-PDMS to form a hybrid mold. The glass substrate that serves as mold holder is placed on top of the PDMS and two spacers.

of the thesis. Adaptations developed to optimize this process are addressed in section 5.1.2.

[1] The separation process can be supported by drenching the setup in ethanol. If this is done, additional drying of the mold is required to remove absorbed ethanol.

3.3 Reversal Nanoimprint Lithography Utilized for Particle Fabrication

Using RNIL, a thick RL can be avoided. In turn, reactive ion etching after the imprint process is not required. Additionally, the imprint material is spin coated onto the mold, eliminating the need for high temperature and pressure.

A detailed schematic of the RNIL process is displayed in figure 13. It shows the approach as employed by *Ha et al.* [28]. First, the mold is preheated at 115 °C to evaporate any adsorbed water. This preparatory step is especially important if the utilized mold has been stored for multiple days or water has been used to remove residual PVA from earlier processes. Then, the imprint material, consisting of a PMMA solution of low viscosity, is cast onto the mold using a glass pipette (figure 13a). A delay time can be introduced before distributing the material on the mold by spin coating. The imprinted mold is then placed on a hot plate, where exposure to 115 °C for 15 minutes causes the solvent to evaporate, leaving behind the hardened PMMA (figure 13b). The schematic includes a curvature at the PMMA filling the cavities, which represents the concave miniscus observed to occur in these conditions. The cured imprint material is then retrieved from the mold by use of an extraction layer made of polyvinyl alcohol (PVA), as employed first by *Kavre et al.* and later *Ha et al.* The liquid PVA solution gets added on top of the imprint and its solvent evaporates again at 115 °C within 10 minutes (figure 13c). The structured PMMA layer adheres to the solid but flexible PVA layer, which is peeled off from the mold using tweezers and stored on sample substrates of glass or silicon (figure 13d). After this, the structured PMMA can be released as particles by adding water (figure 13e).

A variety of PMMA solutions purchased from *Allresist GmbH*, which will be specified further in section refsec:results:resist, are used as imprint material. The PVA solution is obtained by dissolving 2 *wt*% solid PVA in deionized water. For this, the water is heated to 80 °C, after which PVA is added over the course of 1 hour to 2 hours, depending on the volume, allowing time for its dissolution during constant stirring.

3.4 EB Layer Deposition

Magnetic functionalization of the structured polymers is to be achieved through deposition of an EBLS (see chapter 2.2.3). This is achieved by means of sputtering, the ejection of surface atoms from an electrode caused by momentum transfer from bombarding ions.

Strictly speaking, sputtering is an etching process which can be used for surface cleaning and pattern delineation [72]. It also produces a vapor of electrode material and is, like evaporative deposition, more commonly used for the deposition of thin films. In this context, the process is commonly referred to as sputter deposition [72].

In this thesis, this is done via diode sputtering containing an anode and a cathode in a vacuum system. Here, the material desired for deposition is placed above the sample as a plate, called a target, and used as a cathode. The target material is then transported

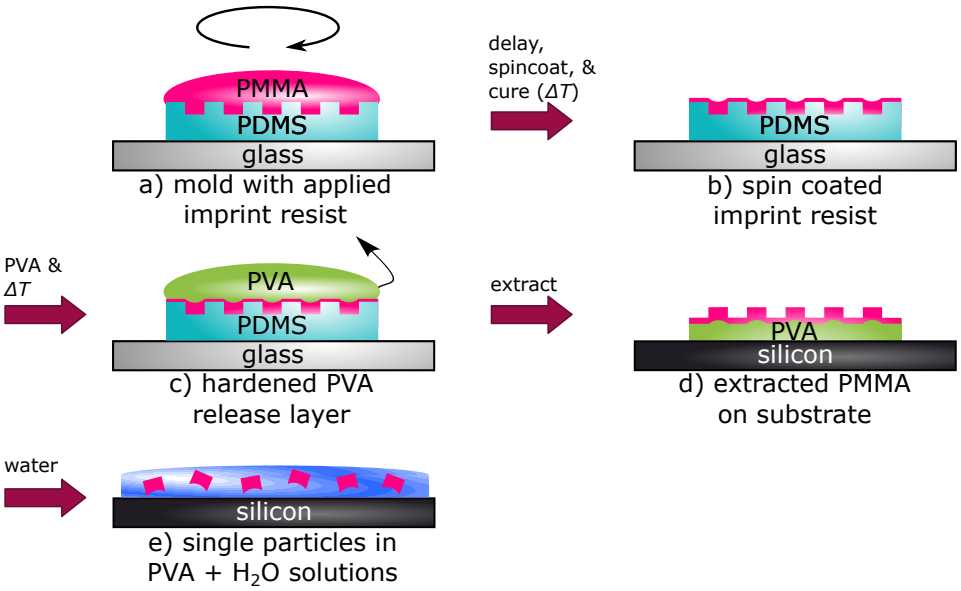

Figure 13: Detailed schematic of the RNIL process. The PMMA solution as imprint material is applied onto the PDMS mold (a) and thermally cured for 15 minutes at 115 °C after a delay time (b). PVA dissolved in water is applied onto the hardened polymer film (c) and also cured thermally at 115 °C until hardened. The hardened but flexible PVA foil is then peeled off, separating the imprinted PMMA from the PDMS mold (d). When added to water, the PVA foild dissolves which causes the imprinted structures to be released as particles if residual layer connecting them is thin enough (e). Edited from [28].

to the substrate via glow discharge of an inert gas to form a film. Radio frequency sputtering, as used in this thesis, applies a high frequency of 13.6 MHz to the electrodes to ignite an argon plasma at a gas flow of 140 sccm. To ensure a sufficient mean free path length, the base pressure is chosen as $p_{\mathrm{B}} \approx 3 \cdot 10^{-7}$ mbar, resulting in a process pressure of $p_{\mathrm{Ar}} \approx 1.2 \cdot 10^{-2}$ mbar [73, 74]. Due to their inertia, the argon ions (Ar^+) cannot follow the quickly alternating current, while generated electrons follow the current to the electrodes [73]. The target is electrically insulated through combination of the RF source and a condensator, causing the target to get charged with a DC voltage U_{DC}. This voltage accelerates the argon ions towards the target, causing the sputtering [73, 74]. The setup is illustrated in figure 14 (left).

To induce unidirectional anisotropy during layer growth, two permanent magnets are positioned on the substrate holder, which generate a homogeneous magnetic field of $\vec{H}_{\mathrm{ext}} \approx 28\,kA/m$ [73].

The layer systems used for this thesis are generally deposited onto structured PMMA, while other substrates have also been tested. The exchange bias layer system (EBLS) consists of an antiferromagnetic $Ir_{17}Mn_{83}$ and a ferromagnetic $Co_{70}Fe_{30}$ bilayer plus an underlying Cu buffer layer and a cap of Si as oxidation protection layer (see figure 14 right). The deposition occurred with a gas flow of 140 sccm. The sputter rates in nm/min were 6.75 (Cu), 5.4 (CoFe), 4.46 (IrMn) and 2.8 (Si). The AF is chosen because

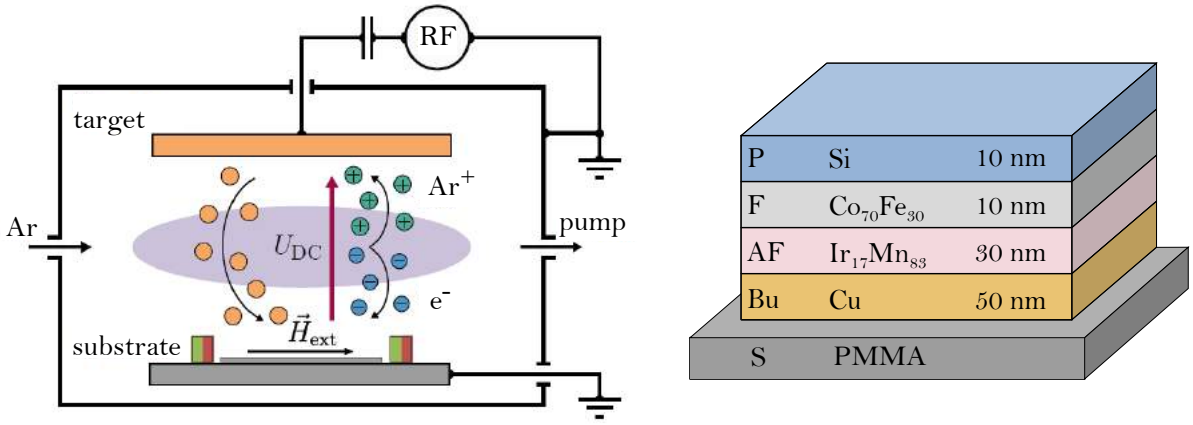

Figure 14: Left: Schematic of the RF sputter deposition process as utilized in this thesis. Right: Schematic of the polycrystalline layer system. Edited from [52, 73].

of its resistance to corrosion and its high thermal stability with a *Néel* temperature of $T_{\mathrm{N}} \approx 690$ K [46, 60, 75]. Maximal exchange coupling is observed for a parallel orientation of the AF (111) plane with respect to the substrate. Copper is chosen as buffer layer to support the respective crystal growth [46, 76]. The ferromagnet is chosen for its high magnetocrystalline anisotropy and *Curie* temperature $T_{\mathrm{C}} \approx 1200$ K [46, 75, 77, 78].

4 Machines for Characterization

After patterned polymers have been fabricated and magnetically functionalized, as described in section 3, they must then be characterized. This section describes the three machines used to accomplish this: vibrating sample magnetometer (VSM), Kerr magnetometer and atomic force microscope (AFM).

4.1 Vibrating Sample Magnetometer

The magnetic moment $\vec{m}(\vec{H}_{\mathrm{ex}})$ of a material within an external magnetic field can be measured through the voltage it induces in an electric conductor that is brought close to the sample surface [79]. The sample generates surrounding magnetic stray fields depending on its magnetization and the correlated uncompensated magnetic charges on its surface. If the sample is driven to oscillate, a temporal change in magnetic flux density caused by the stray fields induces an electric voltage U_{I} in the conductor proportional to the sample's magnetic moment $\vec{m}(\vec{H}_{\mathrm{ex}})$.

Based on this effect, a precise method to measure the magnetic moment of a sample was developed by *Foner* [79]. The VSM, as used in this thesis, is set up as follows and as illustrated in figure 15. The magnetic sample (1) is placed on the sample holder (2) between the pole pieces of an electromagnet (4) and held in place by suction from a vacuum pump. The sample holder is vertically attached to a loudspeaker (3), which drives its oscillation perpendicular to the external field. Two pick up coils (5), which serve to detect the induction voltage U_{I}, are attached on each of the two pole pieces of the electromagnet. The amplitude of the alternating current induced by the sample is proportional to its magnetic moment and amplified via lock-in amplifier.

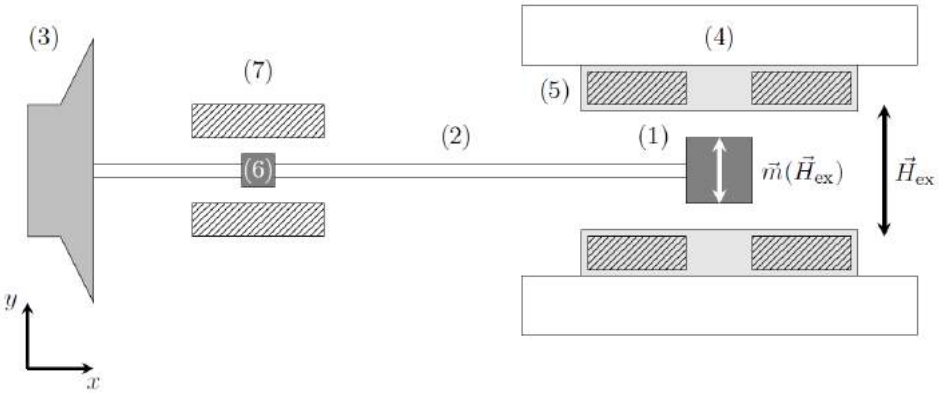

Figure 15: Schematic setup of the VSM used in this thesis, showing (1) sample, (2) sample holder, (3) loudspeaker, (4) electromagnet, (5) pick-up coils, (6) reference magnet and (7) reference pick-up coils. From [46].

The result of a measurement is a hysteresis curve, where the magnetization is integrated over the whole sample, rendering the outcome highly dependent on the sample

geometry. Exact determination of the sample's magnetization is only possible after calibration with a reference sample of known magnetization, which is described in more detail in [80]. Accordingly, this thesis utilizes VSM measurements to compare the influence of the substrate, which the EBLS grows on, on the magnetic properties of the sample. For interesting samples, such as via RNIL structured PMMA with exchange bias functionalization, complementing measurements via *Kerr* magnetometer are provided. Also, the hysteresis curves measured with the device used during this thesis have shown a systematic shift of $\Delta H_{\mathrm{EB}} = 0.3\,\mathrm{kA/m}$. The data presented has been corrected by this value. The occurrence of this shift has been reported in earlier works with this machine as well [73].

4.2 Kerr Magnetometry

The magneto-optic Kerr effect (MOKE) describes a change of intensity or polarization of light reflected from a magnetized surface. It was first discovered by *John Kerr* in 1876 [30, 32] and can be used in a *Kerr* magnetometer to record the hysteresis curve of a magnetic sample in an external magnetic field. While the *Kerr* effect describes changes to light reflected from a magnetic surface, a similar effect, called the *Faraday* effect, is observed for changes in light transmitted through magnetic materials [81].

Linearly polarized light can be described as a superposition of two waves, a left circularly polarized one and a right circularly polarized one, as illustrated in figure 16.

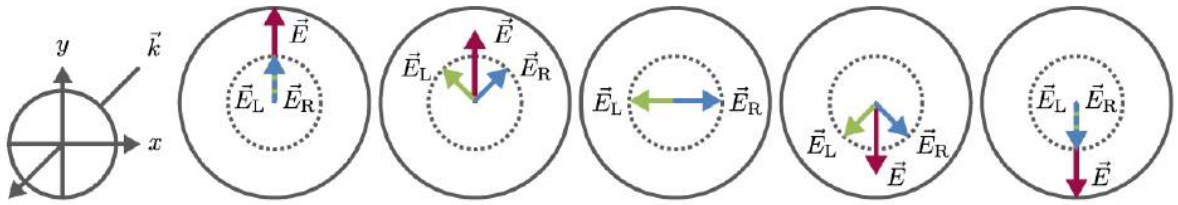

Figure 16: Linearly polarized light with an electric field vector $\vec{E}$ can be described as a superposition of a left circularly polarized wave with $\vec{E}_{\mathrm{L}}$ and a right circularly polarized wave $\vec{E}_{\mathrm{R}}$ of equal amplitude. From [52].

The rotation of the plane of polarization (*Kerr* rotation) by an angle ϑ_{K} occurs because magnetized material shows different refractive indices for left (n_{L}) and right circular polarized light (n_{R}), known as circular birefringence [81], causing different phase velocities. This leads to a different phase shift between the two waves, resulting in the observed rotation of the linearly polarized light by the *Kerr* angle θ_{K}.

Elliptically polarized light is similarly caused by a difference in absorption coefficients for left (ε_{L}) and right circularly polarized light (ε_{R}), resulting in different light intensities. The two reflected circularly polarized waves then form the observed elliptic polarization. This phenomenon is called magnetic circular dichroism [81]. The effects of the Kerr rotation and magnetic circular dichroism are illustrated in figure 17.

The magneto optic *Kerr* effect is placed in different categories depending on the direction of the magnetization vector with respect to the reflecting surface and the plane

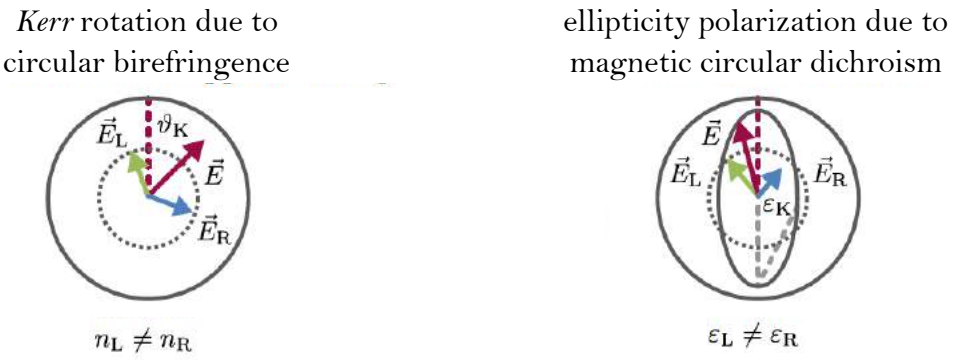

Figure 17: Magnetized material shows different refractive indices (circular birefringence) as well as different absorption coefficients (magnetic circular dichroism) for differently circulary polarized light. The change in amplitude causes ellipticity of the polarization plane [81]. From [52].

of incidence. These categories are depicted in figure 18.

For the polar magneto-optic Kerr effect (P-MOKE), the magnetization vector is perpendicular to the reflective surface and parallel to the plane of incidence. It causes the reflected beam to change from linear polarization to elliptic polarization and to change its polarization angle.

If the magnetization is parallel to the reflective surface and perpendicular to the plane of incidence it is termed transversal magneto-optic Kerr effect (T-MOKE). This effect only occurs for light with its polarization parallel to the plane of incidence. The consequence is a change in intensity of the reflected beam instead of the polarization angle.

The effect most relevant for this thesis is the longitudinal magneto-optic Kerr effect (L-MOKE). Here, the magnetization vector is parallel to the reflective surface and parallel to the plane of incidence. Similar to P-MOKE, linearly polarized light becomes elliptical and experiences a polarization rotation proportional to the magnetization. The rotation is opposite for parallel and perpendicular polarization of the incident beam [32, 81].

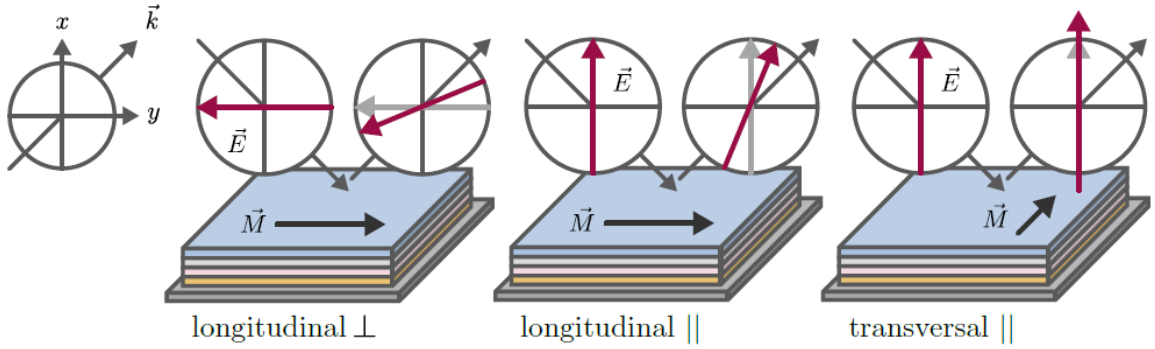

Figure 18: Selected MOKE geometries for a magnetization parallel to the sample surface. The polarization plane indicated by the magenta arrow experiences a rotation by the *Kerr* angle ϑ_K upon its reflexion from the sample surface [32]. From [52].

For this thesis, an L-MOKE magnetometer was employed for the magnetic characterization of structured polymer samples with exchange bias functionalization. The device is equipped with a diode laser of $\lambda = 635\,\mathrm{nm}$ wave length and a beam diameter of approximately $100\,\mu\mathrm{m}$ on the sample surface [46]. In order to eliminate any transverse components of the magnetization during magnetization reversal, a polarizer is placed in front of the light source to allow transmission only for perpendicularly polarized light [51]. The reflected beam first passes through a combination of a polarizer and a polarizing analyzer set approximately 90° to it, before being converged onto the photo diode detector by converging lenses. This setup enables detection of relatively small polarization rotations (less than $1\,^\circ$ for common ferromagnets [81]) by translating them into relatively large changes in transmitted amplitude [51].

4.3 Atomic Force Microscopy

A AFM can be used to examine structures that are too small to be observed via optical or electron microscopy. The limitations coming from diffraction effects can be circumvented by scanning each point of a probe individually while measuring a specific property [82].

In this thesis, an AFM is used to examine the sample topography with sub-micrometer resolution. In this regard, information about surface roughness and grain size distribution are gathered and interpreted.

An AFM is able to examine nanosized objects by scanning a probe in a distance of only several nanometers, measuring attractive or repellent interaction at each scanned point. This interaction is described with the *Lennard-Jones* potential

$$V(r) = \frac{C_\mathrm{r}}{r^{12}} - \frac{C_\mathrm{a}}{r^6} \tag{13}$$

where C_r and C_a represent material constants regarding the repulsive and attractive part of the potential, whereas r represents the distance between tip and sample surface [25]. Equation 13 includes a repellent force at very low distance between tip and probe surface, caused by the repulsion of the atomic shells. This force scales with a z^{12} term and is dominant over the attractive *Van der Waals* term at short distances, which is also included in the *Lennard-Jones* potential. Latter grows in relevance with increasing distance. The *Van der Waals* interaction consists of the *Keesom* force (between permanent dipoles), the *Debye* force (between dipole and induced dipole) and the *London* dispersion force (between instantaneously induced dipoles) and scales with an z^6 correlation. If added up, these terms lead to the term described in Equation 13.

When the tip is brought close to the surface, the cantilever it is attached to encounters a deflection. The deflection is measured via optical lever to gain information about the affecting forces [25]. Accordingly, a laser beam is pointed at the back of the cantilever, which is covered with a reflective medium. The reflection of the beam is gathered at a quadrupole photodiode. The diode measures differences in the direction of the reflected beam by interpreting differences in the induced voltages of its four compartments. Given the long optical lever, even small deflections of the cantilever can be detected this way. The diode signal itself is digitally amplified and compared to reference signals and then

fed in a feedback controller, which regulates the distance between sample and tip by varying the voltage of a piezoelectric actuator. A schematic of the setup is shown in figure 19.

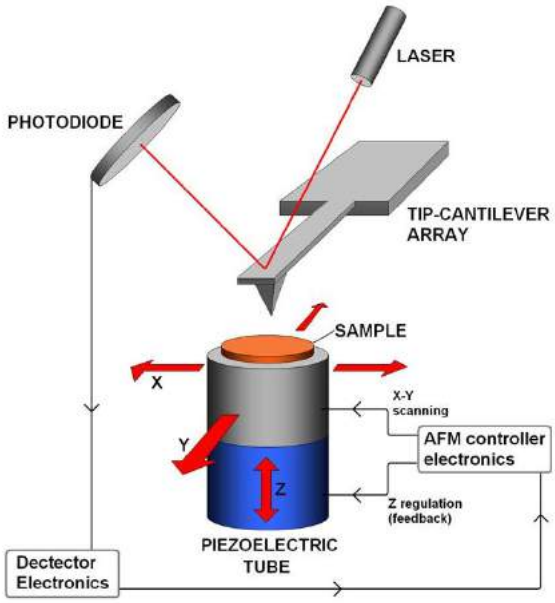

Figure 19: Schematic setup of an AFM. A laser beam is reflected by the cantilever and its reflection measured and interpreted by the quadrupole photodiode and following electronics. From [83].

In AFM, the investigated area is scanned point by point. This is done by moving the tip in parallel lines over the area. Consequently, the imaging process is faster parallel to these scanning lines (quick scan direction) than perpendicular to those (slow scan direction). Moreover, the resolution of the produced image depends on three different factors, each causing different inaccuracies: 1) The distance of two scanning points limits the digital resolution which equals the number of pixels. 2) The scanning and feedback speed limit the accuracy of height differences on the sample surface, since the feedback loop needs time to adapt to the height of a new scanning point. 3) Finally, the tip geometry must be adapted. If structures of atomic measurements are to be observed, the geometry of the tip must be at least the same size as the structures. Ideally, the tip is the the size of only one atom. Yet, such high precision during fabrication and handling of the cantilever is not easily manageable. Imperfections of the tip are bound to affect the resulting image.

With an AFM, there are generally three different measurement modes: contact mode, non-contact mode and intermittent mode. In contact mode, the bending of the cantilever due to repulsive forces caused by the Pauli principle (see figure 20) is measured. This mode can produce an atomic resolution, depending on the geometry of the tip, which lies between 1 nm and 10 nm. Two different scanning methods can be used to obtain the signal in contact mode: It is possible to either keep a constant height of the cantilever and

measure its bending through the resulting movement of the laser spot on the photodiode (see figure 19), or to keep the repulsive forces between tip and sample stable by varying the height of the cantilever. The latter requires a feedback loop that decreases the scan speed dramatically. CM is therefore only recommended for scanning flat and clean surfaces, so that damage to both the tip and the sample can be avoided.

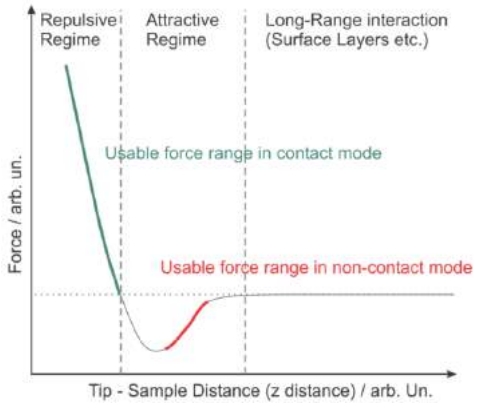

Figure 20: Curve of the Lennard-Jones Potential that results from the combination of repellent and attractive forces. From [84].

But since many of the samples investigated in the context of this thesis cannot be considered flat, the utilized mode is the non-contact mode. It uses the attractive force regime based on Van der Waals interactions (see figure 20). Consequently, the distance between sample and tip is bigger than for contact mode, resulting in less wear for both the tip and the sample. Compared to contact mode, the non-contact mode provides less resolution as the force range utilized is smaller. For this mode, the cantilever is put into a weakly damped forced oscillation with the frequency ω using a piezoelectric crystal. When the cantilever tip interacts with the surface atoms, the apparent spring constant of the forced oscillator changes, in turn changing the resonance frequency ω_0. As a result, a change of oscillation amplitude as well as phase shift between the the excitation signal and the probe's vibration can be detected [82]. The detection works best if the according change of signal is maximal. Hence, the cantilever is put into oscillation with a frequency near the resonance frequency of the cantilever, but slightly shifted. This is illustrated in figure 21 and ensures a maximal change of amplitude ΔA, the sign of which indicates the acting forces to be repulsive or attractive.

Again, a feedback loop is used to maintain the initial resonance frequency. Using an appropriate feedback loop for the conditions at hand is vital for the quality of the measurements. It can be necessary to adjust its parameters to prevent it from reacting too strongly or too slowly It can be influenced by the operator through adjustment of scanning parameters, such as scanning speed, and feedback parameters for the proportional (P), integral (I) and derivative (D) controller. Depending on the detected amplitude change, the PID controller gives an output voltage to the z-piezo calculated as

$$u(t) = K_\mathrm{P} \cdot e(t) + K_\mathrm{I} \cdot \int e(t\mathrm{d}t + K_\mathrm{D} \cdot \frac{\mathrm{d}e(t)}{\mathrm{d}t} \tag{14}$$

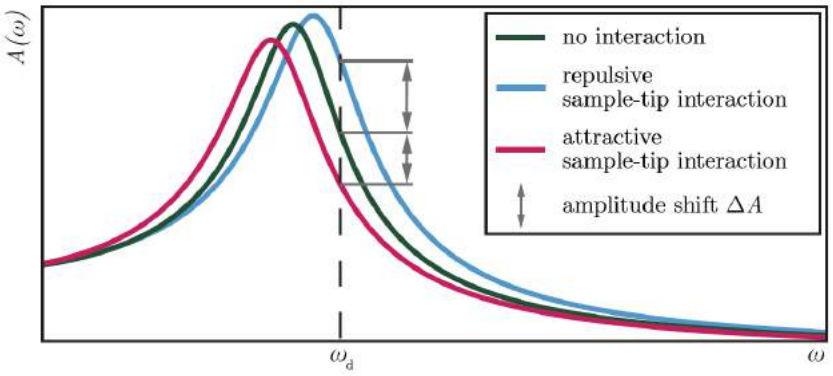

Figure 21: Amplitude in dependence of the frequency of the cantielver oscillation. As the driven frequency ω_d is tuned to be constant, the amplitude of the oscillation changes (ΔA when the tip interacts with the sample surface. The interaction-free case (green) is shown next to attractive sample-tip interaction (pink) and repulsive sample-tip interaction (blue). From [85].

with the difference signal $e(t)$ and the factors K_i for the respective feedback parameters [82].

The third measuring technique is measuring in both the attractive and the repulsive regime, called the intermittent contact mode. It is used to scan rough surfaces, by using a driven oscillation with an amplitude bigger than the distance between tip and sample [82]. Regarding wear of the cantilever tip, as well as resolution and scanning speed, this mode represents a compromise between contact mode and non-contact mode.

The AFM used for in this thesis is the *Nanosurf Flex AFM* in non-contact mode, using *Nanosensors*^{TM}PPP-CONTR cantilever tips. The obtained data was analyzed for surface roughness and grain size distribution using the software *Gwyddion*. For each sample, at least five spots were measured.

5 Results and Discussion

The structure of this section relates to the four research goals presented in section 1. The order has been slightly varied from their enumeration to provide better context for the research presented. Accordingly, all research involving RNIL is discussed in the first two subsections, followed by the functionalization experiments in the succeeding two sections.

5.1 Producing Structured Polymer Surfaces Using RNIL

Aiming for a structured polymer surface with no regard to the thickness of the underlying bulk material comes with a distinct advantage: The imprinting process gets significantly simplified. The major concerns hence lie with the design and fabrication of the master template as well as the mold. As these do not show significant problems throughout the thesis, this section mostly presents encountered minor issues and the adapted strategies to counteract them.

5.1.1 Influence of Master Template Design

The two MTs used for this thesis are portrayed in chapter 3.1. Here, their influence on experimental outcomes is displayed.

Influence of shape and dimensions

It is mentioned in section 3.3 that classic NIL utilizes capillary action to fill the mold with the imprint resist and that, naturally, capillary action can also be observed for the RNIL process. If adhesion between imprint resist and mold surface is weaker than the forces during spin coating, it can be observed that the structure cavities are only filled with resist in the corners. This observation is portrayed in figure 22, which shows an optical microscope (OM) image of the barely-filled cavity corners on a spin coated and cured mold (left) as well as these fragments being released if the extraction layer is dissolved in water (right). In these figures, the different filling mechanisms relevant for the NIL and RNIL imprint processes, respectively, are emphasized. The classic nanoimprint process (3.3) mostly relies on capillary action, which works well for sub-micrometer structures. However, when utilizing RNIL for the imprint of wider, micrometer-sized structures, stronger adhesive forces between resist and mold can be necessary. A multitude of imprint resists are commercially available for classic NIL [86], [87]. The experiments here show that their applicability cannot always be transferred to the RNIL technique. It can therefore be necessary to reconsider the chosen imprint resist or spin coat parameters, as the latter also have an effect on the mold filling.

Another influence of the shape and dimensions of the MT can be observed during particle release, which will be addressed in more detail in subsection 5.2. But because the observation is linked to the MT design, it is presented here. It was mentioned in chapter 3.3 that particle release occurs through breakage of the surrounding residual

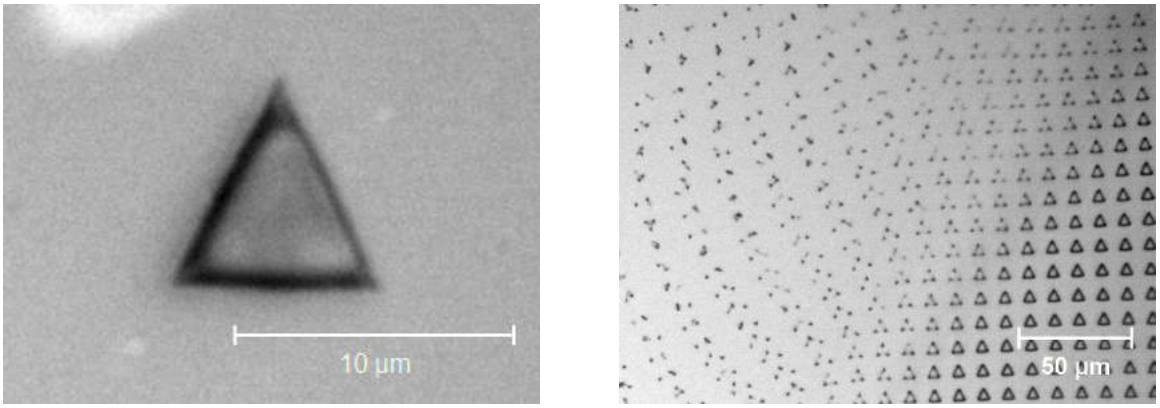

(a) (b)

Figure 22: OM images after imprint by spin coating. Here, the adhesive forces between imprint resist and mold were not strong enough to prevent the resist from being almost completely removed during spin coating. The only resist left after curing is located in the corners of the triangular cavities (left). If the PVA layer is dissolved in water, the release of these corners can be observed (right).

layer. This process can be seen in figure 23. It can be concluded that the distance of the structures as well as their orientation to one another have at least some influence on their release mechanics in water. The extent of this influence could be quantified by a series of tests comparing the release mechanism of structures of varying distance and shape while maintaining a constant RL thickness. However, the influence of the RL thickness strongly outweighs any impact of the breaking mechanism, which is why the former represents a major subject of research for this thesis.

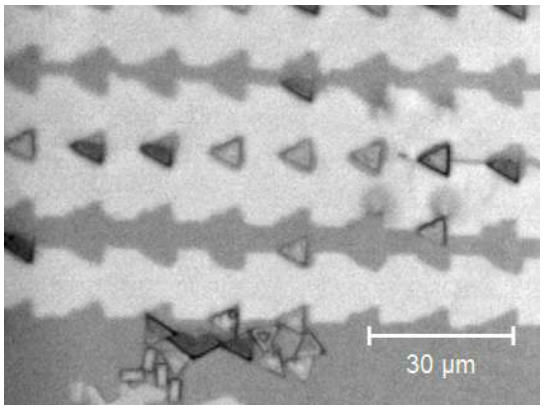

Figure 23: OM image of an imprinted polymer sample while its PVA extraction layer is dissolved in water. The breakage lines give information about the mechanics of the release process, a moment of which is captured in this photo.

Influence of structure arrangement

One reason for the production of the second 4-field master template was to achieve spatial separation of the differently sized structures. Using the 4-field arrangement, this separation can easily be achieved on the obtained PDMS mold using a scalpel and tweezers. The resulting four fields of the mold can then be imprinted, extracted, functionalized and - most importantly - characterized independently. The separation is beneficial for all characterization methods whose measurement area is comparable to the area of the structured fields. For a VSM, which measures the whole sample (subsection 4.1), the four fields can be measured separately compared to the 16-field design. For an L-MOKE magnetometer (subsection 4.2) the structuring of the samples leads to diffraction of the incident laser beam, influencing its reflection. Because this reflected beam determines the outcome of the measurement, its shape is vital. Figure 24 compares a 'bad' diffraction effect (caused by the 16-field MT) to a 'good' one (caused by the 4-field MT). The 'bad' diffraction is observed for a sample obtained using the 16-field MT, where the laser beam covers multiple structure fields. The reflected beam then contains information for all of those structures, which cannot be deconvolved. The diffraction pattern caused by the 4-field design can, in theory, be analyzed for all its information. For this, a Bragg-MOKE magnetometer can be employed, which is not available at the University of Kassel. With a Bragg-MOKE, Kerr hysteresis loops can also be measured at the diffraction spots of different order [88], providing valuable information about the mean lateral magnetization distribution.

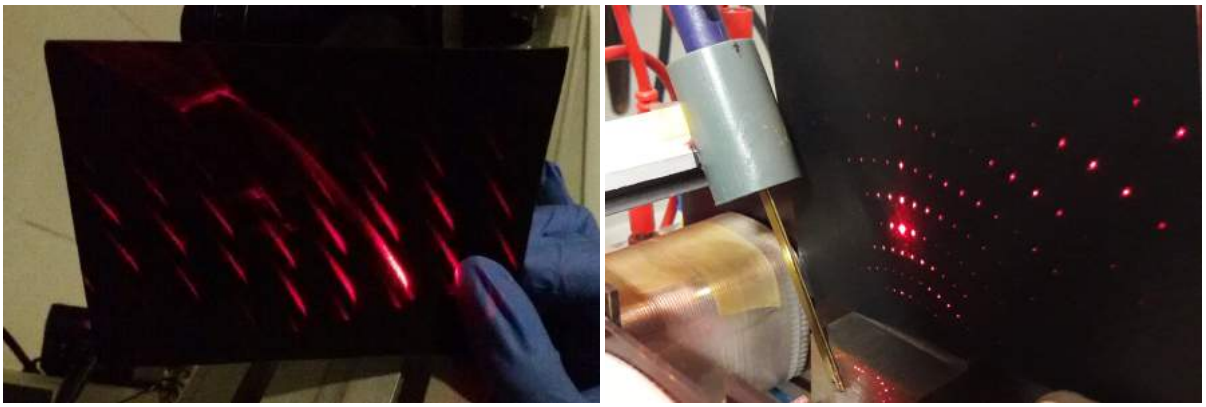

(a) (b)

Figure 24: a) L-MOKE magnetometer setup for measuring a sample obtained using the 16-field MT. Due to surface roughness and diffraction of the laser beam on differently sized structures, the reflected beam loses its shape. b) The same setup for a sample obtained using the 4-field MT. The zero order beam reaches the diode.

5.1.2 Optimizing the Molding Process

The general fabrication process of the PDMS mold as well as its purpose are explained in subsection 3.2. During the thesis, two adaptations have been made to optimize this step, which are now discussed.

As the PDMS is applied manually, its distribution between the MT and the glass substrate is usually inhomogeneous when the substrate is placed. An interplay of the sudden spatial confinement and capillary action causes the liquid PDMS to change its distribution. This results in a nearly complete wetting of the MT, independent of the original distribution of the PDMS drop and its volume. A complete wetting is generally desired, as it eliminates the necessity for high accuracy regarding the aforementioned parameters volume and original distribution, which is why it can be performed by hand.

Yet, this process can also cause two undesired outcomes, which figure 25 illustrates: A tilted mold and/or a solidified film of PDMS gluing the underlying substrate and the MT together. The former is often, but not always, caused by a too little amount of PDMS and the systems aim to minimize its surface energy. If the amount of PDMS is smaller than the volume between MT and glass substrate, the system favors a reduced setup volume over empty space, hence pulling the only flexible boundary - the MT - closer to the glass substrate. After polymerization of the PDMS mold, it is possible that the tilted mold cannot hold the imprint resist, thereby complicating its handling or eliminating its use for this purpose entirely.

If, on the other hand, too much PDMS is poured onto the MT, confining it with the glass substrate will cause the liquid to spill over and embed the MT. After polymerization, it can be hard to separate the setup from the underlying substrate, rendering the safe retrieval of mold and MT difficult. In an unfortunate case, these two problems can occur simultaneously. If a large volume of PDMS is poured close to an edge of the MT, parts of the liquid can spill over immediately after glass substrate positioning, leaving an insufficient amount between MT and glass substrate. This in turn causes the tilt of the MT, enabling the spilled PDMS to flow underneath. After polymerization, the now completely enclosed PDMS acts as glue between MT and underlying substrate. Only very patient and careful action can then prevent damage to the MT upon separation, which is performed manually and mechanically.

These events rarely occur in the problematic manner described above. Usually, a slightly tilted mold or limited amount of excess PDMS have little effect on further procedures. But with the molding process requiring one day to finish and, moreover, a re-creation of the MT requiring considerable effort (see 3.1), two simple adaptations have been implemented to avoid any occurrence of these issues whatsoever. The first adaptation solves the problem caused by excess PDMS by replacing the underlying aluminum substrate with a material easily separable from the polymerized PDMS. During this thesis, sheets of silicon and Teflon® have been investigated with the finding that both provide the intended benefit. Towards the end of his thesis, *Burhan Kaban* found commercial baking paper to provide the same advantage, presenting an even easier-to-handle and cost efficient candidate for the underlying substrate. The second adaptation involves weak attachment of the MT to the underlying substrate using either double-

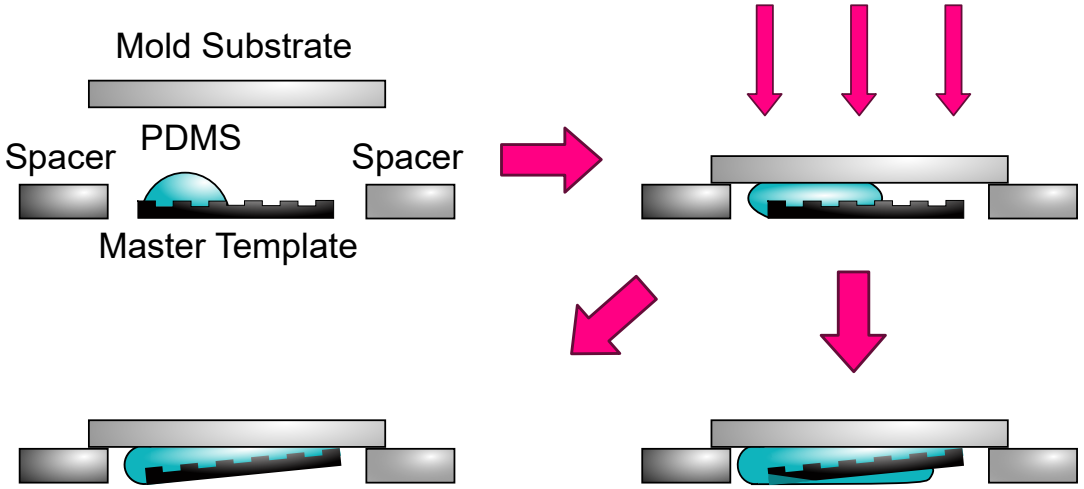

Figure 25: Schematic visualizing how the default method for molding can lead to two undesirable outcomes. Unfavorable addition of PDMS can occasionally result in a tilted mold and complicate safe retrieval of the MT, if PDMS polymerizes underneath.

sided tape or small drops of PVA on the corners of the MT, which can be hardened within one minute before the use of PDMS. The attachment achieved this way is weak enough to be easily reversed after the process, but strong enough to prevent the MT from tilting. This not only prevents the MT from getting strongly glued to any substrate material, but also ensures that every mold fabricated is level and can be used for the later imprinting process. Naturally, both solutions can be combined to ensure safe retrieval of the MT in a case where one or the other step is skipped, be it intentionally or unintentionally.

It can be concluded that applying either one of the adaptations or both of them combined provides a cheap, easy and efficient way to ensure that every mold fabricated can be utilized and, more importantly, that the process of MT retrieval poses as little danger to it as possible.

5.1.3 Imprint and Extraction - Results and Method Modifications

One of the benefits of RNIL over classic NIL is the thin RL of imprint resist remaining after the imprint process (see 3.3). However, the first research goal of producing a structured polymer surface using RNIL does not require a thin residual layer. In consequence, the step of spin coating the resist onto the mold becomes optional. Choosing to skip this step simplifies the imprint process and the parameters involved. A drop of imprint resist can simply be cast onto the mold and then thermally cured for an increased amount of time compared to spin coating the resist. This is simply due to the higher volume of resist remaining on the mold. For this method, the necessary curing time naturally depends on the amount of drop cast resist. To ensure complete curing of less than five drops, 60 minutes in an oven or on a hot plate at 115 °C have proven sufficient. Afterward, the imprint is extracted via PVA extraction layer as described in subsection 3.3.

The resulting PMMA film contains the structure of the MT on its surface, which can then be analyzed and/or processed further.

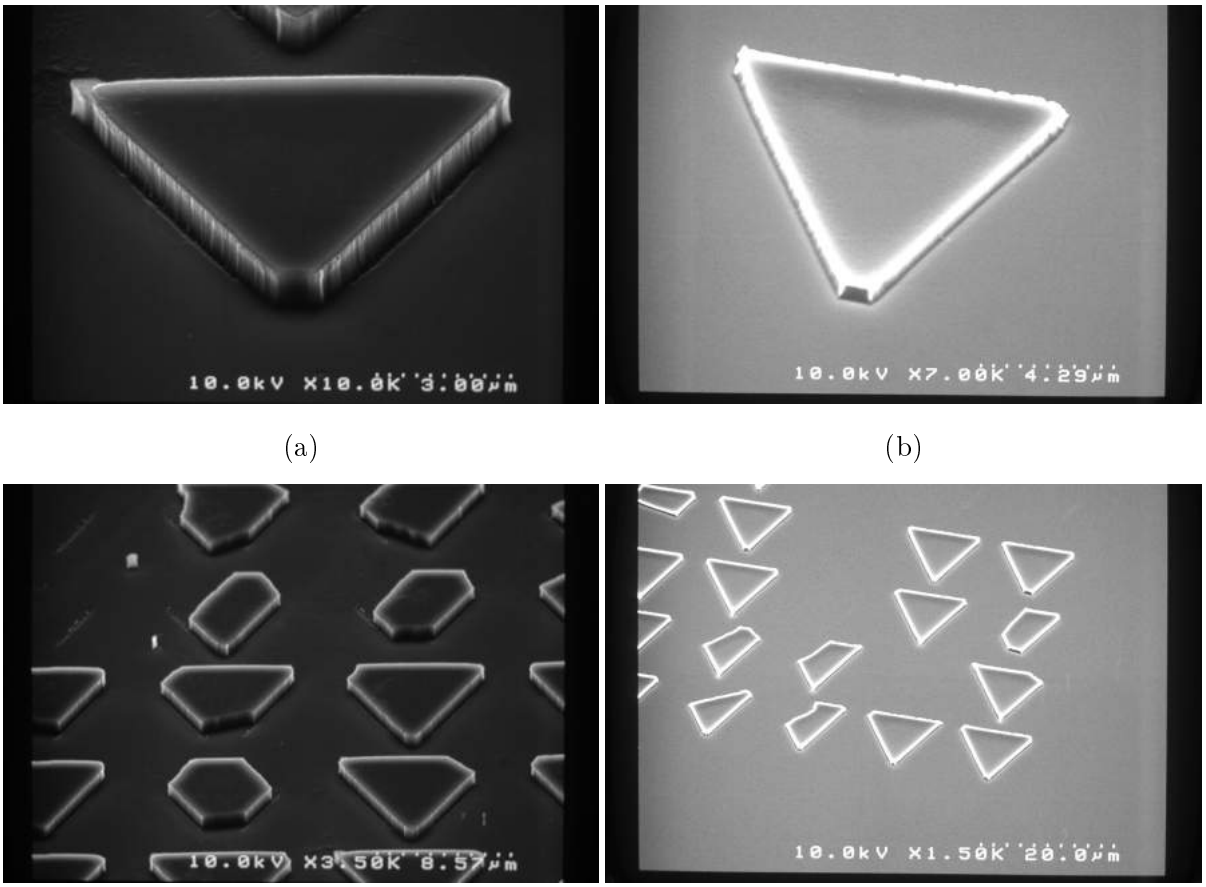

(a) (b)

(c) (d)

Figure 26: SEM images comparing the structures of the MT (a and c) to the structures obtained via RNIL using drop cast imprint and extraction (b and d). The errors of the MT (see section 3.1), visible, for example, in the broken edges, are transferred to the imprinted structures. Using the structure walls, the resolution of the imprint was determined to be smaller than 100 nm.

Figure 26 compares characteristic SEM images of the original MT and the imprinted polymer structures. It can be seen that the imprint copies the MT structures very accurately. A nanometer scaled structure for exact resolution quantification was not implemented. When examining the resolution of the structure walls, however, the imprint resolution can be determined to be smaller than 100 nm, which can be expected based on the literature [24, 89].

Modifications due to observed sample curling

Samples fabricated as described so far can be observed to curl up after several hours or even minutes of storage. This is likely to be caused by changing moisture of the PVA

layer, which is permanently exposed to the surrounding air. This curling is problematic for sample characterization. Curled up areas can yield distorted results during imaging techniques like OM, SEM or L-MOKE (after sputter deposition) or, depending on the degree of curling, even prevent imaging of these areas altogether. Sputter deposition on these areas will lead to inhomogeneous or failed coverage, and AFM cantilevers cannot compensate such high degrees of height difference. Because flat samples are required, the extraction process has been modified to prevent curling of the PVA extraction layer. Instead, the drop cast resist is brought in contact with the sample substrate (glass or silicon) during its curing. Two different approaches have been tested and are illustrated in figure 27.

The first method holds the setup together via two binder clips after the resist is

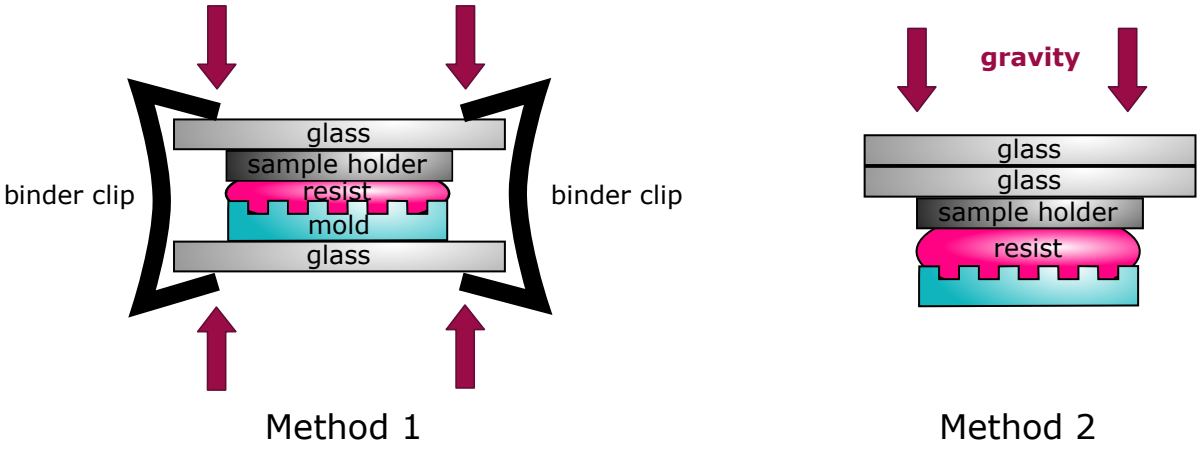

Figure 27: Schematic of the two different methods for imprint and extraction via drop cast, both resulting in a thick RL. In method 1, the mold, imprint resist and sample holder are pressed together by binder clips during thermal curing in the oven. This method was found to squeeze out nearly all of the resist. In method 2, less pressure is applied by adding weight to the sample holder during thermal curing on a hot plate, resulting in more homogeneous resist distribution after curing.

drop cast. Due to the elevation, the thermal curing has to occur in an oven. This method is found to be flawed. The pressure caused by the binder clips squeezes out most of the resist solution, often resulting in incomplete wetting of the mold. This problem is aggravated by the strong adhesion between resist solution and glass/silicon substrate, all three being hydrophilic. For the second method, the setup can remain on a hot plate. The glass/silicon substrate is also applied during the resist curing process, but only medium pressure is applied by securing the substrate with two additional glass substrates. This is advantageous because the pressure is strong enough to enforce complete wetting, but not strong enough to squeeze out the resist solution. Curing for 24 hours at 115 °C compensates for the lack of air contact to the resist, leading to a flat sample as can be seen in figure 28.

Although the different imprint-and-extraction method presented in this subsection turns the curing step into a 24 hour process and adds some sensitivity to the applied

(a) (b)

Figure 28: (a) shows an imprinted PMMA film extracted via PVA foil and stored on a glass sample holder. Due to changes in moisture of the film, it curls up at the edges, which represents an undesired event. (b) shows an imprinted PMMA film extracted using PVA and double-sided tape, which is clearly visible underneath the transparent PMMA/PVA foil, stored on a silicon sample holder. The film is prevented from curling up.

resist volume, the resulting benefits from the homogeneous height of the sample outweigh the disadvantages. It reliably leads to a sufficiently flat sample and has therefore been favored in this thesis. It is henceforth referred to as 'silicon extraction', to be distinguished from the other extraction methods introduced in the methods section 3.3 or explored in the results section 5.2.5.

5.2 Producing Shaped Polymer Particles

Producing releasable polymer particles using RNIL requires a very thin residual layer of imprint resist during the imprinting process. Consequently, the imprinting method of drop casting the resist, described in section 5.1.3, must be replaced. This, however, results in a higher complexity of the imprinting process, requiring further optimization of the parameters. Similarly, this can be said for the extraction process following the imprinting step. This subsection therefore focuses on the experiments performed to enable and optimize these two process steps.

Three major factors can be identified when regarding the imprinting process: the resist, the mold, and the spin coating process, which appear as subsections in this chapter. The general approach during the research phase was to vary a property of either the mold or the resist and test the outcome for several spin coating parameters, to provide comparable data sets.

Section 5.2.1 begins with experiments involving the imprint resist, continuing with tested mold treatments thereafter in section 5.2.2. A short comparison of the tested methods is offered in section 5.2.3. With a successful imprint process established, section 5.2.4 deals with its optimization. Section 5.2.5 then lists a number of investigated extraction methods, thereby concluding all research involving polymer shaping using

RNIL.

5.2.1 Improving Resist Adhesion - Varying Resist Properties

Varying stock solution

In an attempt to find a solution not requiring any additional processing steps, commercially available stock solutions that were already at hand during the thesis have been tested as imprint material. This series of tests has been done during the preparatory project preceding this thesis and found the resist AR-P 639.04, a positive PMMA e-beam resist by the company *Allresist GmbH*, to be the most promising among other resists made by the same manufacturer.

These tests do not represent the content of this thesis, but the following briefly discusses possible improvements on these experiments since understanding the reason for this finding could enable determination of a more suitable material. The resists were previously judged by their interaction with the mold during spin coating, which presents a criteria that is hard to quantify. One method that could be used to investigate this in more detail is contact angle measurement [90]. Comparing the contact angles between the respective stock solutions and the PDMS mold surface provides information about the strength of their adhesion, which correlates with the wetting during spin coating. The properties of the stock solutions could then be plotted against their respective contact angle to conclude which properties are beneficial. Each stock solution has a number of properties: solvent, viscosity, solids content, chain length, etc. But, in accordance with the *Young* equation [91], the dominant factor regarding the contact angle in this setup is the surface tension of the solvent. Reducing the tested liquids to the solvents, instead of also using the PMMA stock solutions, would simplify the interpretation as well as render the series of tests significantly cheaper.

It is, however, questionable if these efforts would result in a significant advancement. On the one hand, the solvents used for the resists evaporate rapidly, rendering reproducible contact angle measurements rather difficult. On the other hand, if the surface tensions of the solvents are considered, the stock solutions can be easily compared using literature values without the need for time consuming test series. Table 1 compares the investigated stock solutions accordingly, including their respective viscosity. Considering the hydrophobicity of PDMS, it can be assumed that a lower resist surface tension results in a lower contact angle and, therefore, better adhesion. The resist formerly found the most promising, AR-P 639.04, is among the lowest surface tension for its solvent as well as the lowest viscosity. Taking this into account, combined with the little improvement observed by varying the resists, further investigation in this direction seems unpromising. Hence, the resist AR-P 639.04 remains the imprint material utilized in this thesis.

solvent	**surface tension at 20 °C in [mN/m]**	**viscosity at 25 °C in [mPas]** [1]
ethyl lactate	30.0	2.2
1-methoxy-2-propanol	28.0	20
chlorobenzene	33.5	-
anisole	35.0	15.5

[1] referring to the respective stock solutions at hand

Table 1: Properties of the stock solutions at hand, listing their respective solvent, the solvents surface tension and the viscosity of the stock solution [92, 93]. Butyl lactate, which is the solvent of the favored resist, AR-P 639.04, is among the lowest surface tension as well as the lowest viscosity, making it the best candidate for spin coating on PDMS.

Mixing the resist with DCM:EtOH

In his master thesis, *B. Kaban* used a combination of dichloromethane (DCM) and ethanol (EtOH) to dissolve a fluorescent polymer[2]. before spin coating it onto a PDMS mold [94]. Although the polymer that was dissolved was not PMMA, its success in coating a PDMS mold renders it interesting for this thesis. Accordingly, a DCM:EtOH solution has been added to the PMMA stock solution before spin coating the combination onto a mold.

Two varieties of DCM:EtOH have been tested: Following the method of *B. Kaban*, 5 *wt*% PMMA stock solution have been added to a DCM:EtOH solution of either a nine-to-one ratio or one-to-one ratio. After spin coating the mixture, the distribution of the hardened PMMA on the mold was found to be very irregular. For the nine-to-one ratio, the 16-field mold in figure 29a is representative for observing mostly unfilled area. Some areas show at least partial filling indicated by darker shading (bottom and right), while the very dark spots prove the aforementioned irregular PMMA solidification. This undesired irregularity, which also comes with a thick residual layer, appears even stronger in the samples using one-to-one ratio of DCM:EtOH, as portrayed in figure 29b. A close-up of the irregular filling is displayed in figure 29c. If extracted via PVA and dissolved in water, some released particles can be seen (figure 29d). When looking at the shading and shape of the particles, it is evident that the zig-zag structures have a better structural integrity than the bigger triangles. This can be interpreted as the larger triangles being filled less, giving only their corners structural integrity due to capillary action described in section 5.1.1. Because the zig-zag structures are smaller and have more corners, this effect has a bigger influence.

In summary, mixing the stock solution with DCM:EtOH showed some improvement. Yet, due to the high irregularity of the outcome combined with the little improvement regarding large scale mold filling, the need for a better method remains pressing.

[2] The polymer is a europium based complex of the chemical formula $\{[Eu(NO_3)_3]_2[C_{26}H_{40}O_6P_2]_3\}_n$. Details in [94] and [95]

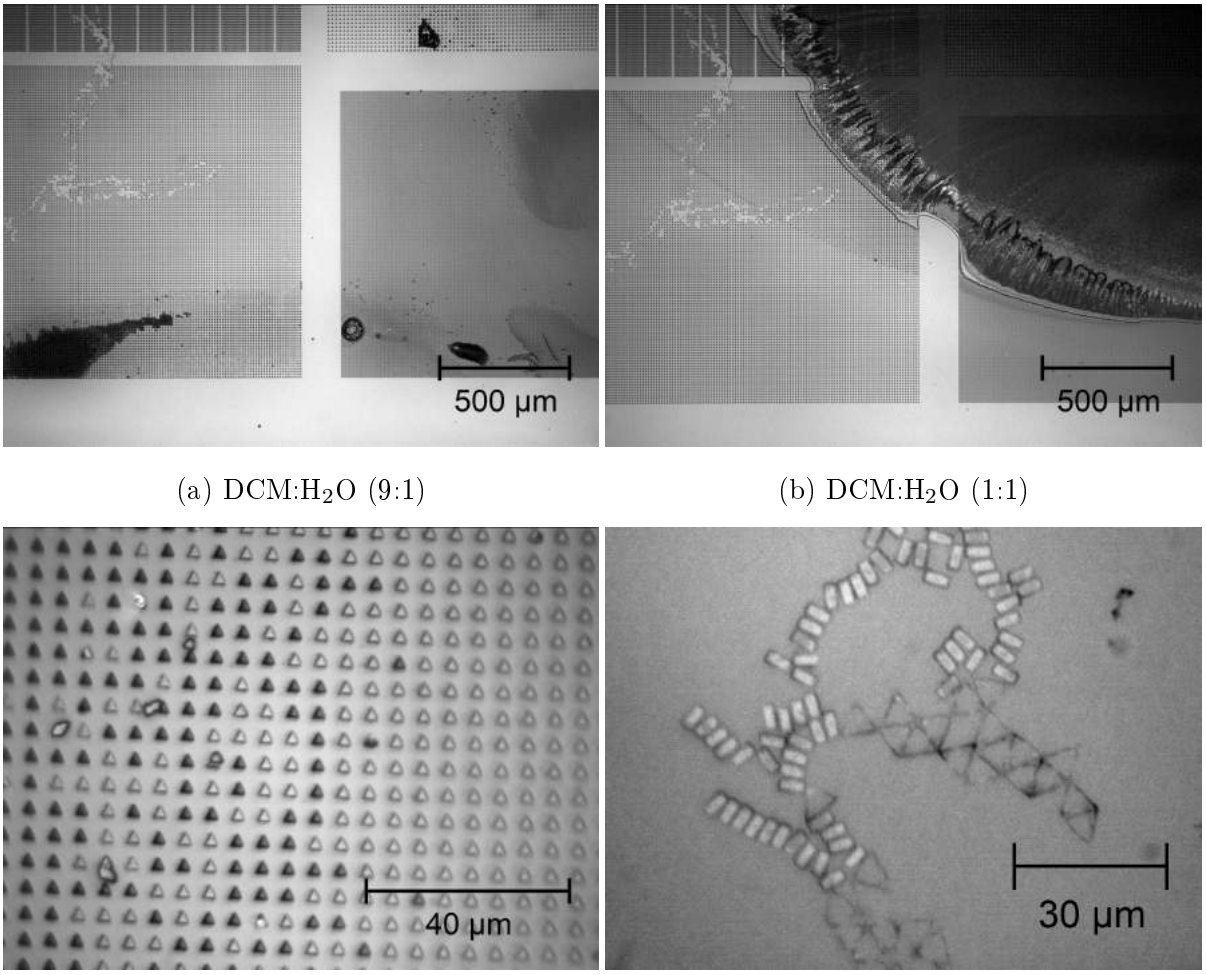

(a) DCM:H_2O (9:1)

(b) DCM:H_2O (1:1)

(c) DCM:H_2O (9:1)

(d) DCM:H_2O (9:1)

Figure 29: Mixture of PMMA stock solution with DCM:EtOH in two ratios. Neither result in a homogeneous filling of the mold cavities on large scale (a and b) or on small scale (c). The limited number of filled cavities can be released in water (d).

Mixing with water

Another method employed by *B. Kaban* during his thesis was that of mixing the PMMA stock solution with water [94]. This method has therefore been explored for this thesis as well.

Ratios below 17 *wt*% water have been found to show no lasting phase separation, which is described as crucial for the intended effect by *Kaban*. This observation fits well into *Kaban's* recommendation of 20 *wt*% water. Keeping the ratio as low as possible appears reasonable, since neither ethyl lactate nor PMMA are soluble in water [93, 96]. To form an emulsion, the two phases are mechanically mixed through manual shaking and treatment in an ultra sonic bath for 1 min. Regarding the results of this method, portrayed in figure 30, the distribution of PMMA on the mold is again highly irregular and varies from sample to sample. Big, small and medium-sized areas of differently filled cavities are observed. They usually encompass blobs of residual layer of similar size differences. Introducing a delay time of 5 minutes to 10 minutes as well as ranging the spinning velocity between 3000 rpm and 4000 rpm shows no significant difference in outcome.

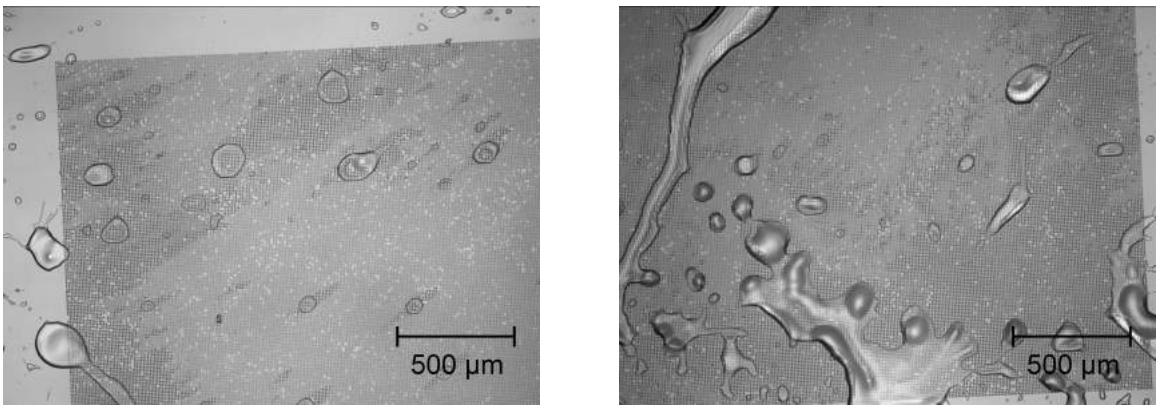

Figure 30: Two OM images of the spin coated mold after mixing the stock solution with 20 % water. Areas of filled cavities, characterized by darker shading, as well as thick residual layers vary greatly in size, shape and frequency.

The method of mixing the stock solution with 20 % water shows increased filling of the mold, often resulting in relatively large areas of several dozen or even hundreds of cavities. Since the necessary analysis via optical microscopy, fluorescence microscopy or scanning electron microscopy only requires small areas, the approach provides a sufficient amount of releasable particles to be analyzed for a successful guest-host-functionalization, as pursued in *Kaban's* work [94]. In contrast, this thesis aims to deposit an EB layer system on top of the whole sample area. It is therefore desired to find an imprinting method that fills the cavities of the mold as homogeneously as possible. For this purpose, while acknowledging the advancement achieved by utilizing a water emulsion, further attempts to improve the imprint outcome have been undertaken and are presented in following subsections.

Improving the mixing experiments

One obvious flaw can be pointed out regarding the approach of mixing the PMMA stock solution with other solvents: The experiments are based on the hypothesis that a different solvent could improve adhesion. It would therefore be reasonable to test the respective solvent without the influence of the solvent of the stock solution. To do so, instead of mixing the stock solution with other solvents, solid PMMA powder could be dissolved in the respective solvent. This approach can therefore be regarded as an extension of the experiments involving different stock solutions. To obtain a reasonable set of data, a number of suitable solvents would have to be determined first. Many solvents are known to dissolve PMMA. Esters, ketones, aromatics, glycol ethers and more are listed in the literature, in addition to ethyl lactate and DCM [96–98]. As PDMS is hydrophobic, the same property could be used as sorting criteria. Other criteria include price and toxicity. The remaining candidates would then be investigated for their adhesion to PDMS via contact angle or added to PMMA powder and spin coated. It is reasonable to assume that the commercially available PMMA stock solutions already take this research into consideration, although selected regarding their adhesion to silicon wafers instead of PDMS. In any case, as this approach is an extension of the stock solution experiments, it is likely the effort required to conduct this research outweighs the potential benefits. For this reason, the thesis hereafter presents experiments involving surface treatment of the PDMS mold.

5.2.2 Improving Resist Adhesion - Mold Surface Treatments

The adhesion between imprint material and mold has proven too weak for proper wetting after spin coating. Chapter 5.2.1 represents the attempt to solve this issue by adapting the utilized imprint material. With the goal to further improve resist adhesion, this subsection addresses the second player of this interaction: the PDMS mold. Instead of finding a different solvent for PMMA, this approach aims to improve adhesion by change of the mold surface. Several ways to achieve this are proposed in the literature, a selection of which has been tested for this thesis.

Application of the adhesion promoter Ti-Prime

The adhesion promoter TI-Prime was applied to the mold surface. The highly diluted organic titanium compound is used to chemically bind to polar OH-bonds that form on surfaces exposed to air and humidity [90]. It thereby counters oxidation and improves adhesion to hydrophobic resists. The series of tests utilizing TI-Prime initially showed very good results. This is documented in figure 31a and b, showing a successfully imprinted mold and a multitude of particles released in water, respectively. Repeated failure to reproduce the results on newly produced molds, however, led to the conclusion that a different cause was responsible for the good wetting. The approach of using the adhesion promoter has thus been abandoned. Still, the positive results - complete wetting of the mold while showing a residual layer thin enough for particle release - were induced by some other effect that was now to be identified. It was hypothesized that aging of the

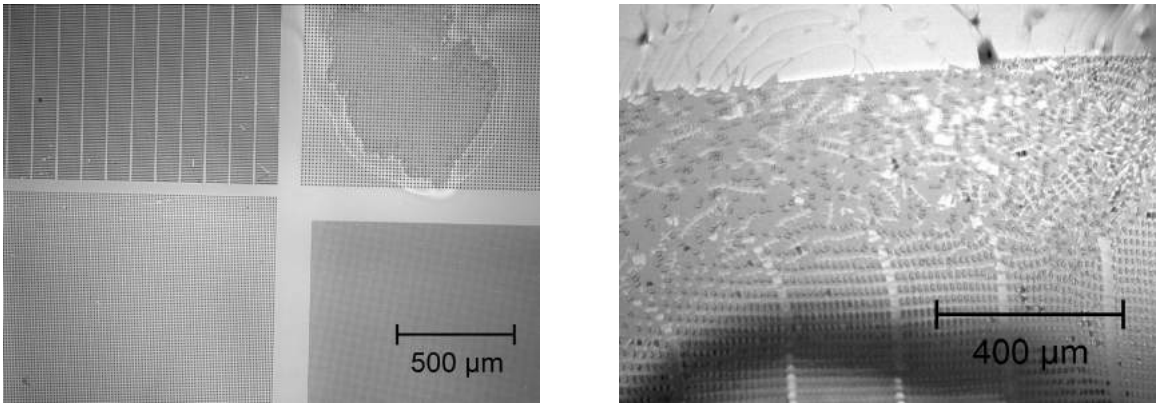

Figure 31: Left: OM image showing a successful imprint after mold treatment with the adhesion promoter TI-Prime. An empty area in the top right field allows comparison of coated and empty area. Right: A polymer film obtained after PVA extraction during contact with water. The release of PMMA particles into the water upon PVA dissolving can be observed.

molds over several weeks leads to an oxidized surface, in turn increasing resist adhesion. This effect should be countered or at least weakened through application of TI-Prime, which exists precisely for this purpose. Nonetheless, this hypothesis was pursued, leading to further efforts to optimize hydrophilic surface treatments, as presented next.

Oxygen plasma for a hydrophilic mold surface

Based on previous experiments, it was hypothesized that a hydrophilic surface treatment of the PDMS mold would be beneficial for resist adhesion during spin coating. In the literature, exposure to an oxygen plasma is proposed as a possible hydrophilic treatment for PDMS [99, 100], among others. Using oxygen as an oxidant also corresponds well to the above formulated hypothesis. To create the respective plasma environment, the low-pressure plasma system *Nano* by *Diener electronic GmbH* was used. Starting with 70 % intensity for 5 minutes, the treatment proves to be too aggressive, causing widespread cracks on the mold surface that are visible by eye. Simultaneously, good mold filling can be observed after spin coating of the PMMA solution (figure 32a) and confirmed through particle release in water (figure 32b). Unsurprisingly, the mold does not remain undamaged. Extraction via PVA also rips out parts of the mold, as is displayed in figure 32c and figure 32d.

Consequently, a series of tests aiming to optimize the plasma treatment parameters has been done. Reducing the plasma duration to 1 minute leaves the mold intact at first. After PMMA extraction, however, the mold becomes damaged. The plasma duration was then gradually decreased from 5 minutes down to just 3 seconds. Continuing to decrease the time while maintaining reproducible circumstances is impossible, as the device can take several seconds to stabilize the plasma. Still finding the mold to be damaged, the plasma intensity was reduced first to 40 % and then to 15 % without

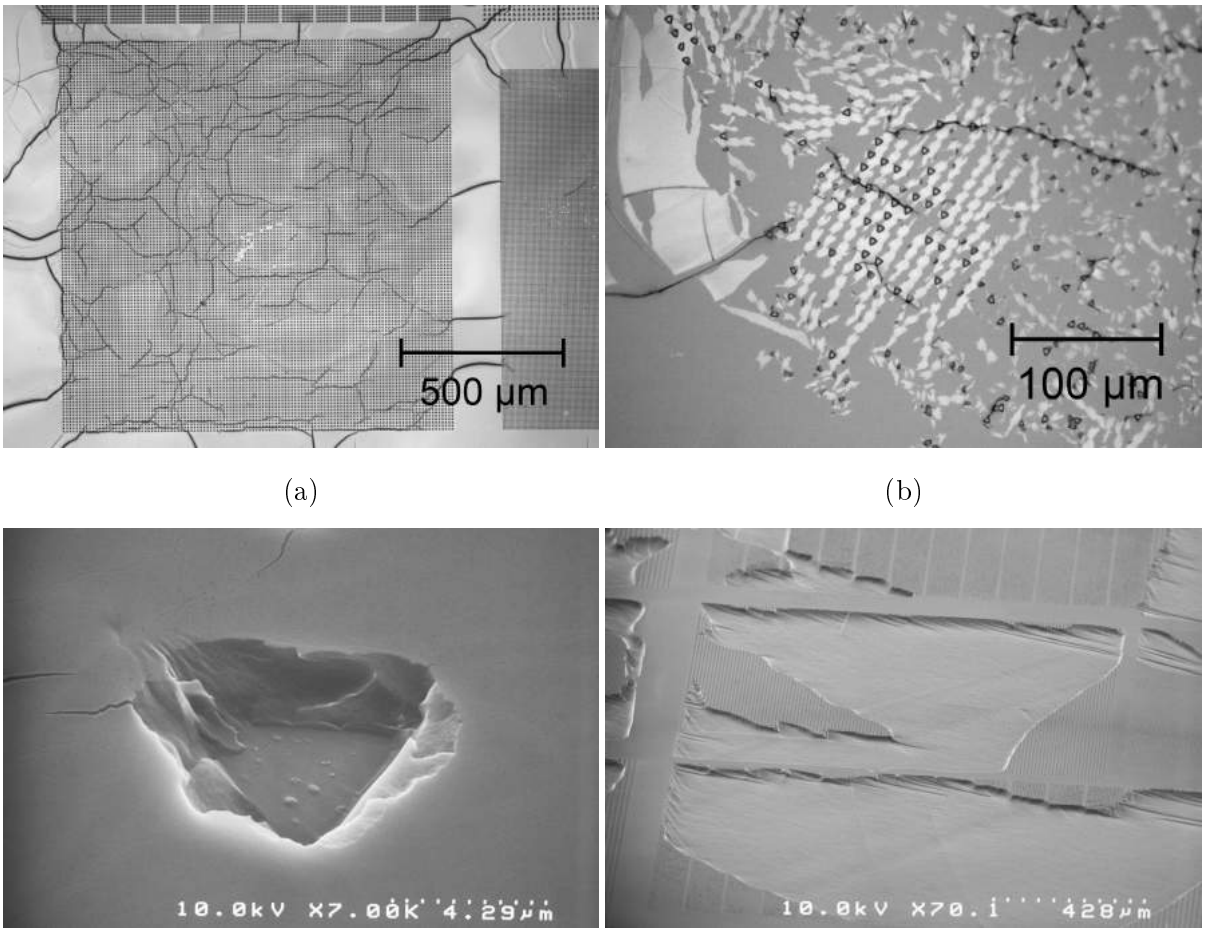

(a) (b)

(c) (d)

Figure 32: Optical microscope (a and b) as well as SEM images (c and d) documenting the damage to an oxygen plasma treated hybrid mold when used for the RNIL process. a) shows the spin coated mold after curing, which shows very good filling as well as severe cracks at the mold surface. b) shows the extracted PMMA/PVA film in water. After PVA is dissolved, large areas of extracted material are visible, consisting of both PMMA and ripped out PDMS. c) shows a close-up SEM image of a damaged mold cavity after PMMA extraction, while d) shows large areas being ripped off the mold.

showing any improvement of the mold integrity. It can be concluded that even relatively short treatments of less than 5 seconds have a strong effect on the surface parameters of PDMS. This finding corresponds to the literature. *Owen et al.* investigated the atomic composition of a PDMS surface treated with oxygen plasma via X-ray photoelectron spectroscopy (XPS) [99]. As table 2 illustrates, they found the surface composition to change significantly within one second of treatment while showing no significant change in composition for longer treatment up to 10 minutes.

Treatment time (s)	**Atomic composition (%)**		
	O	C	Si
0	27.1	50.3	22.6
1	43.2	34.4	22.4
5	43.5	34.7	21.8
10	45.1	32.0	22.9
30	46.5	29.7	23.8

Table 2: XPS surface analysis of oxygen plasma (70 W) treated PDMS. Taken from [99].

When looking at the SEM images of destroyed molds (figure 32d), an even and limited depth of the damage can be determined. This raised the hypothesis that only the superficial h-PDMS layer gets damaged by the plasma treatment, while the underlying s-PDMS remains intact. To test this, a PDMS mold was fabricated solely out of s-PDMS and treated with oxygen plasma. It was found that even after several imprint-and-extraction cycles the mold remained both fully coated and fully intact. To minimize wear on the mold while maintaining reproducible conditions, the ideal plasma parameters were found to be the following: The plasma duration is set for 10 seconds at a plasma intensity of 40 % while the mold is placed in a Faraday cage to protect it from accelerated ions. After this process the mold can be used for RNIL for several days before its hydrophilic character begins to wear off. Literature describes recovery of hydrophobicity to occur by diffusion of untreated polymer chains through cracks in the treated layer [99]. The time frame for this recovery varies between sources from hours [101] to days [102, 103] and weeks [104, 105]. The molds here show no significant hydrophobic recovery until at least one week after treatment.

One disadvantage of this method, apart from its dependence on s-PDMS molds, is the strong interaction of the treated mold with PVA that is applied for extraction. The adhesion to PVA exceeds that of the imprint material greatly, so that any PVA in direct contact with the mold will rip out these parts of the mold upon extraction. As wetting of the mold with imprint material is not always absolute, this will lead to increased damage to the mold over time, although mostly in its periphery. This emphasizes that oxygen plasma treatment of the mold is beneficial when using PMMA as imprint material. For more hydrophilic imprint materials, however, this approach can have destructive effects.

Still, this represents a major advancement and is the key to successful and large-scale PMMA particle fabrication using the RNIL method that is subject of this thesis. The

problem of weak adhesion is hereby identified as the mold surface being too hydrophobic, making the proposed hydrophilic surface treatment viable as long as the mold consists of s-PDMS.

Oxygen gas as hydrophilic surface treatment

A successful imprint that leads to releasable PMMA particles is achieved by exposing a mold fabricated out of s-PDMS to oxygen plasma before spin coating. However, using a hybrid mold made of h-PDMS and s-PDMS is advantageous over the use of s-PDMS molds (see 3.2). It is, thus, preferable to find a solution that allows the use of h-PMDS. In other words, less aggressive options for hydrophilic mold treatments should be explored.

The first of the options explored is based on the hypothesis that led to the use of oxygen plasma in the first place. This hypothesis holds oxidation through extended exposure to air responsible for the initial advancements observed. In an attempt to imitate these conditions, the mold is exposed to pure oxygen gas. Hypothetically, oxidizing through pure oxygen gas happens faster than exposure to air while being much less aggressive than oxygen plasma. Exposure to oxygen gas was also realized using the low-pressure plasma system *Nano* by eliminating the plasma phase and increasing the gas flooding phase to the intended exposure duration. A series of tests were carried out for 1 minute, 5 minutes, 15 minutes and 45 minutes of exposure time. None of these exposure times led to a visible improvement of mold wetting. Consequently, either the exposure time has to be increased to achieve a significant oxidation, or oxygen gas is not strong enough to oxidize PDMS.

UV light as hydrophilic surface treatment

Other PDMS surface treatments encountered in literature are ultraviolet (UV) radiation and ultraviolet/ozone (UVO) treatment [106]. *Efimeno et al.* found that when exposed to UV, PDMS molecules undergo chain scission. In the presence of molecular oxygen and ozone, these radicals form a large number of hydrophilic groups, decreasing the contact angle to water to about 10°. Alternatively, if the setup is flooded with nitrogen, the radicals recombine and form a network that is slightly more hydrophilic. The contact angle to water is reported to decline from 110 ° to roughly 90°. The strength of the effect depends highly in treatment duration, as determined by *Efimeno et al.* and illustrated in figure 33.

UV exposure under nitrogen gas represents a significantly weaker surface treatment compared to oxygen plasma while still providing improved wetting. It is hence tested in this thesis. The UV light was supplied by a mercury lamp. Molds are treated for 45 minutes, 60 minutes and 90 minutes and then spin coated with PMMA solution at 3000 rpm after 5 minutes of delay time. After 45 minutes, almost no improvement to untreated PDMS is observed (figure 34a). Only randomly appearing PMMA blobs and small surroundings of filled area occur. The data taken after 60 minutes of treatment

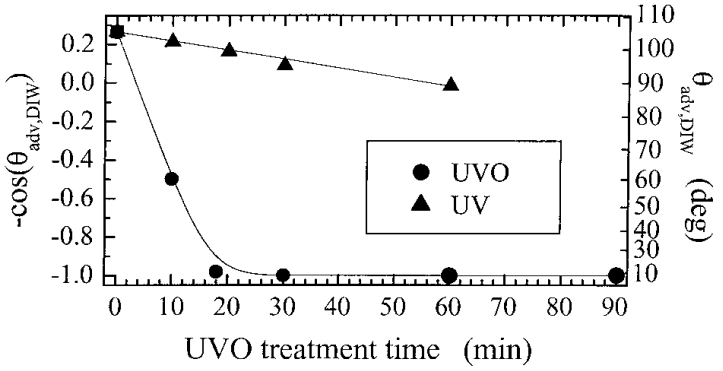

Figure 33: Dependence of the advancing contact angles of deionized water ($\theta_{adv,DIW}$) on the UVO treatment time for PDMS exposed to UVO (circles) and UV (up-triangles). Edited from [106].

is slightly more promising. The resulting PMMA blobs appear more frequently and in increased sizes, and large areas appear in slightly different shades compared to empty areas, suggesting at least some cavity filling (figure 34b). As expected, the longest treatment time of 90 minutes shows even more wetting. Thick PMMA layers cover an estimated 25 % of the mold surface while almost all other areas show at least some degree of filling (figure 34c). Translating observed triangle shading into filling quantity is impossible at this stage. Only relative information can be given when comparing some cavities to others, like for figX b. Accordingly, to gain more information about filling quantity, the behavior of the samples in water is observed (figure 34d). This revealed triangles that were barely visible and cavity filling that was minimal.

Although UV treatment is observed to have a more homogeneous effect than the methods tested above, the results depicted above suggest that it can bring about only limited improvement on cavity filling compared to untreated PDMS. Still, there is evidence to suggest that even longer UV treatment, possibly combined with other imprint parameters, could further improve wettability. However, this was not tested, as the focus of research at this point shifted to the functionalization part of the thesis. But because this treatment results in a resist adhesion insufficient for suitable particle thickness, it is not an ideal method for the purposes of this thesis.

A conclusion of the methods tested and possible further research will be discussed in the following chapter.

5.2.3 Comparison of the Tested Methods

Varying the PMMA stock solutions provided nearly no improvement of wettability.

Mixing the stock solution with dichloromethane (DCM) leads to minimal benefits in cavity filling accompanied by highly irregular distributions of filled and empty cavities and thick residual layers. As this produces a minimal amount of releasable particles with sufficient thickness, this method is discarded as a viable option for adhesion improvement, although further tests dissolving solid PMMA in DCM with succeeding dilution

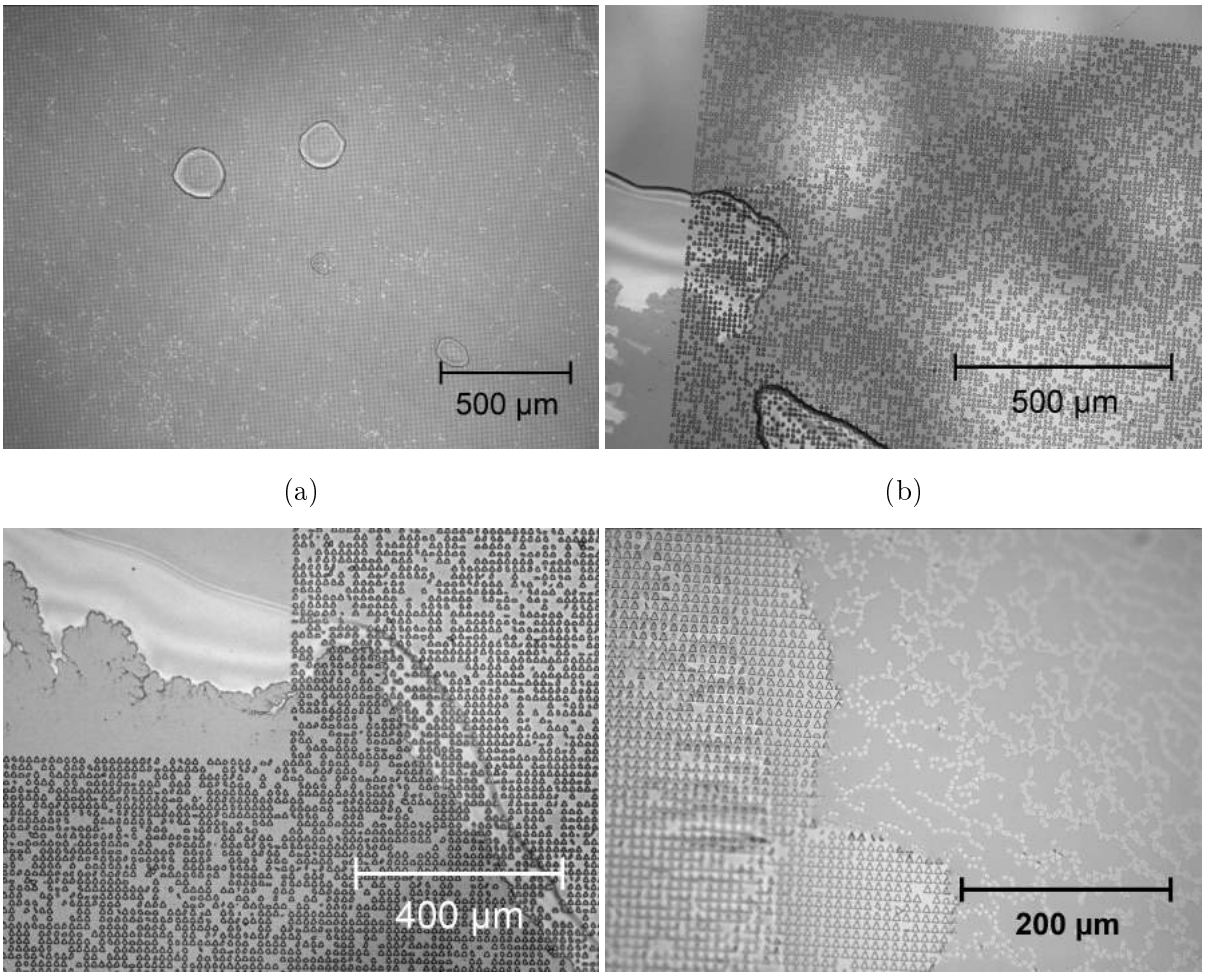

(a) (b)

(c) (d)

Figure 34: OM images of spin coated molds after UV treatment. After 60 minutes of treatment (a), spin coating yields large areas being slightly filled, as can be seen by comparing the filled, darker shaded area to the unfilled area (b). 90 minutes UV treatment further increase mold filling (c), resulting in large areas that are often connected by a RL or slightly filled (d).

using ethanol could prove beneficial.

Mixing the stock solution with water leads to inhomogeneous filling of surface areas that vary significantly in size, while about half of the mold remains either empty or covered with thick residual layer. This provides a number of filled areas well-suited for *Kaban's* research goals. Yet, the large area functionalization that this thesis aims to fabricate makes a more homogeneous filling of the mold more desirable, which is why further methods are explored.

The initial success attributed to the use of TI-Prime as an adhesion promoter fails to be reproducible, but leads to the exploration of hydrophilic mold surface treatment. Doing so by means of UV treatment results in slight a improvement of adhesion, leaving most cavities filled to low amounts. The beneficial effect depends on treatment time, and increasing the treatment to times longer than 90 minutes could further improve adhesion. This method results in a more homogeneous and reproducible adhesion improvement than the methods above. Yet, the thickness of the spin coated PMMA layer achieved with this method is smaller compared to mixing with water and is thus considered insufficient.

Treatment of the h-PDMS/s-PDMS hybrid molds with oxygen plasma shows the strongest effects compared to all methods tested. Any parameters lead to greatly enhanced adhesion, resulting in complete and homogeneous wetting of the mold. Depending on the plasma duration (5 minutes at 70 % intensity), the treatment can lead to visible cracks in the mold surface in addition to severe damage after PMMA extraction via PVA. For weaker plasma treatment (10 seconds at 40 % intensity while using a Faraday cage), the cracks are avoided, although extraction still destroys the mold surface. Consequently, while this method provides the most improvement of adhesion, it is simultaneously the least favorable as is destroys the mold.

The best results are achieved by treating molds solely out of s-PDMS with oxygen plasma. The treatment lasts at least for a weak and leaves the mold intact whilst greatly increasing wettability, making this method ideal regarding the goals of this thesis. Regarding long term stability of the mold, less aggressive hydrophilic treatments should still be explored.

An ideal treatment would be weaker than oxygen plasma but stronger than UV radiation. The strength of these treatments can be quantified by regarding the contact angle between the treated surface and water. However, the destructive nature of treatments that result in contact angles near 0° is not guaranteed, rendering all of them possible candidates. Attempting to further reduce oxygen plasma duration seems unreasonable. As argued by *Owen et al.*, the change in surface composition occurs within 1 sec. But reducing the treatment duration to less than a second comes with technical challenges, while the exact duration necessary is unknown. A possible option to test next would be UV treatment with extended exposure time, although the data obtained here suggests this will only bring limited improvement. This treatment could be intensified by the presence of oxygen/ozone, as done by *Efimenko et al.* A very promising treatment has been conducted by *Jokinen et al.*, who suggest using nitrogen plasma to obtain a contact angle to water of 60° (compared to 110° for untreated PDMS and near 0° for oxygen plasma treatment). If the above options fail, many other treatments have been

encountered in the literature, such as using plasma of argon, helium, ammonia and air [100, 106–108] or chemical treatments like piranha and KOH solution [109].

5.2.4 Optimizing Residual Layer After Successful Imprint

The previous subsections established the use of oxygen plasma treated molds for the imprint process. This can be used to fabricate shaped polymer particles if the material is extracted and added to water. As described in section 1 and thematized in sections 5.3 and 5.4, the ultimate research goal for this thesis is to release polymer particles with an EB layer system deposited on top of them. This layer system is designed to be 100 nm thick, which is more than a tenth of the particle thickness. The tensile strength of metals being much higher than that of PMMA, a negligible influence is not guaranteed. Hence, decreasing the residual layer of PMMA as much as possible is desired. During previous experiments involving oxygen treatment, an interesting observation has been made, as depicted in figure 35a. While most of the area is covered with PMMA, small areas around some cavities are empty. Achieving filled cavities with no connecting residual PMMA in between for the whole mold would be ideal. The only layer linking them together after magnetic functionalization would be the metal layer of 100 nm thickness.

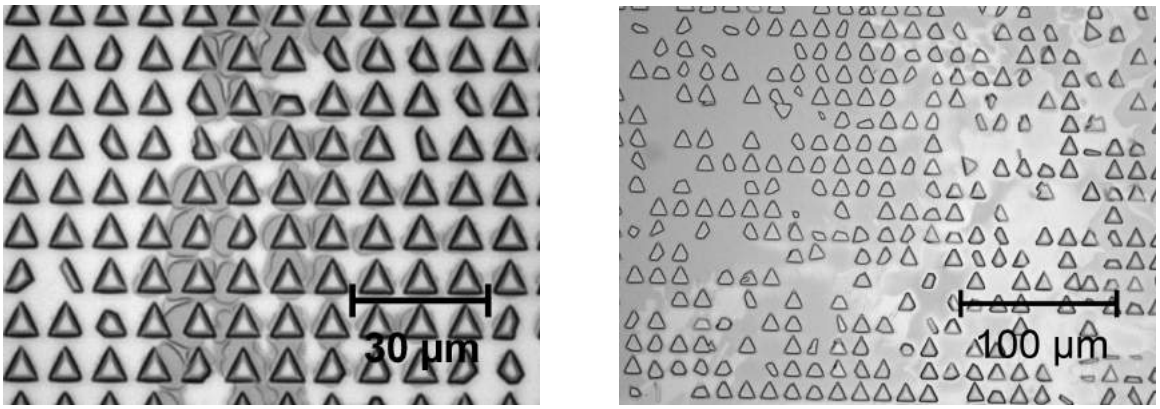

(a) (b)

Figure 35: OM images of imprinted, oxygen plasma treated molds, obtained using 4000 rpm, resulting occasionally in small areas of empty surface surrounding the cavities (a) and 10 000 rpm, resulting in less homogeneous wetting and thinner RL (b).

One attempted way to reduce the RL was by an increase of the spin coat velocity successively from 3000 rpm up to 10 000 rpm. This resulted in an increasingly more inhomogeneous PMMA distribution as portrayed in figure 35 and is hence regarded unsuccessful.

The second approach was to dilute the PMMA stock solution with its solvent as provided by the manufacturer, *AR 600-09*. Samples were then compared for 100 *wt*% stock solution, 75 *wt*%, 50 *wt*% and 25 *wt*%. If regarded under the OM, it seems that

dilution to 25 $wt\%$ still results in good filling of the structures. The SEM image shown in figure 36, however, proves that the filling level is negligible, although wetting is observed.

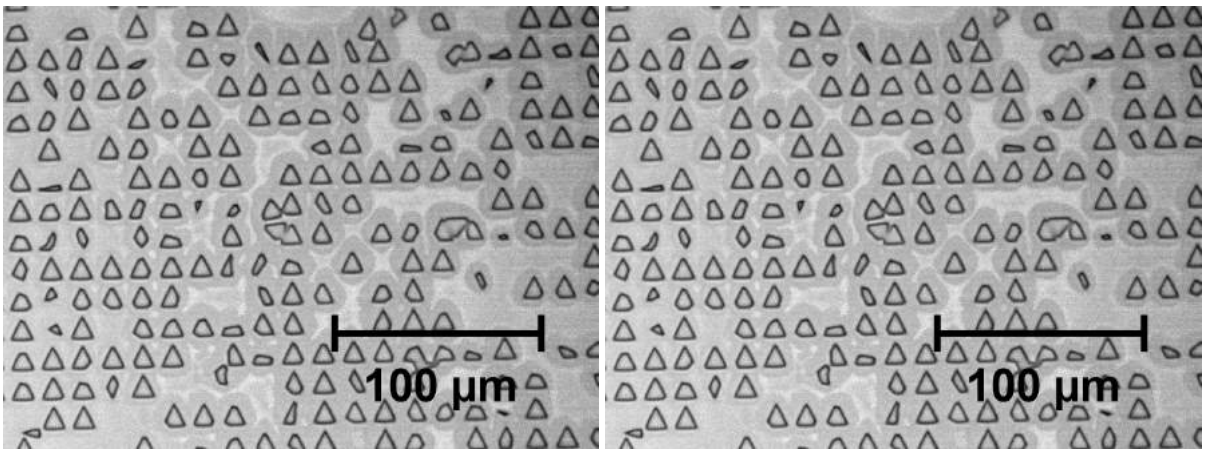

(a) (b)

Figure 36: Mold spin coated with 25 $wt\%$ PMMA stock solution diluted with more of its solvent ethyl lactate at 4000 rpm. Under the optical microscope, a homogeneous, thin RL can be seen between the cavities as lighter shaded areas (a). Investigation under the SEM reveals that the RL is too thin to even resolve an edge and that the cavities are virtually empty (b).

This emphasizes the importance of using multiple characterization methods to interpret results. More importantly, further SEM imaging demonstrates that the RL achieved without dilution is thinner than initially expected. In figure 37, an SEM image of a sample obtained using shows no dilution. The intuitive interpretation of blurriness in fact resembles soft edges that are expected to appear, as explained in subsection 3.3. At this

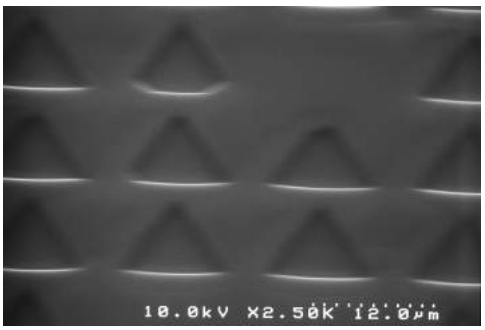

Figure 37: SEM image of a mold spin coated with undiluted PMMA stock solution after oxygen plasma treatment. Even though complete wetting is observed in the OM, the cavities are still visible.

point, quantification of the exact RL is of interest. This can be done by extracting only a part of the PMMA via PVA. This should leave a distinct edge on the mold whose

height can then be measured via AFM, for example. Due to the limited time frame of this thesis, however, this quantification remains subject of future research. In context of this thesis, it is concluded that the RL thickness is sufficiently thin to proceed to the next step of research, which will be presented in the following subsection.

5.2.5 Extraction Method Adaptation for Thin Residual Layer Samples

Extraction via PVA and tweezers as introduced in subsection 3.3 is well suited to retrieve the imprinted polymer film with the prospect of particle release in water. This was done repeatedly in subsection 5.2 to achieve complementary information about cavity filling and RL thickness. This method has the disadvantage of causing the samples to curl up, which is problematic in the context of surface functionalization by sputter deposition and several characterization methods (e. g. SEM, AFM). Thus, a different extraction method is suggested in chapter 5.1.3. It sacrifices a thin RL to simplify and combine the processes of imprinting and extraction, obtaining flat samples. This is justified if only the shaped polymer surface is of interest and no intention to release the structures as particles exists, as in the context of subsection 5.1.

For the goal of producing magnetically functionalized polymer particles, yet another set of requirements has to be considered. Here, the samples must be prevented from curling while simultaneously requiring a thin RL. This excludes both extraction methods used so far. Instead, PVA-tape extraction and other methods are explored below.

PVA-tape extraction

An easy and efficient way to obtain flat samples was found by slightly adapting the original method of *Kavre et al.* and *Ha et al.* introduced in subsection 3.3. Instead of using tweezers to peel off the hardened PVA layer, it is attached to the substrate using double-sided *tesa*® tape, as depicted in figure 38. If desired, the PVA extraction layer, which contains the imprinted polymer, can be manually separated from the double-sided tape. Of course, the problem of curling returns after separation.

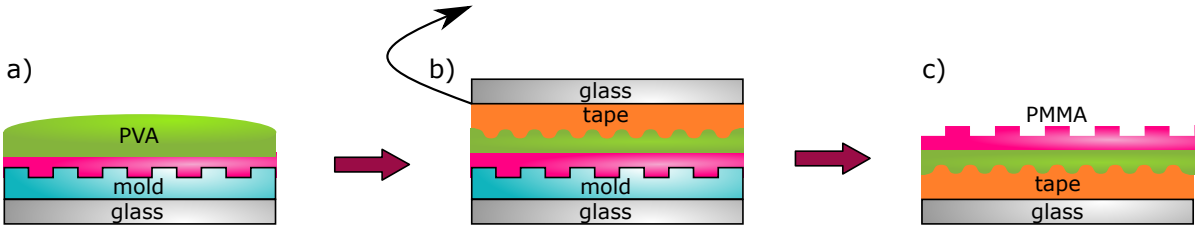

Figure 38: Schematic of the PVA-tape extraction method. The PVA extraction layer gets cast on the spin coated and cured imprint material (a). When thermally hardened it is attached to the substrate via double-sided tape (b). Removal of the substrate yields the imprinted material on a flat surface (c).

It is necessary to emphasize that the height homogeneity obtained by this method is only of macroscopic character. The roughness of the tape influences the roughness of

the sample attached to it. The extent of this influence as well as its consequences will be discussed in detail in subsection 5.4.

Other extraction methods explored

The above mentioned roughness of the sample based on the underlying tape is an undesirable property. Hence, further methods have been explored. One is found in *Kaban's* thesis and illustrated in figure 39. The method suggests partial thermal hardening of the PVA extraction layer on a glass substrate at 70 °C. After 8 minutes, the glass-PVA interface is already hardened while the intended PVA-PMMA interface remains liquid (figure 39a). Only then is the spin coated mold pressed onto the liquid PVA interface for about 1 minute, while the thermal curing finishes (figure 39b). Separation of the mold yields the imprinted PMMA on a flat PVA layer (figure 39c). The PVA remains flat because its curing on the glass substrate allows strong adhesion of the two materials.

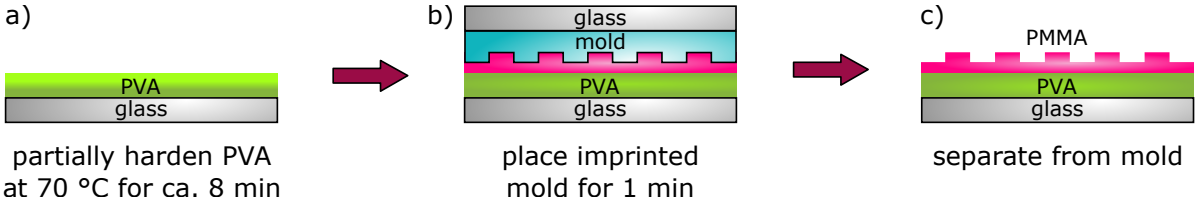

Figure 39: Schematic of an extraction method utilizing partial PVA hardening tested by *Kaban* [94]. After curing, the spin coated mold is pressend onto a partially hardened PVA film, which completes to harden in contact with the PMMA film. Upon separation, the PVA extracts the imprinted PMMA.

In this thesis, this method was found difficult to reproduce. This is due to the very short duration during which the PVA is partially hardened. As a result, most of the time the imprinted mold was either applied too early or too late. If applied too early, the PVA solution is still liquid or viscous, resulting in a failed extraction upon separation even after additional hardening time. If applied too late, there is insufficient (or zero) adhesion forming between the imprinted material and the solid PVA. Additionally, the recommended time for partial hardening of 8 minutes varies with the amount of PVA solution applied, the quantity of which is not given. These two conditions require this process to be almost constantly supervised, while the optimal timing is still difficult to achieve.

Exploring a liquid glue, a solution of Amonil® was used to glue the extraction layer to the substrate to achieve separation. It is applied on the cured extraction layer, thermally activated for 1 minute at 115 °C and cured under UV light for 1 hour. [3] Successful separation of the mold and the imprinted material could not be achieved using this method.

[3] This follows the recipe for curing Amonil®, a commercially available nanoimprint resist.

Lastly, the alternative of using liquid glue was considered. For this thesis, *Alleskleber Hart* glue from *UHU®* was available and used replacing the double-sided tape. The liquid form was hypothesized to prevent introduction of undesired surface roughness. Some tests have been initiated and documented as unsuccessful because the allowed hardening time for the glue of up to 3 hours was insufficient for the glue to completely harden. A longer duration has not been tested due the time restrictions of this thesis.

Another extraction method is used by *Fernández et al.*, extracting the PMMA without the use of PVA. This is done by pressing the spin coated mold onto the substrate while applying heat exceeding the glass transition temperature of PMMA (105 °C), causing the PMMA to transfer from the PDMS mold onto the substrate [24]. However, this method is sensitive to inhomogeneously thick RL [94]. A thick RL in some areas will hinder transfer of those areas with a thinner RL. This issue gets worsened by the concave miniscus of the PMMA filling the mold cavaties, as is schematically illustrated in figure 13 and recorded via SEM in figure 37. This method relies on the weak adhesion between imprint material and PDMS mold. It is questionable if this method will still work after the drastic increase of adhesion through plasma treatment of the mold. It is furthermore questionable if the transferred structures can still be released as particles, as is ultimately intended for this research project.

Perhaps these downsides can be overcome by utilizing a combination of the methods from *Ha et al.* and *Fernández et al.*. The results of this thesis show that PMMA adheres stronger to PVA than to PDMS, plasma treated as well as untreated. The hardened drop cast of the PVA extraction layer smooths the surface. In the suggested approach, the sample substrate (silicon or glass) would be brought in contact with the PVA foil and heated above the glass transition temperature of PMMA (105 °C) and PVA (85 °C) [110]. Separation should then, in theory, yield the empty mold and the substrate with the imprinted polymer. Preceding plasma treatment of the substrate could further improve its adhesion to the PVA foil. This approach, however, was not tested in this thesis due to a lack of time.

In summary, the method of PVA-tape extraction is the only method found to be reproducible and successful in flat extraction of thin RL samples at this stage of the thesis.

5.3 Magnetically Functionalizing Structured Polymer Surfaces

Before it was attempted to magnetically functionalize polymeric structures that can be released as particles, preliminary experiments were performed to learn about the sensitivity of this process regarding the substrate material and morphology, as well as the EBLS. The composition and deposition parameters of the EBLS mostly remained fixed during this thesis. Section 3.4 provides reasoning for the selection of these parameters. The first part of this section investigates the suitability of involved materials for EBLS deposition. The second part applies this magnetic functionalization to shaped polymer surfaces produced using the methods described in 5.1. Together, they provide comparable data sets for the findings of chapter 5.4.

5.3.1 Suitability of Involved Materials for EBLS Deposition

Because of the high number of factors influencing the properties of an EBLS, some of which are explained in sections 2.2.3, these properties are impossible to predict and can vary greatly between two systems showing seemingly minimal differences. Accordingly, the first experiments performed give an overview over the sensitivity of the chosen EBLS regarding the substrate used to produce it, and provide a reference point for future experiments. All materials were positioned on silicon substrates manually cut to a 1 cm^2 size. An EBLS was then deposited on them, consisting of Cu(50 nm)/IrMn(30 nm)/CoFe(10 nm)/Si(10 nm), as detailed in section 3.4). The first substrate material tested was PMMA. Confirming a suitable interplay of this material with the chosen EBLS parameters is a crucial precursor to using more complex samples fabricated according to section 5.1 and 5.2. After successful measuring of an EB effect for six samples, two samples of each of the other materials used for polymer sample fabrication were tested as EBLS substrate as well. The samples were measured using a VSM and the EB fields obtained from the respective hysteresis curves.

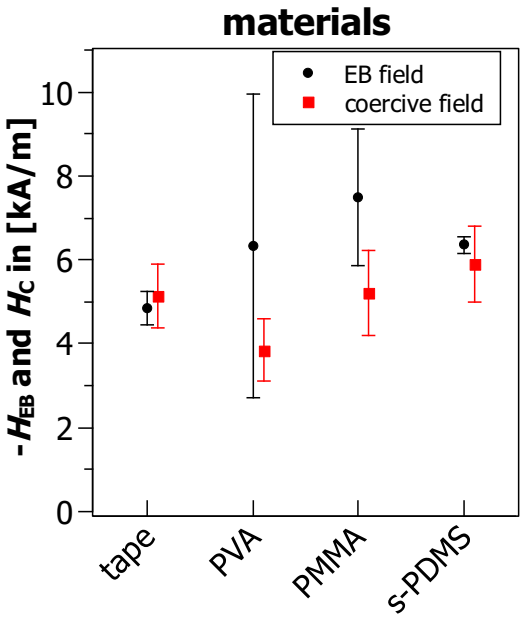

Figure 40: $-H_{EB}$ (black circles) and H_C (red squares) resulting from EBLS deposition on different materials, determined using a VSM. Each data point represents the average of two samples, which causes the large error bars.

The results are summarized in figure 40, where each data point represents the average value for each material. The graph shows absolute values for better visualization. The amount of two samples per material does not allow statistical interpretation and is responsible for the large error bars. It is, however, evident that the strength of the EB and coercive fields varies between different conditions. When regarding all values, it can be observed that H_{EB} varies greatly between 3 kA/m and 10 kA/m, while H_{C} seems less

sensitive, lying between 3 kA/m and 7 kA/m, roughly. While an EB field depends on the interplay of F and AF, coercivity is a ferromagnetic phenomenon (see 2.2.3) and exists independent of the AF/F interface, although it can be enhanced by it. It can be concluded that no material is entirely unsuited for EB experiments, although their surface properties show a strong influence on the observed EB effect, where the EB field reacts more sensitive to the substrate material than the coercive field. It can further be concluded that the coercivity for substrates of structured polymer layer systems is likely to be in a similar range as observed here.

It is interesting that an EB field of around 6 kA/m can be measured for PDMS. In his master thesis, *Siebert* tested the suitability of flexible materials to serve as EBLS substrates. He deposited an EBLS made up of Si/Co/IrMn/Au[4] with layer thicknesses of 20/15/30/5 nm, respectively, on s-PDMS[5], and measured hysteresis using an L-MOKE. Interestingly, he measured no EB field on PDMS. It cannot be concluded at this point whether his findings contradict those of this thesis or if instead the difference is simply due to the different EBLS used. *Siebert* tested only one PDMS sample, while this thesis tests two. Determining this would require a more extensive test series, measuring e. g. ten samples with s-PDMS as substrate for each layer system.

5.3.2 Results of EBLS Deposition on a Structured PMMA Surface

Subsection 5.3.1 established PMMA as suitable material for EBLS deposition, while subsection 5.1 established a process to obtain a structured PMMA surface on a silicon substrate using RNIL. In this part of the thesis, the silicon substrate-based samples are equipped with the same EBLS as the materials in the chapter above. This is the third step in the process of obtaining free micrometer shaped, exchange biased polymer particles. Accordingly, the goal of this step is a proof-of-concept to measure an EB field on micrometer-shaped, unreleasable polymer structures. The respective measurements have been accomplished using VSM and L-MOKE.

Regarding the L-MOKE measurements, each curve is recorded from 250 measurements per point and averaged over 20 hysteresis cycles. Each sample was measured on three spots within a structured field and three spots outside of a structured field. This was performed for three samples.

Comparing the EB fields measured inside and outside of the structured fields revealed that each sample shows a slightly more negative EB field inside the structured area, with an average of $\Delta H_{\mathrm{EB}} = 0.60 \pm 0.23\,\mathrm{kA/m}$. This slight increase could be due to two factors. The first could be position-dependent deposition rates during the sputter deposition process, which have been repeatedly observed by the work group. The structured field of the sample has an edge length of 5 mm, compared to 10 mm of the substrate. This difference might be enough to observe the position dependency. The other factor could be interference. As shown in section 5.1.1, the periodically structured area of the sample generates a diffraction pattern when reflecting the laser beam. The

[4] The reverse order of antiferromagnet and ferromagnet is known as bottom-up sputtering.

[5] *Siebert* uses the same recipe and ingredients as was used in this thesis for s-PDMS, although he simply terms it PDMS.

measured laser beam then only shows a part of the sample, losing some information. In this case, measurements with a Bragg-MOKE would provide more insight, as they include information from different orders (see 5.1.1).

When regarding the average of all measurements, the EB field is found to be $H_{\mathrm{EB}} = -9.9 \pm 2.0\mathrm{kA/m}$ and the coercivity $H_{\mathrm{C}} = 4.5 \pm 1.4\mathrm{kA/m}$. This corresponds well to what is expected based on the data obtained in section 5.3.1. Consequently, structured PMMA samples prepared according to section 5.2 can be expected to show similar values. It can also be concluded that the presence of the structures does not propose hindrance to a measurable functionalization through an EBLS.

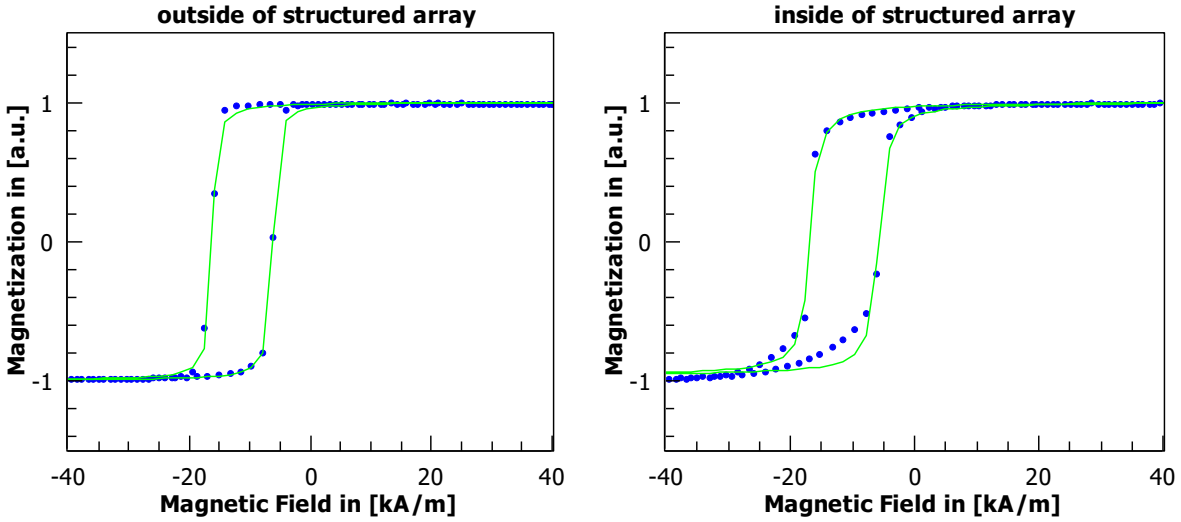

Figure 41: Magnetization curves recorded via L-MOKE for a measurement outside the structured array (left) and inside of it (right). The external magnetic field is applied parallel to the easy axis. The corresponding fit function is added in green.

An interesting observation can be made when comparing two hysteresis curves of outside and inside a structured field, as displayed in figure 41, left and right, respectively. The hysteresis recorded inside the structured array shows a more shallow slope $\mathrm{d}M/\mathrm{d}H$ during magnetization reversal than the one recorded outside of it. This indicates a more step-by-step reversal of the magnetic domains instead of reversing all at once. The reason for this is the difference in size and shape of the measured material, in turn causing a difference in shape anisotropy and magnetic properties. The outside area can be modeled as extended planar film. The accompanying in-plane magnetization decreases the stray field energy, which the system aims to minimize. Within the structured field, this in-plane magnetization is disrupted at the structure edges. This changes its orientation to the sample surface from parallel to perpendicular, as illustrated in figure 42. As a result, the affected domains begin to reverse earlier due to the saturated magnetization state not corresponding to their minimized stray field energy. The slope is further influenced by the presence of 'damaged' structures that have their origin in the MT (see section 3.1), resulting in even more diversity in domain sizes and shapes.

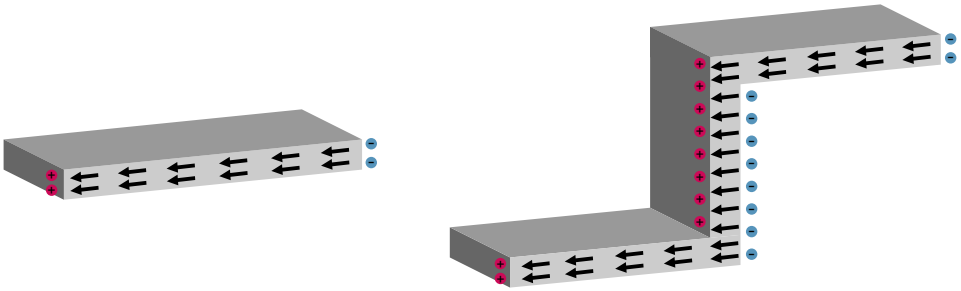

Figure 42: Schematic cross sections of a saturated planar thin film and a saturated structure wall. The different amount of net magnetic charges at the object's edges cause a different stray field energy contribution at the saturated magnetization state.

5.4 Magnetically Functionalizing Shaped Polymer Particles

While section 5.3 addresses the underlying mechanisms of the EBLS tested on unpatterned and patterned polymer films with a thick residual layer, this section examines sputter deposition on near residual layer-free patterned polymer films, which are produced as shown in section 5.2 and which are able to be released as particles when added to water. This section utilizes the data gathered from sections 5.2 and 5.3 to investigate the magnetic functionalization of the patterned polymer film.

5.4.1 Sputter Deposition on Releasable Polymer Structures

This section builds on the results obtained from the preceding sections. Section 5.2 established a reliable way to produce shaped polymer particles that can be released in water, and section 5.3 provided evidence for the practicability of their exchange bias functionalization based on experiments with the samples obtained in section subsec:RNIL.surface.

This part of the research aims to combine the previously applied methods to fabricate shaped, EB functionalized polymer structures that can be released as particles in water. To do so, the polymer material was shaped via RNIL, extracted via PVA-tweezer or PVA-tape method (see 3.3 and 5.2.5) and functionalized via sputter deposition (3.4). This was done initially for a total of seven samples, representing two samples for each field of the 4-field master template except the one with 5 µm sized structures. This was later complemented by two more PVA-tape extracted samples (12.5 and 5 nm structures).

All nine samples were magnetically characterized via VSM, resulting in an unexpected finding for the magnetic properties. The EB field and coercive field were determined as $H_{\mathrm{EB}} = (-0.01 \pm 0.07)\,\mathrm{kA/m}$ and $H_{\mathrm{C}} = 4.4 \pm 0.5\,\mathrm{kA/m}$. In other words, the EB field was measured to be virtually non-existent. It would have been unsurprising to encounter a reduced effect. Its sensitivity regarding the deposition substrate material became evident in section 5.3.1. Its complete absence, however, is unexpected. A characteristic VSM hysteresis curve recorded with the external magnetic field parallel and perpendicular to the samples easy axis is shown in figure 43.

It can be observed that the hysteresis shows the same shape for perpendicular orientations of the easy axis. It is, therefore, evident that the lack of a measurable EB field

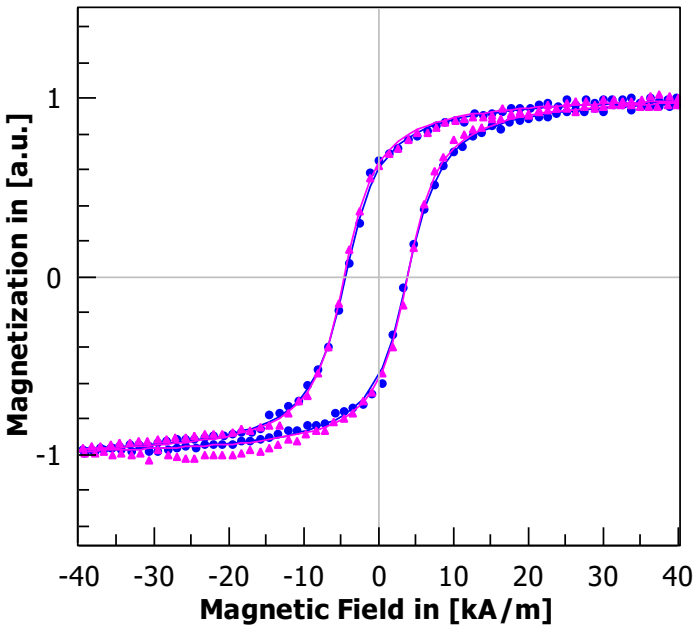

Figure 43: VSM hysteresis curves of PVA-tweezer extracted structured polymer after EBLS deposition with the easy axis parallel (blue circles) and perpendicular (magenta triangles) to the external magnetic field. The fit functions have been added as a guide-to-the-eye. The two curves are almost identical.

does not cause the observed system to behave completely ferromagnetic, as the hysteresis should disappear in this case (based on *Stoner-Wohlfarth* model [**Radu.2007**]).

5.4.2 Investigating the Lack of EB - Particle Fabrication Process

The samples discussed above were prepared with identical parameters for EBLS deposition with respect to the samples presented in section 5.3.1. Therefore, it is evident that the significant difference in measurable EB field does not originate in the deposition parameters, which in general are proven to have a major influence on the resulting EB field strength. The obvious difference in sample fabrication lies before this step and represents the varying methods between sections 5.1 and 5.2. However, it is not obvious which difference in sample fabrication causes the observed lack of an EB field, as there are multiple candidates. Their interplay during the structuring process further complicates logical analyzation of possible origins. In short, these differences are: structuring, mold treatment, extraction method, and PMMA thickness. The surface material is another influential factor but was determined not to be a cause in section 5.3.1.

First, an explanation for how these factors could influence the EBLS growth is given. After this, it is explained how the corresponding hypotheses were tested, before the results of these tests are presented.

At first glance, polymer structuring does not seem to be a factor in the lack of an EB field because of the positive findings of section 5.3.1. However, the absence of an EB field was only observed for structured samples. Given the macroscopic influence the structures

have on the surface morphology, it is possible that this property in combination with other influences could cause the lack of a measurable EB field.

Any process that changes the surface properties of the mold the EBLS is deposited on has a strong influence on its growth. This hypothesis is supported by the findings of 5.3.1. It is possible that the PMMA surface gets modified when in contact with the oxygen plasma treated PDMS. The increased adhesion between the two materials combined with weakened structural integrity of the exposed PDMS have been observed to cause the latter to be ripped out of the mold. While this effect was visible to the naked eye for hybrid molds with h-PDMS at the surface, it is possible the same phenomenon can occur for the s-PDMS molds to a lesser extent, extracting only several nanometers or even just a monolayer of s-PDMS upon separation. If this were the case, the surface would be modified on the molecular level and could influence the growth of the buffer material of the EBLS.

The extraction method may also be a cause. Although it has no direct contact to the polymer surface, extraction of the PVA layer via tweezers or tape influences the morphology of the whole sample. In section 5.3.1, double-sided tape is used as substrate for EBLS deposition, resulting in EB fields around 5 kA/m. Therefore, it seems counterintuitive that an EB field can be measured when the EBLS is deposited on tape and PMMA, but not on tape, PMMA and PVA.

Finally, PMMA thickness was tested as a potential cause. Regarding the EBLS, the thickness of every layer has been found to be influential on the EB effect, including that of the diamagnetic buffer layer. It is possible that the PMMA thickness or the corresponding application methods (e.g. spin coat or drop cast) somehow influence the interface between PMMA and buffer layer.

Generally, when the influence of a certain property is tested, all other properties are held constant. This is not easily achieved due to the dependence of some factors on others. For example, spin coating PMMA on the mold requires prior plasma treatment (5.2), while extraction through hardening on silicon (5.1.3) fails using spin coated PMMA. To be able to vary only one factor while maintaining the others, a new combination would have to be employed: a drop cast of PMMA onto a plasma treated mold that is either structured or unstructured, which is extracted after RNIL via PVA-tape method. Using this method, the four factors could then be varied independently. However, this would require a high number of new samples. Consequently, a different approach was chosen to utilize the data acquired thus far. This approach compares, for example, all of those samples that involved mold treatment to those that did not involve mold treatment. The argumentation of this approach is opposite to the first: whereas the first method would investigate each factor individually, this method holds one factor constant while varying the others. While this method seems more time-intensive, it required minimal experimental effort. Following this approach, all samples that share the critical factor will fail to show a measurable EB field, regardless of what else has been changed. Accordingly, the samples already characterized were sorted into the four respective categories. The the missing data points were then acquired, leading to the four graphs displayed in figure 44.

In figures 44 a-c, no clear distinction of samples with or without EB field can be made.

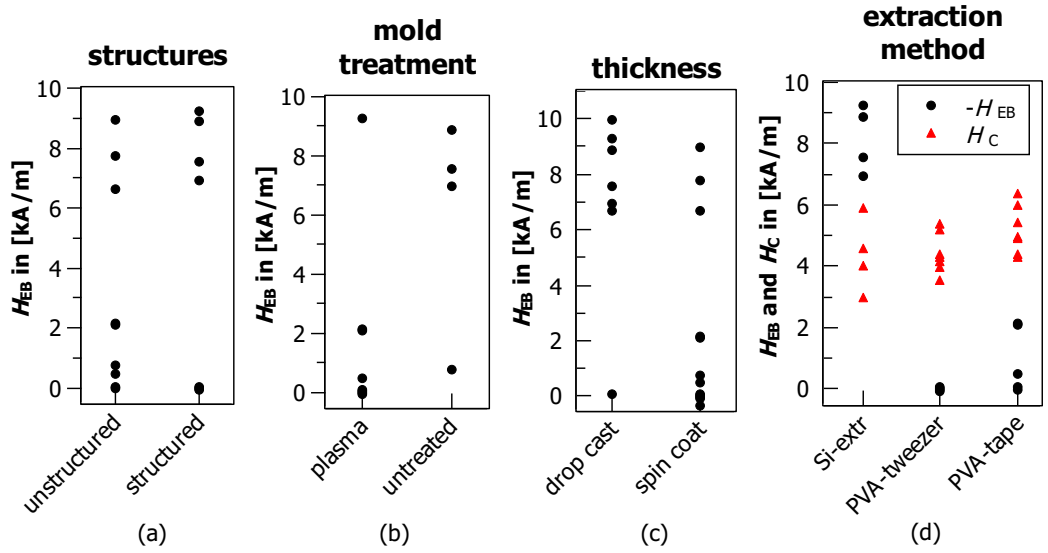

Figure 44: Comparison of the samples' EB fields when sorted into the four categories: structuring (a), mold treatment (b), PMMA thickness (c), and extraction method (d). A clear dependency of the samples' EB field can only be seen for the extraction method. The respective graph (d) also contains the coercive fields (red triangles), which show no dependence on EB field or extraction method.

Only the extraction method (d) clearly influences the outcome. It can, therefore, be concluded that the two extraction methods using PVA are the cause of the lack of an EB field. In addition to this, several other interesting observations can be made by evaluating the data. Firstly, the EB field is between 6 and 11 kA/m for the samples that show an EB field, which fits into the data range obtained in 5.3. Despite identical preparation of the four Si-extracted samples, their measured EB fields vary up to $\Delta H_{\mathrm{EB}} = 2.3\,\mathrm{kA/m}$, representing a difference of 25 %. As this data is acquired via VSM, the difference can be caused by the diamagnetic PMMA of the sample, which can vary in volume due to the preparation method. A more exact analysis of these samples via L-MOKE is discussed in section 5.3.2. Interestingly, two measurements regarding PVA-extraction show values of around 2 kA/m. This represents a significant difference from zero, which is unlikely to be caused from the measurement setup. If and how these samples differ in their properties from the other samples that were produced identically is investigated in the next subsection. Figure 44d also depicts the coercive fields of the samples. They are distributed around $H_{\mathrm{C}} = (4.5 \pm 1.5)\,\mathrm{kA/m}$ and show no correlation with any of the investigated categories or their corresponding EB fields. Hence, only the conformity of their range with previous experiments can be concluded. An increased coercive field, which can be expected to accompany an EB field (see 2.2.3), is not observed.

The evidence presented above pinpoints the extraction process as the responsible factor for the observed lack of a measurable EB field. It can be argued that the macroscopic roughness of the double-sided tape influences the morphology of the PMMA

surface. Since an EB field can be detected very well if the EBLS is grown on a pure tape substrate, these findings are somewhat counter intuitive. Generally speaking, understanding why some approaches fail to show the intended result is often of great scientific importance. The knowledge gained from undesired results can allow understanding and prediction of alternative approaches and lead to directions for the most promising path to success - and in rare cases even lead to groundbreaking discoveries, like the discovery of penicillin [111]. Accordingly, understanding why no EB field was measured here was at this point prioritized over testing further extraction methods.

5.4.3 Investigating the Lack of EB - Surface Roughness and Grain Size Distribution

In order to analyze the the differences between the samples with and without a measurable EB field, the samples were categorized into four categories related to their expected surface roughness: (A) smooth silicon extracted samples, which show EB fields between 6 and 10 kA/m after sputter deposition; (B) a collection of PVA-tape extracted samples that do show a relatively weak EB field of around 2 kA/m; (C) PVA-tape extracted samples, which show no measurable EB field after sputter deposition; and (D) samples using tape as a substrate for EBLS growth, which show the highest macroscopic roughness and EB fields between 4 and 6 kA/m. Each category of samples was investigated via AFM regarding their surface roughness and grain size distribution. These properties were then compared to the EB field that the samples show to find a possible correlation.

The investigation was performed for the top layer (Si) of the EBLS. It must be emphasized that the properties of interest are those of the AF/F interface, as this is the area where the EB effect arises. Characterizing the surface of the capping layer, instead of the specific interface, was performed for multiple reasons. The AF/F interface is embedded in between the two materials and cannot be accessed easily. Common methods used to characterize the AF and its interface to the F, like X-ray reflectometry, were not readily available within this work group and at the time of these investigations.

It can now be argued that the next best surface to be analyzed would be the AF surface without added F and buffer layers. But due to the rapid oxidation of the AF layer, this approach does not represent an easy task. Ideally, each sample would be characterized immediately after its deposition process, slowing down the overall progress. At the same time, oxidation as well as other contamination of the AF surface when exposed to air does not allow for the same samples to be used for AFM characterization and reused for magnetic characterization after deposition of the complete EBLS. This further increases the number of required samples. On the other hand, it is possible that the morphology of the silicon capping layer directly relates to that of the AF/F interface and even to the underlying Cu buffer layer. Multiple sources have reported that the surface morphology of films deposited on Cu is conformal during film growth and that AFM measurements reflect the initial growth of Cu on Si(100) substrates [52, 112, 113].

Under the premises that a) this also applies to PMMA substrates, b) the CoFe layer is thin enough to follow the growth of the IrMn layer and c) the deposited Si layer on top of the EBLS is amorphous, it is possible to assume that the measured roughness

directly relates to that of the AF layer. The roughness then scales proportionally to the thickness of material in between [114]. It is also possible that those parameters relate to those of the underlying Cu buffer layer, but in the context of discussing the EB effect, this layer is not of interest.

Considering the sensitivity of an AF layer to oxidation and other contamination, it seems more reasonable to utilize the less sensitive samples which are already available. By doing so, the samples can be discussed in relation to one another, although the findings cannot be compared to literature. The measured property (e.g. roughness and grain size distribution) will be compared to the EB effect a sample shows.

Based on these considerations, the samples of the four categories were investigated via AFM, scanning three points of each sample to minimize the influence of any location-dependent variations in surface property. The first property that is discussed is the grain size distribution, which could not be measured for the samples using tape as substrate, as shown in figure 45. According to literature, the grain size distribution follows a

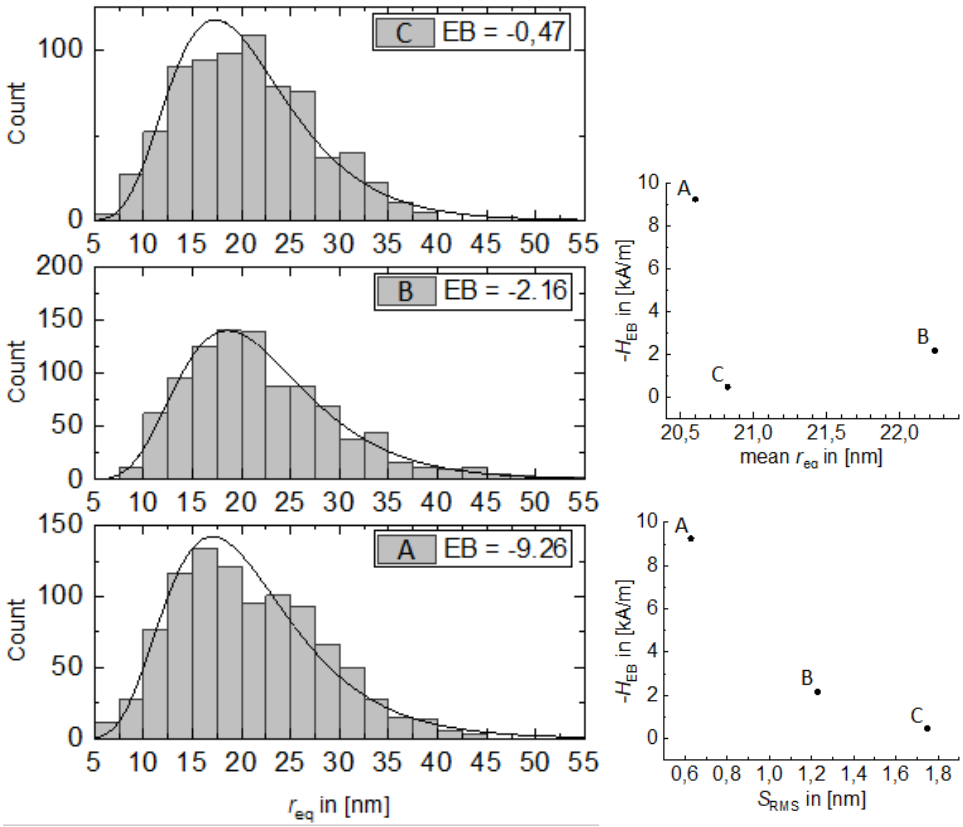

Figure 45: Left: Grain size distribution of the three samples. No significant difference can be seen comparing the silicon-extracted (A) and the two PVA-tape extracted (B and C) samples. Right: H_{EB} plotted against the respective sample's mean equivalent radius r_{eq} (top) and against its surface roughness S_{RMS} (bottom). The latter shows an inverse relation, while no relation can be identified for the former.

logarithmic normal distribution. The probability density $p(r_{eq})$ for a grain to have a

radius r_{eq} is given by

$$p(r_{eq}, \mu, \sigma) = \frac{1}{\sqrt{2\pi}\sigma r_{eq}} \exp\left(-\frac{(\ln r_{eq} - \mu)^2}{2\sigma^2}\right) \tag{15}$$

with the determining parameters σ and μ [60, 115]. The mean value $E(r_{eq})$ and the variance $\mathrm{Var}(r_{eq})$ are given by

$$\mathrm{E}(r_{eq}) = \exp\left(\mu + \frac{\sigma^2}{2}\right) \tag{16}$$

$$\mathrm{Var}(r_{eq}) = \exp\left(2\mu + \sigma^2\right)\left(\exp\left(\sigma^2\right) - 1\right). \tag{17}$$

The logarithmic normal distribution can also be seen for the data displayed in Equation 15 (left), which shows the GSD as histograms for the samples. Continuing to build on the assumption that the measured grains relate to the AF grains, one would expect a significant difference in grain sizes for the large differences observed in EB fields. But comparing the three histograms shows virtually no difference. The data can be used to fit a log normal distribution using Equation 15. Utilizing the fit, the parameters σ and μ of the distribution can be extracted to calculate the mean grain size $\mathrm{E}(r_{eq})$ using Equation 16 and the variance using Equation 17. Plotting the corresponding EB fields against this data results in the graph shown in figure 45 (top right). It can be observed that the mean grain size $\mathrm{E}(r_{eq})$ shows very little change for the three samples. As the difference in grain size distribution is insignificant, this property cannot be the cause of the significantly different EB field. This finding corresponds well to the results one would expect when using identical deposition parameters.

Imaging via AFM was done for areas of 10 µm edge length, recording 256 pixels per line for 256 lines. From this, the resolution can be calculated as 39.06 nm/px. With a resolution of 39 nm for the AFM measurement, the roughness measured for a 10 µm range does not resolve the morphology of individual grains, which have a mean size of about 20 nm (see figure 45 top right). Accordingly, the data in figure 45 (bottom right) contains information about the heights of grain areas compared to each other. It shows an inverse dependence of the EB field to the roughness. The high EB field corresponds to a comparatively low roughness and, thus, excellent coupling between AF and F grains (figure 46a), while increasing roughness disturbs the uniform exchange interaction, resulting in a decrease of EB field (figure 46b). This interpretation builds on the model of *Fulcomer* and *Charap*, who introduced a roughness parameter to correlate the EB strength with the amount of coupling domains per area (see 2.2.3) [65]. According to this model, the EB field is approximately proportional to the sum of the contributing grains' surfaces multiplied with their respective coupling constant (compare equations 10 and eq:2-grain.free.energy2). A high number of frustrated bonds hence causes poor coupling of the F to the AF, reducing the EB effect.

The AFM measurements of the sample using double-sided tape as substrate show seemingly contradicting results. While evaluation of the grain size distribution was not possible for this sample, the measured roughness had a value of about 62 nm. This value

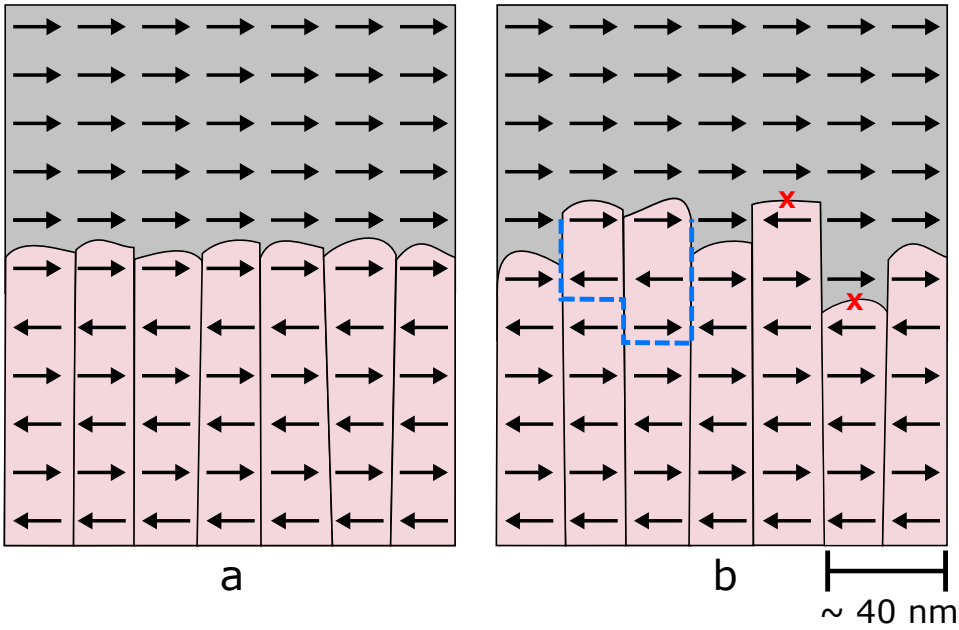

Figure 46: a) Illustration of the AF/F interface for Si-extracted samples with a macroscopic area of interface magnetization which enables interface coupling and, therefore, the formation of a unidirectional anisotropy. For the PVA extracted samples (b), these areas are either disrupted or significantly smaller due to frustrated bonds of a comparatively high number of grains, preventing effective coupling of the F to the AF. Illustration of the AF/F interface compared for Si-extracted samples (a) and PVA-extracted samples with an increased surface roughness (b). The increased roughness reduces the EB effect by introducing frustrated bonds (marked by a red x) and domain walls in the AF (blue dashed line).

is significantly higher compared to the other samples, while it still shows an EB field of $H_{\mathrm{EB}} = -5.2\,\mathrm{kA/m}$ and a coercivity of $H_{\mathrm{C}} = 5.88\,\mathrm{kA/m}$. One possible explanation for this result stems from the work of *Liu et al.*, who found the dependence of the measured EB field on the interface roughness to vary significantly for different substrates [112]. While there was a strong correlation for samples with a Cu underlayer grown on Si substrates, they found the EB effect to be insensitive to a change of roughness for samples deposited on Si substrates. Changing the substrate used here from PMMA to tape could have a similar effect, rendering the data incomparable.

Another explanation lies in the way of data acquisition and the definition of the measured roughness itself, which becomes evident when smaller areas are regarded. Figure 47 shows a falsely-colored AFM image of a tape substrate sample after line correction using the line median. Significant height differences can be seen when comparing large areas. However, for this sample, the roughness depends tremendously on the kind of data correction applied and the area measured. Subtracting the background using a polynomial filter with a polynomial degree of 5 (figure 47a), instead of using the line median for line correction, as done for the other samples (figure 47b), yields much smaller roughness values, as does measuring over a much smaller area of 1 µm (figure 47c). In both cases, the measured RMS values lie in the range of $(6.0 \pm 0.9)\,\mathrm{nm}$, representing roughly 10 % of the original values. It is possible that the roughness is even smaller for an area that includes only several grains.

Considering the above arguments, it is plausible that small areas of less than $1\,\mu\mathrm{m}^2$ locally show successful coupling between AF and F grains, while being separated from other areas due to the high macroscopic roughness, resulting in the observed EB fields of around $H_{\mathrm{EB}} \approx 5\,\mathrm{kA/m}$.

It can be said that using tape as substrate comes with such different conditions that this category cannot be compared to the PMMA samples, which is why this data point is not included in figure 45.

Regarding the experiments above, it can be concluded that the change of EB effect for different sample preparation methods, specifically PMMA extraction methods, finds its origin in the interface roughness. While the grain size distribution is insensitive to the different preparation methods, the resulting difference in roughness influences the exchange interaction at the AF/F interface to differing extents, causing variances in the EB fields. PVA-tweezer as well as PVA-tape extraction hereby cause an increased roughness, which correlates to a decrease in EB field. This finding further increases interest in the alternative extraction method hypothesized in section 5.2.5. This extraction, in theory, not only represents a rigid extraction, which comes with a lower surface roughness. The heating to a temperature exceeding the glass transition temperature of PMMA could also smooth the patterned surface. It can therefore be regarded as a promising approach that should be strongly considered in future research of this topic.

It must be mentioned, however, that the above interpretations rest on the assumption that the measured morphology directly relates to the AF/F interface. It is possible that the morphology observed instead relates to the top of the ferromagnetic CoFe layer, rather than the AF/F interface. In this case, the data allows no conclusions about the interface. Consequently, the observed grain size distributions, belonging to the CoFe/Si

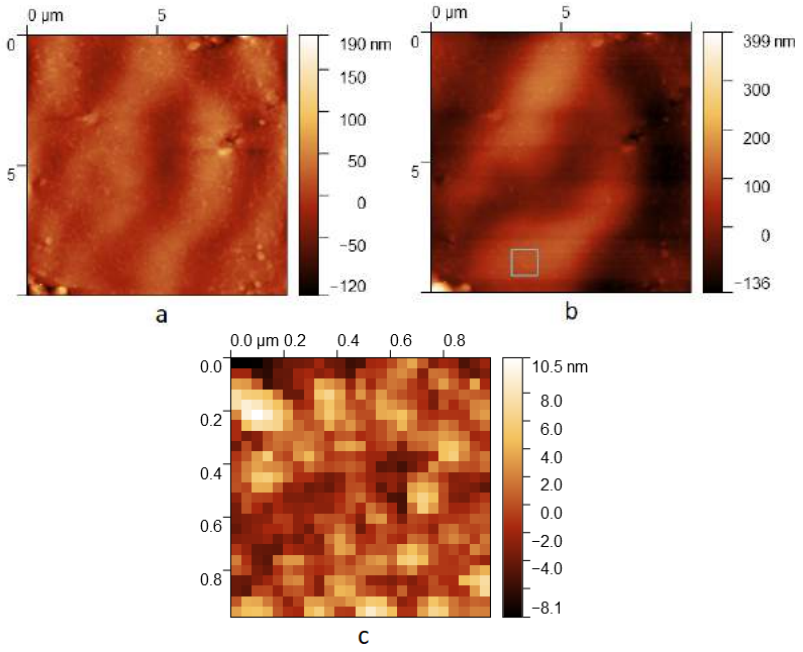

Figure 47: AFM images of a sample using tape as substrate. Using *Gwyddion* to determine the RMS roughness yields very different results depending on the way it is measured. Row alignment using a polynomial function with factor 5 (a) gives values in the range of 10 % of those obtained using the line median (b), as does measuring of selected 1 µm^2 sized areas (c).

interface, show no correlation to the measured EB fields, simply because there is no correlation. The trend regarding the surface roughness (figure 45 bottom right) would then be coincidental.

Answering this question, however, is not trivial. As mentioned above, the correlation between the morphology of underlying layers and of the top layer has been shown for systems grown on Si substrates with and without a Cu buffer layer of varying thickness [112, 113], but not for the system employed here, which uses a PMMA substrate and different materials for the AF and F layers. The respective investigation could be performed similarly to the approach of *Liu et al.* by measuring the surface morphology before and after film deposition. This was attempted in this thesis. Using PMMA as substrate, however, complicates this approach due to a poor interplay of substrate and cantilever tip rigidness. As a consequence, the measurements did not provide usable information. One way to solve this issue could be the use of a more suitable, softer cantilever tip. Another solution could be the deposition of a very thin layer of amorphous material, e.g. silicon, on top of the PMMA layer to turn it 'accessible' with minimal influence on the surface morphology. As this approach still influences the surface energy and in turn the whole EBLS growth, changing the cantilever material might be more advantageous.

6 Summary and Outlook

The main objectives of this thesis were to establish the reversal nanoimprint lithography technique for the production of residual layer-free, anisotropic structures, and to investigate the compatibility of this technique with succeeding magnetic surface functionalization via sputter deposition. The groundwork laid by this thesis should enable expansion of the research involving micro- and nanopatterning via RNIL by establishing reliable methods transferable to other shapes and materials. It should further pave the way for experiments involving exchange biased patterned polymer films and particles. This thesis investigated how easily sputter deposition of a metallic thin film containing an exchange bias layer system can be applied to a patterned polymer surface, and how the sample properties influence the resulting EB effect.

In the first part of research, the preparatory steps involved in the RNIL process were adapted to optimize efficiency of the experiments. At first, utilizing the molding methods described in literature yielded non-trivial issues. Without further precautions, transferring the pattern from the master template to the PDMS mold was found to occasionally lead to unsatisfactory molding results and high risks of damaging the master template. To ensure safe and efficient molding, the the MT was glued to the underlying ground - here, an aluminum plate - using a drop of aqueous PVA solution on each MT corner. After thermal curing of PVA, this prevents suction of the MT during PDMS application. In turn this prevents tilted molds and, more importantly, prevents the viscous PDMS mixture from flowing under the MT before its hardening by polymerization, which endangers safe MT retrieval. The gluing PVA can be safely removed using water. If desired, baking paper can be used to enable easy separation of excess PDMS also from under the MT, although this does not prevent mold tilting.

To prepare for the tests examining the compatibility of RNIL produced patterns and sputter deposited exchange bias thin films, a varied RNIL technique was used to produce a patterned polymer film with a thick RL, which is not harmful regarding this application. A PMMA solution of low viscosity was drop cast onto an untreated PDMS mold and hardened for 15 minutes at 115 °C while in contact with the silicon sample substrate. Peeling off the substrate with the attached polymer film was termed silicon extraction to contrast other extraction methods tested in this thesis. A good copy of the original MT structures with a sub-micrometer resolution was verified via SEM and OM.

Onto these patterned samples with a thick RL, an exchange bias layer system of Cu(50 nm)/IrMn(30 nm)/CoFe(10 nm)/Si(10 nm) was deposited using sputter deposition. The samples were then magnetically characterized using Kerr magnetometry, finding an EB field of $H_{\mathrm{EB}} = -9.9 \pm 2.0\,\mathrm{kA/m}$ and a coercive field of $H_{\mathrm{C}} = 4.5pm1.4\,\mathrm{kA/m}$, confirming the compatibility of an EBLS with a patterned polymer.

To serve as reference and gain an understanding of the general interaction of the magnetic thin film on various involved materials, unpatterned PMMA films as well as PDMS, PVA and double-sided tape were cast onto a silicon substrate and similarly equipped with an EB layer system. The averaged EB fields of the respective materials varied roughly between 5 and 7 kA/m, while the coercive fields varied between 4 and 6 kA/m.

The number of two samples for each material does not allow for statistical certainty of these values. Still, the general practicability of magnetic surface functionalization via sputter deposition of PMMA as well as the other materials is demonstrated.

Applying polymer photo resists onto metal substrates via spin coating is a well established process. Many resists are available for purchase from suppliers like *allresist GmbH* or *MicroChemicals GmbH*. Applying these materials onto molds of PDMS, however, follows different rules and is thus not always easily achievable. In this thesis, PMMA solutions in a variety of solvents and solvent mixtures have been tested for wetting of a surface patterned PDMS mold. While a variety of available PMMA stock solutions have been tested in preliminary work, this thesis continued these tests by mixing the most promising stock solution *AR-P 639.04* (*allresist GmbH*) with other solvents to improve wetting. Mixing with a DCM:EtOH solution of as well as mixing with water was tested in different ratios, both leading to limited improvement of wetting but also highly inhomogeneous mold-filling and RL.

The experiments of this part of the thesis have proven that the solvent of the imprint material plays a vital role regarding mold filling, if no hydrophilic surface treatment of the mold is desired. Since the tested stock solutions and their mixtures with other solvents have failed to significantly improve mold filling, the necessity of more careful solvent selection becomes evident.

Another approach to improve resist adhesion was by surface modification of the mold before its spin coating. In this regard, 5 seconds of oxygen plasma treatment of the hybrid molds (consisting of an s-PDMS bulk and a h-PDMS top) drastically improved resist adhesion, but also damaged the mold's structural integrity, and caused extensive surface cracking for treatments exceeding 1 minute. These molds could not be separated from the imprinted material without serious damage. This problem was solved by utilizing a mold made up solely of s-PDMS. These molds stayed intact after repeated use and showed immensely improved mold filling. Due to the observed destructive behavior of the oxygen plasma treatment, two other treatments have been tested: Prolonged exposure to oxygen gas for up to 45 minutes did not show visible wetting improvement. On the other hand, UV treatment for 90 minutes led to limited improvement, although not enough to lead to a good mold filling.

Using oxygen plasma treatment of the s-PDMS mold, good wetting and near residual layer-free patterning of the PMMA film could be achieved for all four triangle sizes. When added to water, the structures were observed via OM to break lose from one another and were released as particles.

Concerning the separation of an imprinted polymer from the mold, the utilized extraction method inspired by *Kavre et al.* and *Ha et al.* has proven simple and efficient. Using a PVA extraction foil, the imprinted PMMA film can be peeled off using tweezers and stored on a substrate or added to water to release the particles.

However, this method does not attach the extracted polymer film to the substrate. As PVA is very sensitive to water, changes in moisture cause the film to curl up over time. This proposes a hindrance for further processes that require a flat sample. Accordingly, several variations to the above extraction method have been tested. A simple way was found by utilizing double-sided tape to attach the PVA layer to the sample substrate

before its separation from the mold. This method held the samples flat and the polymer film can be peeled off the tape to release the embedded particles.

In the final stage of this thesis, RL-free patterned PMMA was used for sputter deposition. Magnetic characterization via VSM and Kerr magnetometry confirmed ferromagntetic behavior with a coercive field of $H_C = (4.4 \pm 0.5)\,\mathrm{kA/m}$. On the other hand, no EB field could be measured. Investigation of several possible causes allowed for the extraction method to be identified as the reason for the absence of a measurable EB field. Detailed AFM investigations were then carried out to compare samples with and without a measurable EB field for their surface roughness and grain size distribution. While no correlation was found between the samples' properties and their grain size distribution, it could be shown that the measured EB field of a sample decreases with an increase of its roughness. Due to the resolution of the roughness measurements, they were interpreted to reflect the height relation of multiple grains among each other instead of the topography of individual grains. Using the model for a polycrystalline AF by *Fulcomer* and *Charap*, an increased roughness was correlated to an increased number of frustrated bonds and domain walls at the AF/F interface, both hindering efficient coupling of the interface grains.

It was interpreted that the flexibility of the PVA film during extraction via tweezers or tape as well as the applied pressure during tape attachment increase the roughness of the patterned surface. Hence, the extraction process has to be more controlled and rigid if succeeding EB layer system deposition is desired. To achieve this, a combination of the methods employed by *Ha et al.* and *Huang et al.* was suggested. This new method is hypothesized to enable a flat an rigid PMMA extraction, hence lowering PMMA surface roughness, while still utilizing the PVA foil for later particle release.

Based on these results, several recommendations can be given for future research of this topic.

If surface treatment of the mold is not desired, resist adhesion must be improved by finding a suitable imprint material solvent. In other works, solid the imprint resist was obtained by dissolving the respective solid polymer in Anisole [24] or dichloromethane with succeeding dilution using ethanol [94] (not as mixture with *AR-P 639.04*, but as sole solvent). Using these solvents to dissolve solid PMMA is hence reasonable to test. Apart from this, considering possible solvents for PMMA based on their surface tension and generally using hydrophobic solvents like toluene is another suggested approach.

Further testing of less aggressive mold surface treatments remains important. Although immense improvement of mold wetting was achieved by its surface treatment with oxygen plasma, the destructive influence of this treatment was demonstrated in this thesis. Especially regarding the expansion to a broader use of imprint materials, oxygen plasma treated PDMS molds might show too strong adhesion to the imprint material, as was observed for PVA. A promising route in this regard might be the combination of UV and ozone treatment as performed by *Efimenko et al.*

Ferromagnetic surface functionalization via sputter deposition of RNIL patterned polymer particles can be achieved as reported in this thesis and used for microfluidic experiments or fabrication of multifunctional polymer particles. For example, a guest-

host polymer system can be fabricated as by *Kaban* and then surface functionalized as performed here. Exchange biased, patterned polymer films can similarly be used in further research, for example in combination with magnetic field landscaping.

In order to be able to produce exchange biased polymer particles, further experiments addressing rigid extraction methods are required. Reproducing the substrate transfer method employed by *Fernández et al.* while using a PVA release layer as employed in this thesis seems a promising route to prevent increase of surface roughness, which was observed to decrease the EB effect. In this regard, it would be useful to quantify how surface roughness changes after adding of each layer, in order to learn if and how the morphology of the capping layer provides information about the AF/F interface. This could provide important information about the related results of this thesis. Alternatively, the deposited layer system can be modified to be more comparable with other works investigating the correlation of AF/F interface roughness and resulting EB effect, like that of *Liu et al.* [113].

The goal of this thesis to establish the RNIL technique for the reliable production of residual layer-free, anisotropically shaped poylmer films and particles was achieved by assessing the factors most influential for a successful imprint and by finding a way to drastically increase resist adhesion through mold surface treatment. The results of this thesis can be either transferred to other patterns and materials directly, or used to develop reasonable approaches to expand its applicability, some of which are already suggested. The last step necessary for the fabrication of free, exchange biased polymer particles has been identified through AFM investigation as a modification of the extraction method for the imprinted polymer film, a promising example of which has also been provided.

7 References

[1] J. Jeevanandam, A. Barhoum, Y. S. Chan, A. Dufresne, M. K. Danquah, *Beilstein journal of nanotechnology* **2018**, *9*, 1050–1074.

[2] S. Mourdikoudis, R. M. Pallares, N. T. K. Thanh, *Nanoscale* **2018**, *10*, 12871–12934.

[3] B. Bhushan, *Springer handbook of nanotechnology: Multi-platform DVD-ROM accompanying the printed version*, 2./3. ed., Springer, Berlin [u.a.], **2010**.

[4] R. Mathaes, G. Winter, A. Besheer, J. Engert, *Expert opinion on drug delivery* **2015**, *12*, 481–492.

[5] M. A. Doborovolskaia, S. E. McNeil, *Handbook of immunological properties of nanomaterials*.

[6] M. A. Dobrovolskaia, S. E. McNeil, *Nature nanotechnology* **2007**, *2*, 469–478.

[7] V. P. Chauhan, T. Stylianopoulos, J. D. Martin, Z. Popović, O. Chen, W. S. Kamoun, M. G. Bawendi, D. Fukumura, R. K. Jain, *Nature nanotechnology* **2012**, *7*, 383–388.

[8] M. J. Ernsting, M. Murakami, A. Roy, S.-D. Li, *Journal of controlled release : official journal of the Controlled Release Society* **2013**, *172*, 782–794.

[9] H. L. Kutscher, P. Chao, M. Deshmukh, Y. Singh, P. Hu, L. B. Joseph, D. C. Reimer, S. Stein, D. L. Laskin, P. J. Sinko, *Journal of controlled release : official journal of the Controlled Release Society* **2010**, *143*, 31–37.

[10] M. Faraji, Y. Yamini, M. Rezaee, *Journal of the Iranian Chemical Society* **2010**, *7*, 1–37.

[11] H. Otsuka, Y. Nagasaki, K. Kataoka, *Advanced Drug Delivery Reviews* **2003**, *55*, 403–419.

[12] M. Noga, D. Edinger, R. Kläger, S. V. Wegner, J. P. Spatz, E. Wagner, G. Winter, A. Besheer, *Biomaterials* **2013**, *34*, 2530–2538.

[13] R. A. Bader, A. L. Silvers, N. Zhang, *Biomacromolecules* **2011**, *12*, 314–320.

[14] D. E. Owens, N. A. Peppas, *International journal of pharmaceutics* **2006**, *307*, 93–102.

[15] J. A. Champion, Y. K. Katare, S. Mitragotri, *Journal of controlled release : official journal of the Controlled Release Society* **2007**, *121*, 3–9.

[16] N. Daum, C. Tscheka, A. Neumeyer, M. Schneider, *Wiley interdisciplinary reviews. Nanomedicine and nanobiotechnology* **2012**, *4*, 52–65.

[17] C. Fang, B. Shi, Y.-Y. Pei, M.-H. Hong, J. Wu, H.-Z. Chen, *European journal of pharmaceutical sciences : official journal of the European Federation for Pharmaceutical Sciences* **2006**, *27*, 27–36.

[18] J. A. Champion, S. Mitragotri, *Proceedings of the National Academy of Sciences of the United States of America* **2006**, *103*, 4930–4934.

[19] J. A. Champion, S. Mitragotri, *Pharmaceutical research* **2009**, *26*, 244–249.

[20] T. C. Carvalho, J. I. Peters, R. O. Williams, *International journal of pharmaceutics* **2011**, *406*, 1–10.

[21] S. Y. Chou, P. R. Krauss, P. J. Renstrom, *Applied Physics Letters* **1995**, *67*, 3114–3116.

[22] J. Perumal, T. H. Yoon, H. S. Jang, J. J. Lee, D. P. Kim, *Nanotechnology* **2009**, *20*, 055704.

[23] K.-S. Kim, K.-D. Kim, J.-H. Jeong, H.-J. Lee, J.-H. Kim, *Electronic Materials Letters* **2013**, *9*, 845–850.

[24] A. Fernández, J. Medina, C. Benkel, M. Guttmann, B. Bilenberg, L. H. Thamdrup, T. Nielsen, C. M. Sotomayor Torres, N. Kehagias, *Microelectronic Engineering* **2015**, *141*, 56–61.

[25] R. Waser, *Nanoelectronics and information technology: Advanced electronic materials and novel devices*, 3. completely rev. and enlarged ed., Wiley, Weinheim, **2012**.

[26] M. D. Austin, H. Ge, W. Wu, M. Li, Z. Yu, D. Wasserman, S. A. Lyon, S. Y. Chou, *Applied Physics Letters* **2004**, *84*, 5299–5301.

[27] F. Hua, Y. Sun, A. Gaur, M. A. Meitl, L. Bilhaut, L. Rotkina, J. Wang, P. Geil, M. Shim, J. A. Rogers, A. Shim, *Nano Letters* **2004**, *4*, 2467–2471.

[28] U.-M. Ha, B. Kaban, A. Tomita, K. Krekić, D. Klintuch, R. Pietschnig, A. Ehresmann, D. Holzinger, H. Hillmer, *Applied Nanoscience* **2018**, *8*, 1161–1169.

[29] W. H. Meiklejohn, C. P. Bean, *Physical Review* **1956**, *102*, 1413–1414.

[30] R. Kassing, *Festkorper*, De Gruyter, Berlin, **2005**.

[31] R. Gross, A. Marx, *Festkörperphysik*, Oldenbourg, München, **2012**.

[32] A. Hubert, R. Schäfer, *Magnetic Domains: The Analysis of Magnetic Microstructures*, Springer Berlin Heidelberg, Berlin, Heidelberg, **1998**.

[33] M. Getzlaff, *Fundamentals of magnetism*, Springer, Berlin and New York, **2008**.

[34] D. C. Mattis, *The theory of magnestism made simple*, Rev. ed., World Scientific, New Jersey, **2004**.

[35] R. M. White, *Quantum Theory of Magnetism: Magnetic Properties of Materials*, Springer Berlin Heidelberg, Berlin, Heidelberg, **2007**.

[36] W. Commons, File:Bethe-Slater curve by Zureks.svg — Wikimedia Commons, the free media repository, [Online; accessed 3-March-2019], **2011**.

[37] W. Demtröder, *[Atome, Moleküle und Festkörper]: Mit 48 Tabellen, zahlreichen durchgerechneten Beispielen und 151 Übungsaufgaben mit ausführlichen Lösungen*, 4., überarb. Aufl., Springer, Berlin, **2010**.

[38] W. H. Meiklejohn, *Journal of Applied Physics* **1962**, *33*, 1328–1335.

[39] Grünberg, Schreiber, Pang, Brodsky, Sowers, *Physical review letters* **1986**, *57*, 2442–2445.

[40] Z. Radović, M. Ledvij, L. Dobrosavljević-Grujić, A. I. Buzdin, J. R. Clem, *Physical Review B* **1991**, *44*, 759–764.

[41] N. R. Werthamer, *Physical Review* **1963**, *132*, 2440–2445.

[42] F. Radu, H. Zabel in *Magnetic Heterostructures*, (Eds.: H. Zabel, S. D. Bader), Springer Tracts in Modern Physics, Springer Berlin Heidelberg, Berlin, Heidelberg, **2008**, pp. 97–184.

[43] A. Mougin, S. Poppe, J. Fassbender, B. Hillebrands, G. Faini, U. Ebels, M. Jung, D. Engel, A. Ehresmann, H. Schmoranzer, *Journal of Applied Physics* **2001**, *89*, 6606–6608.

[44] A. Ehresmann, D. Engel, T. Weis, A. Schindler, D. Junk, J. Schmalhorst, V. Höink, M. D. Sacher, G. Reiss, *physica status solidi (b)* **2006**, *243*, 29–36.

[45] A. Ehresmann, I. Koch, D. Holzinger, *Sensors (Basel Switzerland)* **2015**, *15*, 28854–28888.

[46] D. Holzinger, I. Koch, S. Burgard, A. Ehresmann, *ACS nano* **2015**, *9*, 7323–7331.

[47] D. Holzinger, D. Lengemann, F. Göllner, D. Engel, A. Ehresmann, *Applied Physics Letters* **2012**, *100*, 153504.

[48] W. H. Meiklejohn, C. P. Bean, *Physical Review* **1957**, *105*, 904–913.

[49] J. Nogués, I. K. Schuller, *Journal of Magnetism and Magnetic Materials* **1999**, *192*, 203–232.

[50] A. E. Berkowitz, K. Takano, *Journal of Magnetism and Magnetic Materials* **1999**, *200*, 552–570.

[51] N. D. Müglich, Dissertation, Universität Kassel, Kassel, **2016**.

[52] M. Merkel, MA thesis, Universität Kassel, **2018**.

[53] E. C. Stoner, E. P. Wohlfarth, *Philosophical Transactions of the Royal Society A: Mathematical Physical and Engineering Sciences* **1948**, *240*, 599–642.

[54] Y. Bai, G. Yun, N. Bai, *Journal of Applied Physics* **2010**, *107*, 033905.

[55] D. Mauri, E. Kay, D. Scholl, J. K. Howard, *Journal of Applied Physics* **1987**, *62*, 2929–2932.

[56] R. Jungblut, R. Coehoorn, M. T. Johnson, J. aan de Stegge, A. Reinders, *Journal of Applied Physics* **1994**, *75*, 6659–6664.

[57] *Magnetic Properties of Low-Dimensional Systems II: New Developments. Proceedings of the Second Workshop, San Luis Potosí, Mexico, May 23-26, 1989*, Softcover reprint of the original 1st ed. 1990, (Eds.: L. M. Falicov, F. Mejia-Lira, J. L. Moran-Lopez), Springer Berlin, Berlin, **2014**.

[58] F. B. Hagedorn, *Journal of Applied Physics* **1967**, *38*, 3641–3645.

[59] L. Néel, *Annales de Physique* **1967**, *14*, 61–80.

[60] K. O'Grady, L. E. Fernandez-Outon, G. Vallejo-Fernandez, *Journal of Magnetism and Magnetic Materials* **2010**, *322*, 883–899.

[61] M. Kiwi, *Journal of Magnetism and Magnetic Materials* **2001**, *234*, 584–595.

[62] A. P. Malozemoff, *Physical Review B* **1988**, *37*, 7673–7679.

[63] A. P. Malozemoff, *Physical Review B* **1987**, *35*, 3679–3682.

[64] T. Ueltzhöffer, MA thesis, Universität Kassel, **2013**.

[65] E. Fulcomer, S. H. Charap, *Journal of Applied Physics* **1972**, *43*, 4190–4199.

[66] E. Fulcomer, S. H. Charap, *Journal of Applied Physics* **1972**, *43*, 4184–4190.

[67] A. Ehresmann, D. Junk, D. Engel, A. Paetzold, K. Röll, *Journal of Physics D: Applied Physics* **2005**, *38*, 801–806.

[68] A. Ehresmann, C. Schmidt, T. Weis, D. Engel, *Journal of Applied Physics* **2011**, *109*, 023910.

[69] A. GmbH, Resist-Wiki E-Beam Resist Allgemein, `https://www.allresist.de/category/resist-wiki-e-beam-resist-allgemein/`, Accessed: 2019-02-26.

[70] S. Landis, *Nano-lithography*, Online-ausg, ISTE, London and Hoboken, N.J, **2011**.

[71] B. Kwon, J. H. Kim, *Journal of Nanoscience* **2016**, *2016*, 1–12.

[72] K. Seshan, *Handbook of thin-film deposition processes and techniques: Principles, methods, equipment and applications*, 2nd ed., Noyes Publications/William Andrew Pub, Norwich, N.Y, **2002**.

[73] H. Hucfeldt, MA thesis, Universität Kassel, **2011**.

[74] H. Huckfeldt, Dissertation, Universität Kassel, Kassel, **2018**.

[75] A. Paetzold, Dissertation, Universität Kassel, Kassel, **2002**.

[76] N. P. Aley, G. Vallejo-Fernandez, R. Kroeger, B. Lafferty, J. Agnew, Y. Lu, K. O'Grady, *Journal of Applied Physics* **2008**, *44*, 2820–2823.

[77] J. B. Sousa, J. A. M. Santos, R. F. A. Silva, J. M. Teixeira, J. Ventura, J. P. Araújo, P. P. Freitas, S. Cardoso, Y. G. Pogorelov, G. N. Kakazei, E. Snoeck, *Journal of Applied Physics* **2004**, *96*, 3861–3864.

[78] S. J. Gamble, M. H. Burkhardt, A. Kashuba, R. Allenspach, S. S. P. Parkin, H. C. Siegmann, J. Stöhr, *Physical review letters* **2009**, *102*, 217201.

[79] S. Foner, *Physical Review* **1959**, *30*, 548–557.

[80] T. Weis, Dissertation, Universität Kassel, Kassel, **2009**.

[81] J. M. D. Coey, *Magnetism and magnetic material*, Cambridge University Press, **2009**.

[82] P. Eaton, P. West, *Atomic force microscopy*, Oxford University Press, Oxford, **2018**.

[83] F. Gołek, P. Mazur, R. Z., S. Zuber, *Applied Surface Science* **2014**, *304*, 11–19.

[84] DME Nanotechnologie GmbH, The AFM Starter-Guide, **2010**.

[85] M. Reginka, MA thesis, Universität Kassel, **2018**.

[86] A. GmbH, Amonil: High Performance UV Nanoimprint Resist, `https://www.amo.de/de/products-services/amonil/`, Accessed: 2019-02-11.

[87] micro resist technology GmbH, Nanoimprint Resists - Resists for Nanoimprint Lithography (NIL), `https://www.microresist.de/en/product/nanoimprint-resists`, Accessed: 2019-02-11.

[88] T. Schmitte, T. Schemberg, K. Westerholt, H. Zabel, K. Schädler, U. Kunze, *Journal of Applied Physics - J APPL PHYS* **2000**, *87*, 5630–5632.

[89] A. Tavakkoli K. G., M. Ranjbar, S. N. Piramanayagam, S. K. Wong, W. C. Poh, R. Sbiaa, T. C. Chong, *Nanoscience and Nanotechnology Letters* **2012**, *4*, 835–838.

[90] M. GmbH, Grundlagen der Mikrostrukturierung, `https://www.microchemicals.com/technische_informationen/substrat_reinigung_haftung_fotolack.pdf`, Accessed: 2019-02-15.

[91] T. Young, *Philosophical Transactions of the Royal Society of London* **1805**, *95*, 65–87.

[92] A. GmbH, Positiv-PMMA E-Beamresists AR-P 630 - 670 er, `https://www.allresist.de/wp-content/uploads/2015/12/allresist_produktinfos_ar-p630_deutsch.pdf`, Accessed: 2019-02-16.

[93] N. C. for Biotechnology Information, PubChem Compound Database, `https://www.ncbi.nlm.nih.gov/pccompound`, Accessed: 2019-02-16.

[94] B. Kaban, MA thesis, Universität Kassel, **2018**.

[95] K. Krekić, E. Käkel, D. Klintuch, D. Bloß, R. Pietschnig, *Zeitschrift fur anorganische und allgemeine Chemie* **2018**, *644*, 149–154.

[96] D. J. Carbaugh, J. T. Wright, F. Rahman, *Microelectronic Engineering* **2017**, *171*, 53–59.

[97] I. Y. Evchuk, R. I. Musii, R. G. Makitra, R. E. Pristanskii, *Russian Journal of Applied Chemistry* **2005**, *78*, 1576–1580.

[98] Y.-F. Qian, Y. Su, X.-Q. Li, H.-S. Wang, C.-L. He, *Iranian Polymer Journal (English Edition)* **2010**, *19*.

[99] M. J. Owen, P. J. Smith, *Journal of Adhesion Science and Technology* **1994**, *8*, 1063–1075.

[100] D. Bodas, C. Khan-Malek, *Sensors and Actuators B: Chemical* **2007**, *123*, 368–373.

[101] S. O., *Langmuir* **2003**, *19*, 8117.

[102] O. Z., *J. Colloid Interface Sci.* **1998**, *202*, 37.

[103] G. F., *J. Colloid Interface Sci.* **1989**, *132*, 504.

[104] W. K., *Polymer* **2000**, *41*, 6851.

[105] D. I., *Phys. Status Solidi (c)* **2010**, *7*, 189.

[106] K. Efimenko, W. E. Wallace, J. Genzer, *Journal of Colloid and Interface Science* **2002**, *254*, 306–315.

[107] R. A. Lawton, C. R. Price, A. F. Runge, W. J. Doherty, S. S. Saavedra, *Colloids and Surfaces A: Physicochemical and Engineering Aspects* **2005**, *253*, 213–215.

[108] V. Jokinen, P. Suvanto, S. Franssila, *Biomicrofluidics* **2012**, *6*, 016501.

[109] D. Maji, S. K. Lahiri, S. Das, *Surface and Interface Analysis* **2012**, *44*, 62–69.

[110] C. E. Scott, poly(vinyl alcohol), `http://www.polymerprocessing.com/polymers/PVOH.html`, Accessed: 2019-03-21.

[111] S. Y. Tan, Y. Tatsumura, *Singapore medical journal* **2015**, *56*, 366–367.

[112] C. Liu, C. Yu, H. Jiang, L. Shen, C. Alexander, G. J. Mankey, *Journal of Applied Physics* **2000**, *87*, 6644–6646.

[113] C. Liu, L. Shen, H. Jiang, D. Yang, G. Wu, C. Alexander, G. J. Mankey, *MRS Proceedings* **1999**, *562*, DOI `10.1557/PROC-562-69`.

[114] P. Barna, M. Adamik, *Thin Solid Films* **1998**, *317*, 27–33.

[115] M. Vopsaroiu, G. V. Fernandez, M. J. Thwaites, J. Anguita, P. J. Grundy, K. O'Grady, *Journal of Physics D: Applied Physics* **2005**, *38*, 490–496.

List of Figures

List of Abbreviations

Acronyms

AF antiferromagnet.

AFM atomic force microscope.

DCM dichloromethane.

e-beam electron beam.

EB exchange bias.

EBL electron beam lithography.

EBLS exchange bias layer system.

F ferromagnet.

FDTS perfluorodecyltrichlorosilane.

h-PDMS hard PDMS.

L-MOKE longitudinal magneto-optic Kerr effect.

MOKE magneto-optic Kerr effect.

MT master template.

NIL nanoimprint lithography.

OM optical microscope.

P-MOKE polar magneto-optic Kerr effect.

PDMS Polydimethylsiloxane.

PMMA poly(methyl methacrylate).

PVA polyvinyl alcohol.

RIE reactive ion etching.

RL residual layer.

RNIL reversal nanoimprint lithography.

s-PDMS soft PDMS.

SEM scanning electron microscope.

T-MOKE transversal magneto-optic Kerr effect.

VSM vibrating sample magnetometer.

[style=long]

8 Acknowledgments

Zu Beginn möchte ich mich herzlich bei *Prof. Dr. Hartmut Hillmer* für die Ermöglichung dieser Abschlussarbeit durch die Aufnahme in die Arbeitsgruppe der *Technischen Elektronik* im *Institut für Nanostrukturtechnologie und Analytik (INA)* bedanken. Ebenso sehr gilt mein Dank *Prof. Dr. Arno Ehresmann* für die Aufnahme in die *Arbeitsgruppe Ehresmann*, was dieses spannende Kooperationsprojekt erst ermöglicht hat.

Weiterhin bedanke ich mich bei *Uh-Myong Ha* und *Andreea Tomita* für die tolle Betreuung und die solide fachliche Hilfestellung, ganz besonders in der Anfangszeit dieser Arbeit. Vielen Dank für diese einzigartige Gelegenheit, mich fachlich wie persönlich weiterzuenwickeln.

Ich möchte mich bei allen Mitarbeitern der *Technischen Elektronik* für die überaus freundliche Arbeitsatmosphäre bedanken. Besonderer Dank gilt hierbei *Anita Dück* und *Jens Krumpholz* für die Unterstützung in Sachen Geräteeinweisungen, technischen oder materialbezogenen Schwierigkeiten. Vielen Dank auch an *Burhan Kaban* und *Eireen Käkel* für die gemeinsame Zeit im INA und an *Christine Heume* für den gelegentlichen Büro-Plausch.

Das Gleiche gilt für die Mitarbeiter der *Arbeitsgruppe Ehresmann*. Die herzliche Aufnahme und die wertvollen Ratschläge werde ich nicht vergessen. Hier muss ich ganz besonders *Iris Koch* und *Meike Reginka* für die Hilfe mit- und das gemeinsame Leiden vor dem AFM danken. Manchmal ist es beruhigend zu hören, dass ein Gerät nicht nur einen selbst nicht leiden kann. In diesem Hinblick gilt mein Dank auch *Dr. Dennis Holzinger*, *Maximilian Merkel* und nochmal Meike für die geteilte Fachkompetenz, die in die entsprechenden Kapitel mit eingeflossen ist.

There is no way to express my gratitude towards *Jacqueline Tiaga*. You did not only keep me sane in the last months of this thesis, but also nourished and balanced. Thank you *so* much for all your support, for the delicious meals and drinks we had together, and so much more.

Vielen Dank auch an meine Freunde und Familie für den notwendigen Ausgleich außerhalb der Uni. Vorallem meiner Mutter möchte ich danken, die mir stets mit nie endender Liebe und Unterstützung zur Seite steht.

9 Statement of Authorship

I hereby declare that this submitted master thesis is my own work. All supporting material and sources used are acknowledged as references. I assure that passages which were literally or analogously taken from published documents are marked with the corresponding citation within the text. Neither this nor a similar work has been presented to an examination committee.

Kassel, March 22, 2019 .....